NUMERICAL MODELING OF SIMPLE LABORATORY EXPERIMENTS OF ROTATING FLOWS

JOSE M. LOPEZ

Dissertation submitted for the Degree of

Doctor of Philosophy

UNIVERSITAT POLITÈCNICA DE CATALUNYA

DEPARTAMENT DE FÍSICA APLICADA

November 2014

NUMERICAL MODELING OF SIMPLE LABORATORY EXPERIMENTS OF ROTATING FLOWS

Jose M. Lopez, Ph.D.
Universitat Politècnica de Catalunya 2014

Despite the large amount of research which has been conducted on turbulent flows, a full understanding of their dynamics as well as the mechanisms involved in the onset of turbulence is still missing. Experimental studies of transition to turbulence are generally carried out in setups with simple geometries which allow isolating the physical mechanisms underlying the dynamics. However, in spite of the simplicity of the models, the problem is extremely complex and it is difficult to reach definitive conclusions on many of the observed dynamical features. Since a few decades ago numerical simulations complement laboratory experiments, significantly accelerating the scientific progress and improving the quality of investigations. In order to compare experimental and numerical results, it is essential to carry out a calibration process in which the possible discrepancies are identified and adjustments (typically modifications in the numerical formulation of the problem) are made in order to minimize them as far as possible.

The results of this thesis are primarily intended as an aid in the calibration process of rotating flows in presence of a temperature gradient, which are of great interest in multiple industrial, geophysical and astrophysical applications. Numerical simulations of the flow enclosed in rotating cylindrical and annular cavities subjected to either a vertical or horizontal temperature gradient (rotating Rayleigh–Bénard convection and laterally heated Taylor–Couette flows) have been performed. Several techniques of numerical analysis such as direct simulation of the governing equations, linear stability analysis, continuation methods or time–series analysis have been used for the completion of the thesis.

Three sources of discrepancies between experimental and numerical results have been investigated. First, we show a detailed study of how symmetry-breaking due to experimental imperfections may modify the dynamics of the idealized systems used in numerical simulations. An example in rotating Rayleigh–Bénard convection is illustrated in which simulations only capture the experimental behavior when this symmetry-breaking is introduced in the formulation of the problem, i.e. through the boundary conditions. Second, we consider the influence of centrifugal effects which are often neglected in theoretical and numerical studies of rotating flows. This may result in substantial differences with experimental results in those ranges of parameters in which centrifugal buoyancy plays a significant dynamical role. To this extent, we provide a straightforward Boussinesq-type approximation which allows for considering centrifugal effects in an inertial reference frame, including secondary effects stemming from differential rotation or strong internal vorticity, which had not been previously considered in any other formulation. Third, the influence of axial end walls in the dynamics of simple models for the study of baroclinic flows is discussed. The objective of this study is to identify the degree to which simulations in axially periodic systems, with a lower computational cost, can be used to reproduce experimental results. A strong stabilizing effect, which increases significantly at high temperature differences between the cylinders, results from the boundary layers and cause large discrepancies with the onset of instability in the case of axially periodic boundary conditions. Finally, a numerical study of a recently reported experimental bifurcation scenario in isothermal Taylor–Couette flow is also presented.

We focus on the dynamics of flow patterns characterized by large amplitude oscillations that are localized only in some vortex-pairs. In this case, experimental and numerical results are in full agreement.

ACKNOWLEDGEMENTS

I would like to express my gratitude to everyone who has assisted and supported me during the completion of this thesis project. First and foremost, I would like to express my sincere thanks to my academic advisers, Dr. Francisco Marqués Truyol and Dr. Marc Avila Canyellas, for their guidance and mentoring. I would also like to thank all colleagues I have worked with, near or far, over the last few years, who also have contributed to the success of this thesis.

Part of the work was done during my visits to the Institute of Fluid Mechanics at the Friedrich-Alexander-Universität Erlangen-Nürnberg, whose kind hospitality is warmly appreciated. I am also grateful to Dr. Björn Hof and the Institute of Science and Technology (Klosterneuburg) for giving me the opportunity of sharing with his group three wonderful months.

I would never have been able to finish my dissertation without my parents and girlfriend's support. My warm thanks go to them all.

I want to thank the Spanish Government who has financed this thesis through the Spanish Government grants FIS2009-08821 and BES-2010-041542 and Red Española de Supercomputación (RES) for the computational resources provided.

TABLE OF CONTENTS

LIST OF TABLES

LIST OF FIGURES

CHAPTER 1

INTRODUCTION

1.1 Rotating flows

Before going into detail with mathematical intricacies and physical interpretations, it is convenient to lead the reader into the subject matter of the thesis: the rotating flows. To this extent, this chapter begins with a brief overview which highlights the main applications of the theory of rotating flows in various scientific fields, spanning from engineering to geophysical and astrophysical flows.

Rotating flows are found in a wide range of industrial applications, such as pump and compressor impellers, gas turbines engines, rotating heat exchangers, rotational viscometers, cyclone separators, brakes, gears or computer storage devices (see e.g. Shepherd (1956); Childs (2011); Rhodes (1998); Lappa (2012)). The understanding of the dynamics is essential to ensure the proper design, maintenance and performance of these industrial appliances. Let us see a couple of examples.

In figure 1.1 the schematic of the simplest case of a cyclonic particles separator is illustrated. In such devices a gaseous stream is separated from solid particles or fine droplets of liquid. The fluid mixture enters the container (cyclone) through the inlet at the top and results in swirling motion. The denser (heavier) particles are then centrifuged radially outward, and collide with the wall, falling for gravity towards the bottom end of the container where they are removed. By contrast, the lighter clean gaseous stream rises and exits the cyclone through the outlet at the top. As the flow goes downward the conic section reduces and the rotational speed increases, allowing for a better efficiency in removing particles of smaller sizes. Cyclonic separators often incorporate a secondary air flow which directs particles towards the collector bin, thus making particles collection more efficient and improving abrasion resistance. Practical applications of cyclonic separators include elimination of pollutants in manufacturing plants, gas-liquid separation in oil refineries, kitchen ventilation or vacuum cleaners (see Rhodes (1998) for an extensive treatment of the subject).

In figure 1.2 a schematic drawing of a gas turbine engine is shown. This device is widely used as a propulsion system for aircraft, ships and trains, as well as in power generation plants. The air stream is accelerated by the rotating blades of the compressor so that the pressure increases and the air volume reduces. High-pressure air passes through a combustion chamber where fuel is added, and the mixture ignites at a constant pressure.

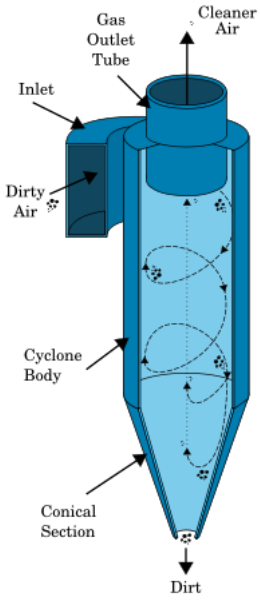

Figure 1.1: Schematic of a simple cyclone separator. Courtesy of C. Barnett.

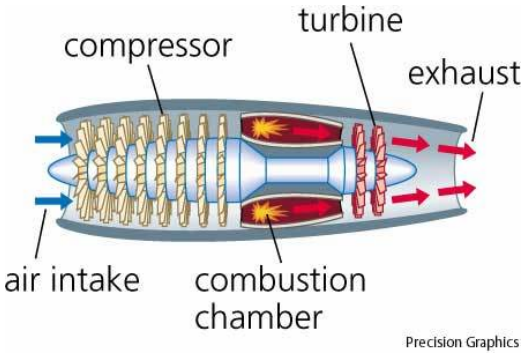

Figure 1.2: Schematic of a gas turbine engine. Courtesy of Houghton Mifflin Harcourt Publishing Company.

The high speed gases resulting from the combustion spin the turbine, turning the kinetic energy of the gaseous stream into mechanical energy in the form of shaft power. One of the major concerns for designers of gas turbine engines is the cooling of the rotating turbine. In turbines the flow expands through alternating rotating and stationary discs, which form small cylindrical cavities between them. Impurities may accumulate in these cavities, resulting in performance deterioration and limiting the lifetime of the turbine. This problem is mitigated through the injection of cool air which cleans the cavity. However, this lowers the cavity temperature and obstructs the access of gas, hence the turbine performance is significantly reduced. Understanding the turbulent dynamics of the flow in these cavities in order to optimize this process is an example of a very active field of research on industrial rotating flows (Launder *et al.*, 2010).

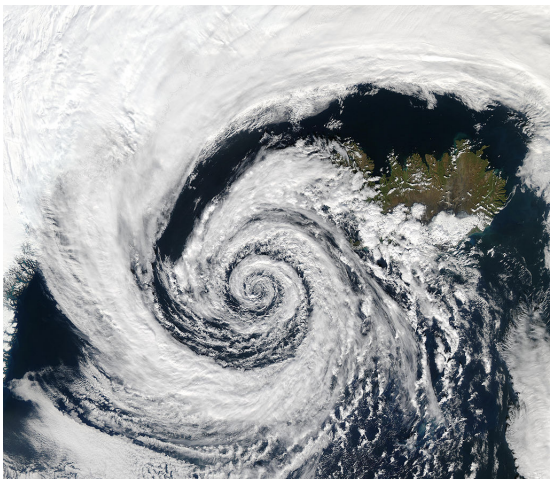

Figure 1.3: Image of a low-pressure system over the southwestern coast of Iceland taken by the Aqua MODIS instrument on September 4, 2003. Courtesy of NASA.

Geophysical fluid dynamics is one of the main application areas of the theory of rotating flows. The large scale flows of the Earth are dominated by the influence of planetary rotation which, along with buoyancy effects due to solar heating, leads to the occurrence of a wide variety of natural phenomena, such as atmospheric cyclones or anticyclones, mesoscale eddies in ocean currents or tsunamis (Pedlosky, 1982; Vallis, 2006). It also applies to the study of the complex atmospheres of the giant planets in the solar system, such as Jupiter, Saturn or Neptune (Sanchez-Lavega, 2011).

Figure 1.3 is a photograph of a cyclone formed in the mid-latitudes of the atmosphere. This type of cyclones, which are refer to as extra-tropical cyclones, generally arise as a result of baroclinic instabilities, and play an essential role in the weather variability. It is for this reason that they are the research focus of numerous investigatory teams in the realm of geophysical flows (see e.g. chapter 10 in Ackerman & Knox (2003) for further information about extra-tropical cyclones).

In figure 1.4 two mesoscale eddies in an oceanic current are illustrated. The size of oceanic mesoscale eddies ranges from a few kilometers up to hundreds of kilometers. They occur as a consequence of multiple physical mechanisms, ranging from the interaction between the current and obstacles such as islands or headlands along the coastline, to instabilities stemming from strong horizontal shear motions or baroclinicity (Collins, 2004). Mesoscale eddies are responsible for the transport of heat and salt around the ocean, and thus are believed to play a relevant role in the climate change (Collins, 2004; Boning *et al.*, 2008; Farneti *et al.*, 2010). They are a relatively recent finding (early 1960's) and, despite significant progress is being made, there are still many questions to

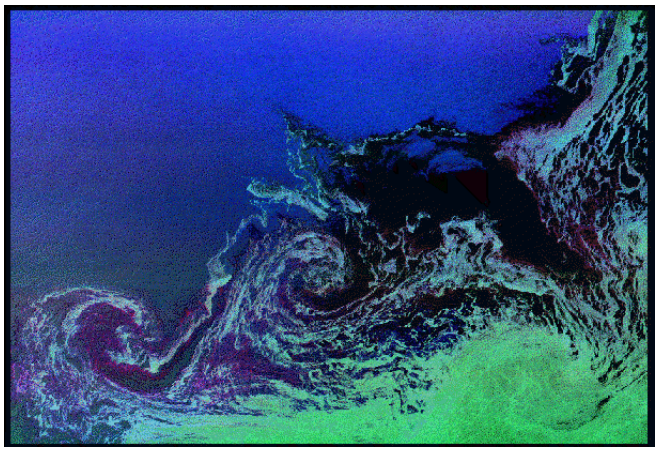

Figure 1.4: Radar image taken by the Shuttle Imaging Radar-C showing two large ocean eddies next to sea ice in the Weddell Sea, Antarctica, on October 5, 1994. Courtesy of NASA.

be answered about the generation mechanisms of these oceanic structures and their role in the general circulation (we refer to Siedler *et al.* (2013) for an extensive review on oceanic circulation).

Finally, attention should also be drawn to rotating flows in an astrophysical context (see Tassoul (2000) for extensive information). The figure 1.5 illustrates an accretion disk around a black hole. Accretion disks are considered as the precursors for the formation of planetary systems. They are composed by a mass of heterogeneous gases (around a 99% of the disk) and solid particles of different sizes (from millimeters to kilometers) and appear surrounding massive celestial objects such as black holes or stars in the universe. As the flow of gases becomes turbulent, angular momentum is transferred outward so that matter flows towards the inner disk layers where accretes onto the central object as a result of gravitational attraction. Although the assumption of turbulence as the element needed to enhance the accretion process is unquestioned, the mechanisms responsible for it are still unclear. This subject, which has generated substantial controversy in recent years (Balbus, 2011), remains one of the biggest challenges for astrophysicists and fluid dynamicists in our days (Klahr *et al.*, 1999; Balbus, 2003; Avila, 2012; Klahr & Bodenheimer, 2003; Lesur & Papaloizou, 2010; Paoletti & Lathrop, 2011; Petersen *et al.*, 2007).

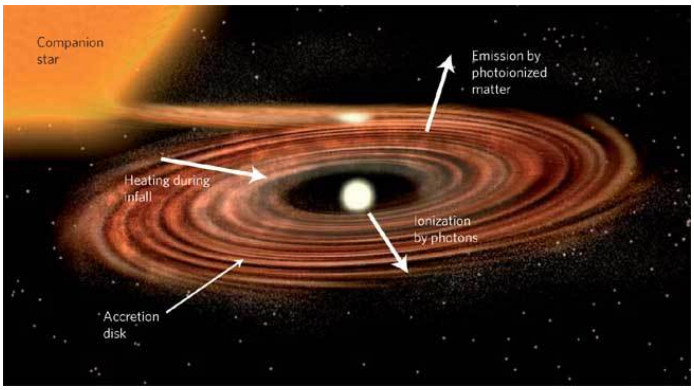

Figure 1.5: Illustration of an accretion disk surrounding a black hole, taken from Drake (2009).

1.2 Transition to turbulence

The study of rotating flows carried out in this thesis primarily focuses on the transition from the laminar to the turbulent regime. Hence, an introductory chapter cannot fail to include a few lines concerning the most relevant concepts on this subject.

The process of transition to turbulence consists of a series of bifurcations taking place as a certain control parameter is varied, which involves the transition from the basic or laminar flow to a turbulent state in which the fluid exhibits complex and chaotic behavior. This problem was first formulated in a formal way by Osborne Reynolds (1883), who investigated the laminar-turbulent transition of water in circular pipe. Despite the time elapsed and the significant amount of work that has been done, it is still one of the most important unsolved problems of classical physics.

A distinction must be made between the two possible bifurcation scenarios that may occur: supercritical and subcritical transitions. In a supercritical scenario, the base flow becomes unstable through infinitesimal disturbances which grow exponentially after the control parameter surpasses a certain critical value. Further increasing the control parameter, the flow undergoes a finite sequence of bifurcations towards more complex spatio-temporal states, which eventually ends up with the appearance of fully developed turbulence. This is the usual bifurcation scenario in Taylor–Couette flows (Golubitsky & Stewart, 1986) and will be discussed in detail in subsequent chapters. In contrast, in a subcritical scenario, the basic flow is linearly stable and becomes unstable through non-linear instabilities that occur due to finite amplitude disturbances. A subcritical bifurcation scenario is typical of shear flows such as plane Couette flow, Poiseuille flow or pipe flow (Eckhardt *et al.*, 2007; Romanov, 1973; Nishioka & Asai, 1985). It will be

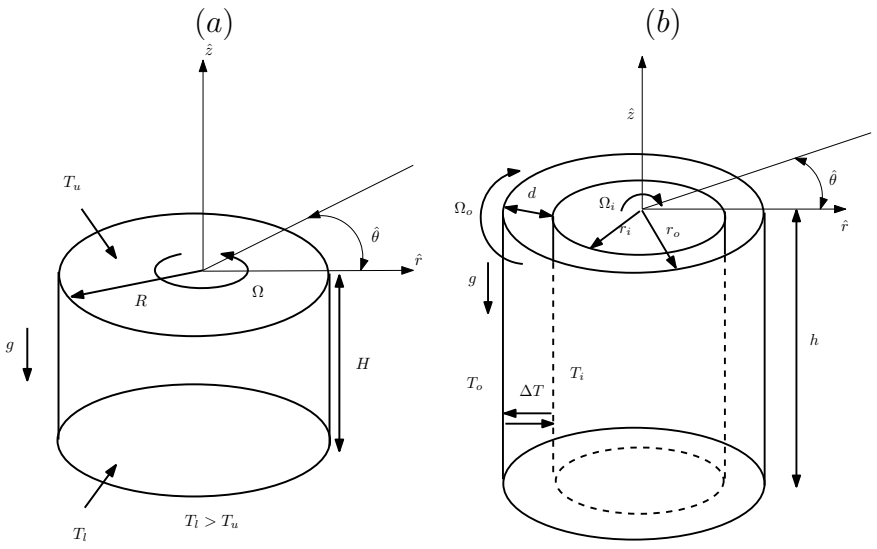

Figure 1.6: Schematic of the experimental setups considered in this thesis. (a) Cylindrical cavity used to study rotating Rayleigh-Bénard convection. (b) Taylor–Couette system.

addressed in chapter 3 in the case of rotating Rayleigh-Bénard convection.

The intermediate flow patterns that occur between the laminar and turbulent states in a supercritical scenario are often due to symmetry-breaking bifurcations, so their features are closely linked to the recipient or environment in which the fluid is contained. The dynamical systems theory provides a symmetry-based approach to study bifurcations and pattern formation in fluids. Thus, experiments on canonical flows are not only used as simple models of complex real flows, but also as a testbed for ideas of the dynamical systems theory which allow further development of the hydrodynamic instability theory.

1.3 Simple models of rotating flows

The laminar-turbulent transition is an extremely complex problem and its study requires of simple models capable of capturing the relevant physics of the real flows to be investigated. For this reason, experiments on rotating fluids are typically performed in cylindrical and annular cavities, which are easily realizable in the laboratory and allow for a straightforward spatial discretization when a numerical approach is accomplished. In particular, the research conducted in this thesis is based upon the experimental setups schematized in figure 1.6.

Figure 1.6 (a) shows a conventional experimental facility for the study of rotating

Rayleigh-Bénard convection. The fluid is confined to a vertical cylinder of radius R and height H which rotates uniformly at constant angular velocity Ω. The bottom lid is maintained at a higher temperature than the top lid, resulting in axial motion due to thermal buoyancy effects. Early studies on rotating Rayleigh-Bénard convection were done by Veronis (1959) and Chandrasekhar (1961), who theoretically investigated the onset of instability in a simple model consisting of an infinite horizontal layer of fluid heated from below. The first laboratory experiments using the setup illustrated in figure 1.6 (a) were carried out by Rossby (1969). He found that, when the fluid is enclosed in a finite geometry, the onset of instability occurs at substantially lower values of the vertical temperature difference than those predicted by the linear stability analysis in a horizontally unbounded domain. Subsequent experiments attributed the discrepancies to the emergence of alternating cold and warm fluid cells localized on the sidewall boundary layer, which were called wall convection modes (Zhong *et al.*, 1991, 1993; Ning & Ecke, 1993). By simplicity, the influence of centrifugal buoyancy was neglected in all theoretical and numerical studies, and the experiments were designed to minimize centrifugal effects in relation to buoyancy effects. Nevertheless, considering the effect of centrifugal buoyancy is an essential ingredient for the study of rotating fluids. When the centrifugal term is included in the governing equations, the basic state is not trivial, but consists of a large-scale circulation in which cold denser fluid is centrifuged towards the sidewall, and warm lighter fluid is centrifuged towards the cylinder axis (Homsy & Hudson, 1969; Hart, 2000). The stability of this basic state was first studied by Homsy & Hudson (1971) for axisymmetric disturbances in the asymptotic limit of infinite Coriolis force, and subsequently extended to finite values of Coriolis and non-axisymmetric instability modes by Marques *et al.* (2007). The non-linear dynamics stemming from the interplay between centrifugal and gravitational forces (keeping the Coriolis force fixed) was reported by Lopez & Marques (2009); Lopez *et al.* (2006). They found that centrifugal effects play a significant stabilizing role which leads to the axisymmetrization of the flow.

In figure 1.6 (b) a Taylor-Couette apparatus is depicted. The fluid is constrained to the gap between two vertical and concentric cylinders of height h and radii r_o and r_i, which may rotate independently with angular velocities Ω_o and Ω_i. This setup was introduced by Couette (1888) to determine the fluid's viscosity from measurements of the torque applied to the cylinders. Taylor (1923) first addressed the stability of the flow contained in that system. He established the onset of instability both theoretically and experimentally, showing an excellent agreement between both results. After this pioneering work, there has been a vast amount of studies focused on this geometry, turning

Taylor–Couette flow in a paradigm for the study of instabilities in fluids and non-linear dynamics in general. The simplest case, which has probably received more attention, is that with the inner cylinder rotating and the outer cylinder at rest. Here, the control parameter used to delimit the different flow regimes is the inner cylinder Reynolds number, $\mathrm{Re}_i = \frac{\Omega_i r_i d}{\nu}$, where d denotes the gap size $d = r_o - r_i$ and ν stands for the kinematic viscosity of the fluid. In the case of infinite long cylinders the base flow consists in a purely azimuthal velocity profile, known as circular Couette flow *CCF*, which remains stable for low values of Re_i. The presence of axial end walls in finite systems introduces radial and axial velocities in the base state, nevertheless, if the apparatus is sufficiently tall, the finite-length effects are confined near the lids and barely modify the *CCF*. As Re_i is increased, the base flow becomes unstable and results in pairs of axisymmetric counter rotating toroidal vortices, the so-called Taylor vortices *TVF* (Taylor, 1923). For the infinite cylinders idealization, these vortical structures occur due to a centrifugal instability at a precise critical value Re_{TVF}. In contrast, in systems of finite length they emerge smoothly from the end walls at $\mathrm{Re}_i \approx \mathrm{Re}_{TVF}$ (Benjamin, 1978; Coles, 1965; Alziary de Roquefort & Grillaud, 1978). Various steady *TVF* states, with a different number of vortices N or changes in the sense of rotation, may coexist for the same values of Re_i (Benjamin & Mullin, 1982). Further increasing Re_i, the *TVF* undergoes a sequence of secondary instabilities which eventually leads the flow to a turbulent regime. The flow exhibits a very rich and complex dynamics along this transition which strongly depends on the geometric parameters of the system: the ratio between the radii of the inner (r_i) and outer (r_o) cylinders ($\eta = \frac{r_i}{r_o}$) and the length-to-gap aspect ratio ($\Gamma = \frac{h}{d}$). Although varying η and Γ results in a vast variety of bifurcation scenarios and therefore it is not possible to establish a general sequence of flow transitions, the so-called Ruelle-Takens scenario is usually considered as a standard route to spatio-temporal chaos in *TCF* (Golubitsky & Stewart, 1986). According to the Ruelle-Takens scenario, when Re_i is increased above a certain critical value Re_{WVF}, the azimuthal symmetry of the *TVF* is broken via a Hopf bifurcation, giving rise to rotating waves that preserve a discrete rotational invariance under rotations of angle $\frac{2\pi}{n}$, where n is the azimuthal wavenumber. The transition towards these flows, commonly known as wavy vortex flow *WVF*, depends on the number of vortices of *TVF* and has been extensively studied both experimentally (Coles, 1965; Mullin, 1985; King & Swinney, 1983; Andereck *et al.*, 1986) and numerically (Jones, 1985; Marcus, 1984). Subsequently increasing Re_i a new Hopf bifurcation occurs at Re_{MWVF}. The resulting quasi-periodic flow is referred to as modulated wavy vortex flow *MWVF* (Coughlin & Marcus, 1992; Gorman & Swinney, 1982). Finally, as increasing Re_i from the *MWVF* regime, the flow begins to lose its spatio-temporal structure and becomes chaotic (Brandstater & Swinney, 1987). The curvature

of the system, given by η, significantly affects the values at which these transitions occur. There exist simple analytical expressions to obtain the critical Re_{TVF} as a function of η (Esser & Grossmann, 1996). DiPrima *et al.* (1984) collected data from the transition to *WVF* in different experiments and concluded that the onset of *WVF* is stabilized as the system approaches the limit $\eta \to 1$. The number of studies regarding *MWVF* is not as plentiful as for the preceding flows, thus it is not easy to draw relevant conclusions on the influence of η. Nevertheless, it is quite common to find qualitatively different behaviors in systems with wide ($\eta < 0.78$) and narrow ($\eta > 0.78$) gaps. The role of Γ is particularly significant, since it does not only affect the critical conditions for the transitions, but also the global dynamical behavior. Whereas in apparatuses with small Γ the dynamics is entirely dominated by the interaction between flow and end walls, in systems with moderate or large Γ the end effects are mitigated, and the dynamics results from the competition between the different flow states that coexist in parameter space (Dutcher & Muller, 2009).

When a radial temperature gradient is included, a Taylor–Couette system is a suitable model for some of the geophysical, astrophysical and industrial flows described in section 1.1. For example, a baroclinic environment in an atmospheric context, in which a cold air mass originating in high latitudes is trapped into a warmer equatorial air mass, can be approximated in the laboratory when the outer cylinder is maintained at a higher temperature than the inner cylinder and both cylinders rotate at a constant angular velocity, which accounts for the planetary rotation (see e.g. Hide (1958)). In contrast, in the context of accretion disks, since the inner layers (often near stars) are considerably hotter than the outer layers, the inner cylinder is set to a higher temperature than the outer cylinder. Both cylinders rotate with different angular velocities following a quasi-Keplerian profile, in which the angular velocity decreases and the angular momentum increases radially outward (Petersen *et al.*, 2007). Taylor–Couette flows with a radial temperature gradient are widely discussed in chapters 4 and 5.

1.4 Laboratory experiments against numerical simulations

At this point, the reader may wonder whether there is any need to perform numerical simulations of models that have been specifically conceived to be implemented in the laboratory. A numerical analyst would surely argue that numerical simulations need a considerable minor economic cost, and at the same time, offer a high degree of flexibility; they allow for performing multiple simultaneous experiments, rapid modification

of boundary and initial conditions, easy access to quantitative data at any point of the fluid domain, isolating the effect of a certain physical mechanism by switching off some terms in the governing equations and remove the restrictions for selecting the input parameters existing in laboratory experiments. In response to these arguments, an experimentalist would say that a numerical simulation is based on a mathematical approximation of the physical reality, and as such, its validity can only be confirmed after its results are satisfactorily tested against those in a real experiment. Furthermore, numerical simulations are extremely limited by hardware restrictions and the scalability of the algorithms, so they usually operate in a smaller parameter range than laboratory experiments. Ultimately, it might be objected that there exist diverse possible causes of error such as programming mistakes, compiler failures, insufficient spatial resolution or problems related to numerical methods, which may lead to misleading results.

Nevertheless, on the basis of the preceding reasoning, it is not difficult to realize that numerical simulations and experiments are complementary activities which mutually benefit one another. Numerical simulations in simple laboratory models may suggest new measurements or experiments and set the bounds of the parameter range where experiments are going to be performed. They allow to explore in greater detail the areas of the parameter space where changes in the dynamics are observed, facilitating the understanding of the underlying physical mechanisms as well as the sort of bifurcations taking place. Most importantly, the comparison between simulations and experiments is essential to detect possible deficiencies either in experimental facilities or numerical codes, which may significantly alter the results of the investigation. Improving this mutual calibration process is the primary objective of this thesis. In particular, simulations have mainly focused on identifying potential sources of discrepancies between numerical and laboratory experiments in the particular case of rotating fluids in presence of temperature gradients. Let us briefly summarize the topics to be developed in subsequent chapters.

Experimental imperfections result in imperfect symmetries which often modify the dynamical behavior of the idealized systems employed in numerical simulations. In SO(2) equivariant systems, such as rotating cylinders or Taylor–Couette flows, imperfect symmetries manifest in the emergence of the so-called pinning region, in which rotating waves with precession frequency near zero are stopped by the imperfections and turn into steady states (Abshagen *et al.*, 2008). Numerical simulations are unable to capture the pinning region unless additional changes in the boundary conditions, modeling the effect of imperfections, are introduced (Pacheco *et al.*, 2011). This subject is addressed in chapter 3. An analysis of the symmetry-breaking of the normal form associated

with a Hopf bifurcation of zero frequency is presented. It is shown that the pinning region results from the breaking of the rotational invariance as a consequence of the imperfections. This phenomenon is illustrated in the case of rotating Rayleigh-Bénard convection, where the SO(2) symmetry of the system is broken by imposing a linear temperature profile at the top lid. It is worth noting that, unlike other pinning regions in fluid dynamics problems, this occurs in a region of the parameter space where the bifurcations are subcritical.

In some cases discrepancies between experiments and numerical simulations occur because the governing equations do not include all physical mechanisms which play significant dynamical roles. A typical example in rotating systems is the absence of the centrifugal term in the Navier-Stokes equations. Barcilon & Pedlosky (1967) warned about neglecting the centrifugal buoyancy: "Many theories proceed under the assumption that the centrifugal force is sufficiently small compared to the gravitational force... With this approximation, the basic stratification is linear and there is no resulting relative motion. Nevertheless, in any experiment some effect of the centrifugal force will be felt, and for rapidly rotating fluids the effect may not be negligible." In fact, they included the centrifugal term in their analysis. The reasons for not including this term are clear: without centrifugal buoyancy the base state is trivial (fluid at rest), and the domain can be considered horizontally periodic, allowing the use of standard analytical tools and low-dimensional models in infinite domains. Including the centrifugal term makes some treatments more difficult: the base state is not trivial and exhibits a centrifugally-driven large-scale circulation that is not amenable to an explicit closed form. Moreover, the centrifugal buoyancy depends explicitly on the radial coordinate, and this invalidates any horizontal periodicity assumption. The parameter which measures the relative strength between centrifugal and gravitational buoyancy is the rotational Froude number, $F = \mathbf{\Omega}^2 L/g$, where $\mathbf{\Omega}$ is the angular velocity, L is a characteristic dimension of the container and g is the acceleration due to gravity. There have been many studies on rotating convection neglecting centrifugal buoyancy, and the results are very often satisfactory and in good agreement with experiments. If the Froude number is small, it seems reasonable to neglect centrifugal buoyancy, and in fact many experiments have been designed and conducted so that the Froude number is very small. However, the centrifugal buoyancy is the only force acting in radial direction, so it is always the dominant force in this direction. The gravitational buoyancy acts orthogonally, in the axial direction, and so comparing their relative magnitudes (using F for example) is not necessarily a good criterion for determining if one dominates over the other (Barcilon & Pedlosky, 1967; Homsy & Hudson, 1969; Hart, 2000; Rubio *et al.*, 2009). From the numerical simulation

point of view, the inclusion of the centrifugal buoyancy term requires a minimal effort, both in code preparation and execution. For these reasons, the centrifugal term should always be included in the simulations (Randriamampianina *et al.*, 2006), and whether it is dynamically significant or not should be determined a posteriori.

The manner in which centrifugal effects are incorporated into the governing equations requires special consideration. Flows with small density variations are customarily approximated as incompressible whilst retaining the leading order effects due to the density variations, thus avoiding issues associated with acoustic waves. The classical approach is the Boussinesq approximation which was originally motivated by the desire to account for gravitational buoyancy effects. Nevertheless, in commonly used formulations of the Boussinesq approximation centrifugal buoyancy effects related to differential rotation, as well as strong vortices in the flow, are neglected. These may play an important role in rapidly rotating flows, such as in astrophysical and geophysical applications, and also in turbulent convection. In chapter 4 a straightforward approach resulting in a Boussinesq-type approximation that consistently accounts for centrifugal effects is provided. Its application to the accretion-disk problem is discussed. The new approach is numerically compared to the typical one in fluid flows confined between two differentially heated and rotating cylinders. The results justify the need of using the proposed approximation in rapidly rotating flows.

Laboratory experiments are usually designed to work in parameter ranges as close as possible to the real context they seek to approximate. Thus, experimental results can be extrapolated to the real flow with some degree of success. Yet, economic and technological limitations sometimes prevent the experiments from functioning in the desired ranges. For example, although experiments on accretion disks operate with very high rotational speeds $\mathrm{Re} \sim O(10^6)$, in real accretion disks $\mathrm{Re} \sim O(10^{12})$ are expected (Paoletti & Lathrop, 2011; Ji *et al.*, 2006), thus the results must be carefully interpreted and extrapolated. This problem becomes worse in numerical simulations where it is often impossible to reproduce the full operating range of a laboratory experiment. An accurate numerical computation of the boundary layers, which in rotating fluids are refer to as Ekman and Stewartson layers, involves a substantial increase in computational cost as the values of the control parameters are increased. The assumption of axial periodicity provides a way to reduce the computational needs and simulate higher and more significant values of the control parameters. In doing so, the Ekman layers that form at the axial end walls completely disappear, and the Stewartson layers at the lateral boundaries merge with the base flow. Moreover, under this assumption variables can be expanded as a Fourier series in axial direction, which greatly simplifies the numerical

approach, allowing for faster and more efficient solvers. Nevertheless, boundary layers play a crucial dynamical role in many fluid systems (Avila *et al.*, 2008). It is therefore essential to identify how the boundary layers can modify the dynamics of axially periodic systems before comparisons with real experiments are established.

Such analysis is considered in chapter 5 for the case of a laterally heated differentially rotating annulus, which is a canonical experiment for the study of baroclinic flows and heat transfer in engineering. The onset of instabilities and turbulence in such flows by using both periodic and physical no-slip boundary conditions in the axial direction are investigated. It is shown that geometry and axial end walls play a key role in determining the dynamics of baroclinic flows and the mechanisms of heat transfer. First, a setup with rotating inner cylinder and fixed outer cylinder, which is a simple model for cooling of rotating machinery, has been considered. If the lateral heating is small the dynamics with periodic and no-slip boundary conditions is very similar. However, as the temperature gradient increases there is in the latter a significant stabilizing effect due to the combination of frictional effects and stable vertical stratification resulting from the Ekman boundary layers. Second, a setup with cylinders and end walls rotating at the same angular speed, which is a simple model for atmospheric flows, is presented. Here even the laminar flow is significantly altered by the axial end walls and the mechanisms of transition are entirely different when periodic boundary conditions are used.

Unlike previous chapters simulations presented in chapter 6 do not focus on the comparison between numerical simulations and experiments, but are intended to complement the results of a series of laboratory experiments (Abshagen *et al.*, 2012; von Stamm *et al.*, 1996; Gerdts *et al.*, 1994). The flow is confined in a wide gap ($\eta = 0.5$) isothermal Taylor–Couette system, with a rotating inner cylinder and length-to-gap aspect ratio restricted to $0.86 < \frac{\Gamma}{N} < 0.95$, being N the total number of vortices. For these values a complex experimental bifurcation scenario, differing from the classical Ruelle-Takens route to chaos, has been reported. The wavy vortex flow becomes quasi-periodic due to an axisymmetric mode that occurs at a very low frequency. This mode plays a key role in the dynamics of the system, leading to the occurrence of chaos via a period-doubling scenario. Further increasing the rotation of the inner cylinder results in the appearance of a new flow pattern which is characterized by large amplitude oscillations localized in some of the vortex pairs. The purpose of chapter 6 is to study numerically the dynamics of these axially localized states, paying special attention to the transition to chaos. Frequency analysis from time series simultaneously recorded at several points has been applied in order to identify the bifurcations taking place. It has been found that the very low frequency mode is also essential to explain the behavior associated with the

transitions either between different axially localized states or to the chaotic regime.

A wide range of mathematical tools such as linear stability analysis, fully non-linear computations, Newton methods, continuation methods or time-series analysis has been applied to carry out the aforementioned studies. This, together with the variety of experimental setups considered along the thesis, has required implementation of several numerical codes. The governing equations, numerical methods, temporal and spatial discretizations, paralellization strategies and other relevant features of these numerical tools are comprehensively described in chapter 2.

Finally, the main results of the thesis, along with some notes about their relevance concerning future works on rotating fluids, are collected in chapter 7.

CHAPTER 2

GOVERNING EQUATIONS AND NUMERICAL METHODS

2.1 Introduction

A significant fraction of the time spent to complete this thesis has been invested in designing, implementing and verifying the numerical tools needed to carry out the computations. Some of them are mere extensions of previously existing numerical codes in order to include the effect of the temperature (those described in 2.3 and 2.4), or modifications of some subroutines to implement new numerical methods, as is the case of the continuation code for rotating waves in cylindrical cavities exposed in 2.6. In these cases, we do not provide an extensive description of the code, but briefly mention the numerical method utilized and highlight the novelties introduced. The reader is referred to the literature of the original code for a comprehensive overview. In this chapter we pay special attention to the parallel code implemented to solve three dimensional flow in a finite annular cavity which, in contrast to the other numerical tools, has been fully developed during this thesis, and is responsible for a substantial amount of the results shown in subsequent chapters. Section 2.2 offers a detailed description of the spatial and temporal discretizations, numerical methods and parallelization strategy chosen to implement this numerical tool.

All codes have been written in FORTRAN, either 90 or 77, and due to the simplicity of the geometries considered (see figure 1.6), we use in all cases pseudo-spectral methods that allow us for a fast convergence with excellent error properties. We only study the dynamics of incompressible fluids so that the equation $\nabla \cdot \mathbf{v} = 0$, where $\mathbf{v}$ is the velocity vector, is satisfied in all cases. The rest of governing equations only differ between codes considering cylindrical and annular cavities, since different reference frames and nondimensionalization have been used. The boundary conditions vary among the different systems studied in each chapter and are conveniently specified in each case.

2.2 Solver for the three-dimensional flow in a finite annular cavity with a radial temperature gradient.

This code solves the Navier-Stokes equations in primitive variables for the flow enclosed in a finite annular domain, including the influence of the thermal gradient caused by the

temperature difference between the inner and outer walls.

2.2.1 Governing equations

We consider an incompressible fluid of kinematic viscosity ν and density ρ confined between two concentric cylinders of length h and inner and outer radii r_i and r_o. A thermal gradient in radial direction is set due to the temperature difference between the cylinders ΔT. The system is non-dimensionalized using the gap width, $d = r_o - r_i$, as the length scale, the viscous time, d^2/ν, as the time scale, ΔT as the temperature scale and $(\nu/d)^2$ as the pressure scale. The Boussinesq approximation is used to include the effect of the density variation due to changes in the temperature. However, we do not use the classical Boussinesq approximation, but a new approach which also includes the centrifugal effects and will be extensively discussed in chapter 4. The dimensionless governing equations are

$$(\partial_t + \mathbf{v} \cdot \nabla)\mathbf{v} = -\nabla p + \nabla^2 \mathbf{v} + GT\hat{\mathbf{z}} + \epsilon T \mathbf{v} \cdot \nabla \mathbf{v}, \tag{2.1a}$$

$$(\partial_t + \mathbf{v} \cdot \nabla)T = \sigma^{-1} \nabla^2 T, \tag{2.1b}$$

$$\nabla \cdot \mathbf{v} = 0, \tag{2.1c}$$

where $\mathbf{v}$ denotes the velocity field vector and T is the deviation of the temperature with respect to the mean temperature T_c. Cylindrical coordinates (r, θ, z) are used. The geometry of the container is fixed with the dimensionless geometric parameters

$$\text{Radius ratio} \qquad \eta = r_i/r_o, \tag{2.2a}$$

$$\text{Aspect ratio} \qquad \Gamma = h/d \tag{2.2b}$$

Three additional dimensionless numbers appear:

$$\text{Grashof number} \qquad G = \alpha g \Delta T d^3/\nu^2, \tag{2.3a}$$

$$\text{relative density variation} \qquad \epsilon = \alpha \Delta T = \Delta\rho/\rho_0, \tag{2.3b}$$

$$\text{Prandtl number} \qquad \sigma = \nu/\kappa, \tag{2.3c}$$

where κ and α are respectively the thermal diffusivity and the coefficient of volume expansion of the fluid, $\Delta\rho$ is the density variation associated with a temperature change of

ΔT and g is the gravity acceleration which is assumed to be uniform and vertical. The term $\epsilon T\mathbf{v}\cdot\nabla\mathbf{v}$ accounts for the centrifugal buoyancy, including secondary effects stemming from differential rotation or strong internal vorticity. For the study of isothermal flows, as is the case in chapter 6, it is enough to set G and ϵ to zero and switch off the equation 2.1b.

The Reynolds number enters the equations through the boundary conditions and it is typically used as a control parameter.

$$\mathrm{Re} = \frac{\Omega r d}{\nu}, \tag{2.4}$$

where Ω is the angular velocity of the system at the radial position r.

When the end walls are steady, the boundary conditions are discontinuous at the junction where the end walls meet the rotating cylinder, $(r = r_i, z = \pm\Gamma/2)$. In a physical experiment there are small but finite gaps at these junctions where the azimuthal velocity adjusts rapidly to zero. For an accurate use of spectral techniques, a regularization of these discontinuities is implemented of the form:

$$v(r,\theta,\pm\Gamma/2,t) = Re\ \exp\big(\frac{r_i - r}{\beta}\big), \tag{2.5}$$

where β is a small parameter that mimics the small physical gap (we have used $\beta = 0.01$). The use of $\beta \neq 0$ regularizes the otherwise discontinuous boundary conditions; see Lopez & Shen (1998) for further details on the use of this technique in spectral codes.

2.2.2 Numerical formulation

Spatial discretization

The spatial discretization of the set of equations in 2.1 is accomplished via a Galerkin-Fourier expansion in θ and Chebyshev collocation in r and z

$$r_i = \frac{1}{2}\big(\cos(i\pi/L) + r_i + r_o\big),\ i = 0,\cdots,L \quad z_j = \frac{h}{2}\cos(j\pi/N),\ j = 0,\cdots,N. \tag{2.6}$$

so that the variables of the problem are expressed as

$$(u,w,p,T)(r,\theta,z) = \sum_{l=0}^{L}\sum_{n=0}^{N}\sum_{m=-M}^{M} a_{l,n,m}T_l(r)T_n(z)e^{im\theta} = \sum_{M=-M}^{M} F_m(r,z)e^{im\theta} \tag{2.7a}$$

$$v(r,\theta,z) = i\sum_{l=0}^{L}\sum_{n=0}^{N}\sum_{m=-M}^{M} a_{l,n,m}T_l(r)T_n(z)e^{im\theta} = i\sum_{M=-M}^{M} F_m(r,z)e^{im\theta} \tag{2.7b}$$

where L and N denote respectively the number of collocation points in the radial and axial directions and M stands for the number of Fourier modes. The different choice of v allows to decompose each equation in (2.1) into two independent equations, containing the real and imaginary parts of the complex functions $F_m(r,z)$. Therefore, a system of Poisson and Helmholtz equations results for each Fourier mode, being the total number of equations to be solved $M\times2\times4$. The Helmholtz equations for u and v are then decoupled, according to Orszag & Patera (1983), by inserting the new variables $u_+ = u + iv$ and $u_- = u - iv$. Note that due to this decomposition, the boundary conditions for the radial and azimuthal velocities must be of the same type. The resulting system of equations is efficiently solved by using a complete diagonalization of the operators in both the radial and axial directions. This technique, which was first described by Zhao & Yedlin (1994), requires the previous computation of the eigenvalues and eigenvectors of these matrices, which is performed as a preprocessing step before the integration begins.

Temporal scheme

The governing equations are advanced in time via a second-order time-splitting method (Hughes & Randriamampianina, 1998; Mercader *et al.*, 2010) that results in the following temporal scheme

$$\frac{3\mathbf{v}^{i+1} - 4\mathbf{v}^{i} + \mathbf{v}^{i-1}}{2\Delta t} + 2N_L^i(\mathbf{v}) - N_L^{i-1}(\mathbf{v}) = -\nabla p^{i+1} + \Delta\mathbf{v}^{i+1} + GT^{i+1}\hat{e_z}, \tag{2.8a}$$

$$\frac{3T^{i+1} - 4T^{i} + T^{i-1}}{2\Delta t} + 2N_L^i(T,\mathbf{v}) - N_L^{i-1}(T,\mathbf{v}) = \sigma^{-1}\Delta T^{i+1} \tag{2.8b}$$

where Δt denotes the time step and N_L refers to the non-linear terms. This is a semi-implicit method, with N_L being treated explicitly, whereas the laplacian operator Δ and the rest of linear terms are considered implicitly. The fractional steps carried out at each iteration are listed below

1. Solve the system of Helmholtz equations resulting from (2.1b) to obtain T^{i+1}

$$\sigma^{-1}(\nabla^2 - \frac{3}{2\Delta T})T^{i+1} = 2N_L^i(\mathbf{v},T) - N_L^{i-1}(\mathbf{v},T) - \frac{4T^i - T^{i-1}}{2\Delta t} \tag{2.9}$$

2. Obtain a predictor for the pressure $\hat{p}^i$ from the Poisson equation

$$\partial\hat{p}^i = \nabla \cdot [-2N_L^i(\mathbf{v}) + N_L^{i-1}(\mathbf{v}) + GT^{i+1}\hat{e_z}] \tag{2.10}$$

with a consistent Neumann boundary condition obtained from (2.8a)

$$\partial_n\hat{p}^i|_{r=r_{i,o}} = n \cdot [-\frac{3\mathbf{v}^{i+1} + 4\mathbf{v}^i - \mathbf{v}^{i-1}}{2\Delta t} - 2N_L^i(\mathbf{v}) + N_L^{i-1}(\mathbf{v}) + GT^{i+1}\hat{e_z}]_{r=r_{i,o}} \tag{2.11}$$

3. Solve the system of Helmholtz equations resulting from (2.1a) to obtain a predictor for the velocity field $\hat{\mathbf{v}}^{i+1}$

$$(\nabla^2 - \frac{3}{2\Delta\mathbf{v}})\hat{\mathbf{v}}^{i+1} = \nabla\hat{p}^i + 2N_L^i(\mathbf{v}) - N_L^{i-1}(\mathbf{v}) - \frac{4\mathbf{v}^i - \mathbf{v}^{i-1}}{2\Delta t} - GT^{i+1}\hat{e_z} \tag{2.12}$$

4. The velocity is corrected to ensure the free divergence condition $\nabla \cdot \mathbf{v}^{i+1}$ in all points of the fluid domain. This is accomplished by means of an intermediate variable $\phi = \frac{2\Delta t}{3}(p^{i+1} - \hat{p}^i)$ which leads to a Poisson equation

$$\Delta\phi = \mathbf{v}^{i+1} \tag{2.13}$$

with a homogeneous Neumann boundary condition. After solving (2.13) velocity and pressure are updated as follows

$$p^{i+1} = \hat{p}^i + \frac{3\phi}{2\Delta T} \tag{2.14a}$$

$$\mathbf{v}^{i+1} = \hat{\mathbf{v}}^{i+1} - \nabla\phi \tag{2.14b}$$

5. The non-linear terms are computed from the values just obtained, $\mathbf{v}^{i+1}$ and T^{i+1}, and a new iteration starts.

Parallelization strategy

A *MPI* (Message Passing Interface) parallelization of the code has been accomplished by distributing the total number of azimuthal nodes $nn = 2 * M$ among the number of processors N_p used in each calculation. This arrangement, which is known as slab decomposition, is possible because the system of equations resulting from the discretization is independent for each Fourier mode. In other words, for each variable, $\mathbf{v}$, T and p, the grid points $(nr, nz, nn) = (L + 1, N + 1, 2 * M)$ are divided into N_p submatrices of the same size $(nr * nz, nn/N_p)$ which are assigned to each processor (see left hand side of figure 2.1) so that the mathematical operations regarding each subset of

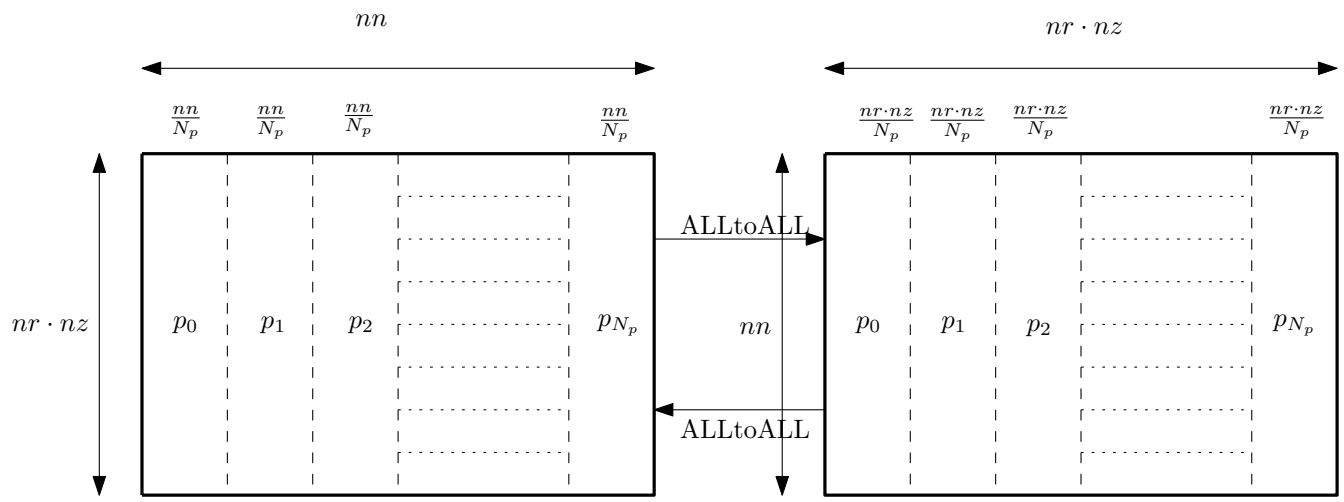

Figure 2.1: Schematic of the distribution of the grid points (nr, nz, nn) into the N_p processors used in each calculation (left hand side matrix) and matrix resulting from the global transposition using MPI_ALLtoALL statements (right hand side)

data are carried out independently by the corresponding processor, thus avoiding the very time consuming communication among processors. Nevertheless, communication is sometimes useful to improve the efficiency in some parts of the code. This is the case of the non-linear term calculation, which is performed in physical space through a pseudospectral technique involving the use of fast Fourier transforms (FFTW) to convert the spectral coefficients into values in physical space. An efficient use of FFTW requires all azimuthal nodes to be contained in each processor, therefore it is needed to transpose the global matrix $(nr * nz, nn)$ corresponding to each variable of the problem, and then distribute it again as submatrices $(nn, nr * nz/N_p)$ for each processor, as shown in the right hand side of figure 2.1. This global matrix transposition, which would otherwise be a major bottleneck, is efficiently performed by using all-to-all communication among processors. After the non-linear term calculation is complete, the matrices are transposed back, again using all-to-all communication, to proceed solving the equations. As a consequence of this methodology, the total number of processors to be used not only has to be divisible by nn, but also by $nr * nz$. Since $nr * nz$ is typically larger than nn in our problems, the maximum number of parallel tasks to be perform must be $\leq nn$. These collective communications restrict the code scalability, however this is compensated with the gain in efficiency when using FFTW. In order to check the right performance and scalability of the code we have done a strong scaling test, consisting in measuring the time spent by the code in 10 iterations of the time stepper for two different spatial resolutions, (a) $(nr, nz, nn) = (106, 512, 256)$ and (b) $(nr, nz, nn) = (106, 512, 512)$, as the number of processors is increased. The results of

this test, which was performed in a HPC (high-performance-computing) platform using 4 nodes with 80 processors each interconnected with Infiniband, are shown in figure 2.2. The black line (circles) denotes the scaling for the lowest spectral resolution $nn = 256$, whereas the red line (squares) represents the case with $nn = 512$. If the code maintained 100% parallel efficiency, the computation time would scale as $1/N_P$. This ideal situation is also reflected in figure 2.2 through the green and blue lines for $nn = 256$ and $nn = 512$ respectively. Note that a log-log diagram has been chosen to make easier the comparison between real and ideal behaviors. It is observed an excellent scaling as long as the number of processors, which in this case is equivalent to the number of MPI tasks, is less or equal than 80, that is, while only a single machine is used. When N_p is increased above 80, and thus more than one machine come to play, the time consumed in collective communications becomes much longer than the computation time saved when reducing the amount of data to be handled for each processor, resulting in a deviation from the ideal scaling. This is a hardware-related limitation concerning the speed with which data can be transmitted from one machine to the other, therefore it is expected a substantial improvement of the scalability in other platforms with a higher bandwidth. It is also important to note that since tests are not performed over a realistic computation time, the possible overhead occurring during the course of the run, which might be a significant part of the real work, is not considered. The parallel efficiency is extremely dependent on the problem size. Indeed, if we compare the scaling for both resolutions, a slightly different behavior can be seen in both cases as N_P is increased. For $nn = 256$, the amount of time consumed in 10 iterations of the numerical integrator progressively increases with N_p. Nevertheless, the shortest time in the case of $nn = 512$ is obtained when $N_P = 256$. Despite the scaling is not good (there is a sharp difference with the ideal scaling and little time is saved with respect to $N_P = 64$), this indicates that as the spectral resolution increases and consequently the number of equations to be solved by each processor becomes larger, computation time overtakes communication time as the biggest bottleneck, resulting in an improvement of the code scalability. The performance of the code could be significantly improved with the inclusion of *OPENMP* directives to parallelize the operations inside each MPI task (Shi *et al.*, 2015). This technique allows for overlapping calculations and communications tasks, which substantially increase the code scalability.

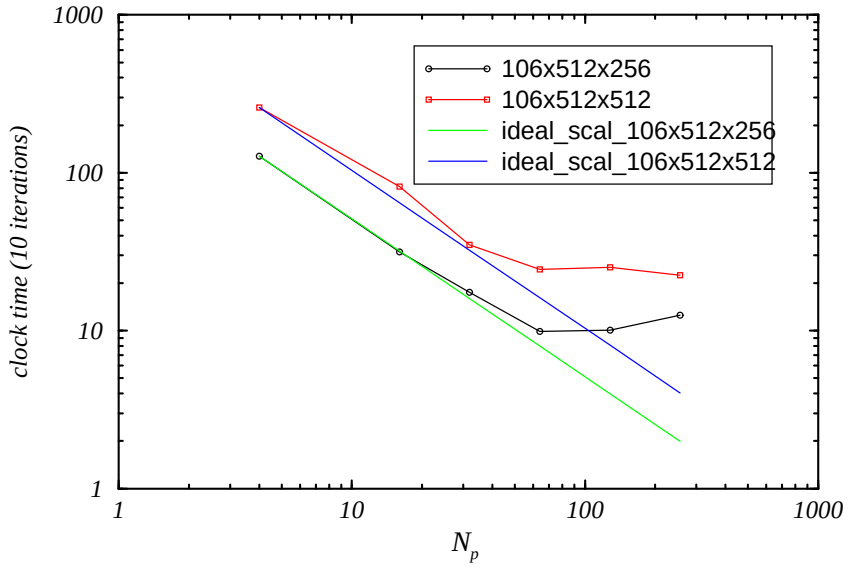

Figure 2.2: Code scalability test. Time spent in 10 iterations of the time stepper vs number of processors N_p.

Validation tests

Multiple tests have been performed to verify the scientific validity of the results. There exist a large number of numerical studies which consider the isothermal case, so it is easier to establish a direct comparison with previously reported results in this case. The first validation was the onset of Taylor vortices for several values of η, obtaining an excellent agreement with the analytical expression given by Esser & Grossmann (1996). As a second test, we have satisfactorily reproduced the results in Marques & Lopez (2006), where the onset of three-dimensional states in a small aspect ratio ($\Gamma = 1$) Taylor–Couette system was numerically investigated. The figure 2.3 illustrates one of these tests, showing an isosurface of angular momentum for a rotating wave with azimuthal wavenumber $n = 2$ at $\mathrm{Re} = 1200$, which was originally shown in figure 9 of Marques & Lopez (2006). The onset of instability for the experimental setups used in Maryland and Princeton to carry out the study of quasi-Keplerian flows has also been computed. The table 2.1 shows these values, which are in agreement with those reported in Avila (2012). Finally, the results described in chapter 6 can be also considered as an excellent validation test, since they accurately reproduce the bifurcation scenario obtained in a series of experiments.

The non-isothermal version of the code has been verified by reproducing the results of the linear stability analysis in Lewis & Nagata (2004), some of which are shown in table 2.2, as well as some of the flow transitions reported in Kuo & Ball (1997), which will be

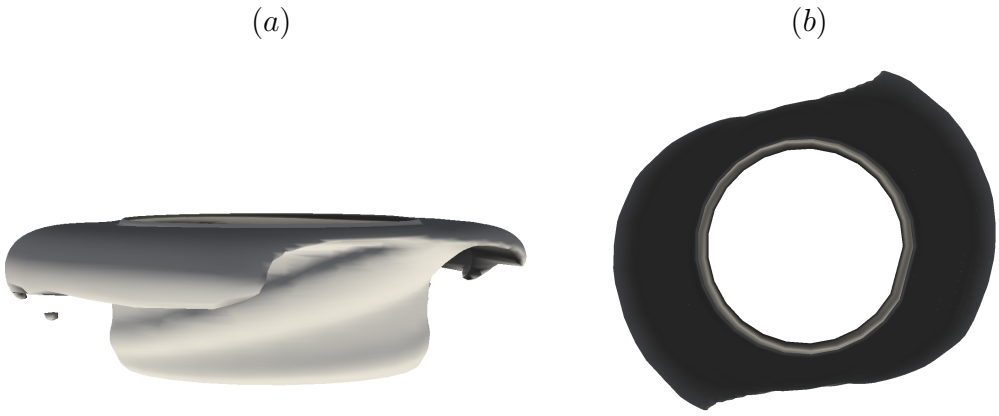

Figure 2.3: Isosurface of angular momentum $rv = 340$ for a $n = 2$ rotating wave at $\mathrm{Re} = 1200$. This state was reported in Marques & Lopez (2006), see figure 9, and has been used here to validate the numerical code. (a) Lateral view. (b) Top view.

	Validation test (Re_s)	Avila (Re_s)
Maryland	349	352
Princeton	1146	1448

Table 2.1: Onset of instability (Re_s, Reynolds shear number) for quasi-Keplerian flow in the experimental facilities of Maryland and Princeton. Comparison with the results in Avila (2012).

discussed in chapter 5.

Ω	Validation test (ΔT)	Lewis and Nagata (ΔT)
0.8	0.371	0.375
1.0	0.355	0.378
0.65	0.403	0.411

Table 2.2: Critical stability values for the onset of instability in a baroclinic annulus. Ω and ΔT are angular velocity and temperature difference between the cylinders respectively. Comparison with the values reported in Lewis & Nagata (2004). Note that finite differences of second order are used in Lewis & Nagata (2004), so for the same resolution there exist small differences between the values obtained in both cases.

2.3 Solver for the three dimensional flow in an infinite annular cavity with a radial temperature gradient

This solver is an extension of the code written by Shi *et al.* (2015) to consider the effect of a radial thermal gradient in an axially periodic Taylor Couette flow. The governing equations, with the obvious exception of the axial boundary condition, and the temporal scheme are the same as in 2.2. The main difference between both codes lies in the spatial discretization. Since the axial and azimuthal directions are periodic, the variables are expanded in Fourier series along these directions,

$$(u, v, w, T, p)(r, \theta, z) = \sum_{l=-L}^{L} \sum_{n=-N}^{N} a_{l,n}(r) e^{ink_\theta \theta} e^{ilk_z z}, \tag{2.15}$$

where k_θ and k_z are respectively the azimuthal and axial wavenumbers. Four-order central finite differences are used to approximate the radial derivatives, with the radial nodes distributed as

$$r_i = \frac{1+\eta}{2(1-\eta)} + \frac{sin^{-1}(-\alpha cos(\pi i/M))}{2sin^{-1}\alpha} \qquad , i = 0, \cdots, M \tag{2.16}$$

The resulting system of Helmholtz and Poisson equations is composed of banded matrices which are easily solved using the LU method. The LU decomposition of the operators is accomplished in a preprocessing stage, so the total number of operations required to solve the M-dimensional system of equations at each time step is $O(M)$. This is a significant difference with the solver in 2.2, where the diagonalization technique used to deal with the equations involves using $O(M^2)$ operations in both radial and axial direction. A hybrid OPENMP-MPI strategy was used to parallelize the code. The MPI

tasks distribution was performed with a slab decomposition slightly different to that illustrated in figure 2.1 (see figure 2 in Shi *et al.* (2015)) . Each MPI task is additionally parallelized using OPENMP directives, which allows for a considerable increase in the code scalability. Adding the temperature equation is straightforward and does not pose any inconvenience to maintain the performance of the code, apart from the subsequent increase in the execution time, which is about 20% longer than in the original code. The code has been satisfactorily tested by comparison with the linear stability results computed with the code described below.

2.4 Linear stability analysis in an axially periodic annular cavity with a radial temperature gradient

The linear stability can be easily infer from the modal kinetic energy in non-linear calculations, and thus we could use the code described in 2.3 to this effect, nevertheless the axial periodicity assumption notably simplifies the numerical approach, allowing for a straightforward resolution of the eigenvalue problem resulting from the linearization of (2.1). This hugely reduces the computational resources and time required in the computations, and allows us to reach very large values of the control parameters, which would otherwise be unachievable. The main aspects of the code implemented to this end are outlined below.

2.4.1 Basic flow

An analytical solution for the base flow can be found by assuming only radial dependence for the variables of the problem. We also use the zero axial mass flux condition to fix the axial pressure gradient, i.e.:

$$\int_{r_i}^{r_o} r w_b(r) dr = 0. \tag{2.17}$$

The resulting steady basic flow is given by:

$$u_b(r) = 0, \tag{2.18a}$$

$$v_b(r) = Ar + \frac{B}{r}, \tag{2.18b}$$

$$w_b(r) = G\bigg(C(r^2 - r_i^2) + \Big(C(r_o^2 - r_i^2) + \frac{1}{4}(r_o^2 - r^2)\Big)\frac{\ln(r/r_i)}{\ln\eta}\bigg), \tag{2.18c}$$

$$T_b(r) = \frac{1}{2} + \frac{\ln(r/r_i)}{\ln\eta}, \tag{2.18d}$$

$$p(r,z) = p_o + G\Big(4C + \frac{1}{2} - \frac{1}{\ln\eta}\Big)z + \int_{r_i}^{r}\big(1 - \epsilon T_b(r)\big)v_b^2(r)\frac{dr}{r}, \tag{2.18e}$$

where (u, v, w) are the radial, azimuthal and axial components of the velocity field, and cylindrical coordinates (r, θ, z) are being used. v_b is the azimuthal velocity for the classical Taylor–Couette problem (Chandrasekhar, 1961), whereas w_b and T_b correspond to convection in a conductive regime and appeared for the first time in (Choi & Korpela, 1980). The pressure varies linearly with the axial coordinate z, but the pressure gradient depends only on r, and therefore it is periodic in the axial direction. This axial pressure gradient mimics the presence of distant endwalls in any real situation, by enforcing the zero mass flux constraint (2.17). It is possible to give an explicit closed expression for p by integrating (2.18e), but it is quite involved and it does not appear in the problem solution. The expressions for the parameters A, B and C are:

$$A = \frac{\mathrm{Re}_o - \eta\mathrm{Re}_i}{1+\eta}, \qquad B = \eta\frac{\mathrm{Re}_i - \eta\mathrm{Re}_o}{(1-\eta)(1-\eta^2)}, \tag{2.19}$$

$$C = -\frac{4\ln\eta + (1-\eta^2)(3-\eta^2)}{16(1-\eta^2)\big((1+\eta^2)\ln\eta + 1 - \eta^2\big)}, \tag{2.20}$$

where (2.19) define the pure rotational flow in the azimuthal coordinate and C gives the axial component of the velocity field. The non-dimensional radii of the cylindrical walls are given by $r_i = \eta/(1-\eta)$, $r_o = 1/(1-\eta)$. Note that the presence of the new centrifugal buoyancy term, proportional to ϵ, does not modify the basic flow's velocity field, but only its pressure.

2.4.2 Linearized equations

We perturb the basic flow with infinitesimal perturbations which vary periodically in the axial and azimuthal directions,

$$\mathbf{v}(r,\theta,z,t) = \mathbf{v_b}(r) + e^{i(n\theta+kz)+\lambda t}\mathbf{u}(r), \tag{2.21a}$$

$$T(r,\theta,z,t) = T_b(r) + e^{i(n\theta+kz)+\lambda t}T'(r), \tag{2.21b}$$

where $\mathbf{v_b} = (0, v_b, w_b)$ and $T_b(r)$ correspond to the base flow (2.18); $\mathbf{u}(r) = (u_r, u_\theta, u_z)$ and $T'(r)$ are the velocity and temperature perturbations, respectively. The boundary conditions for both $\mathbf{u}$ and T' are homogeneous: $\mathbf{u}(r_i) = \mathbf{u}(r_o) = T'(r_i) = T'(r_o) = 0$. The axial wavenumber k and the azimuthal mode number n define the shape of the disturbance. The parameter λ is complex. Its real part λ_r is the perturbation's growth rate, which is zero at critical values, and its imaginary part λ_i is the oscillation frequency of the perturbation.

Using the decomposition (2.21) in the equations (2.1) and neglecting high-order terms, we obtain an eigenvalue problem, with eigenvalue λ. It reads

$$\begin{aligned}
\lambda u_r = {} & \frac{1}{r}\frac{\partial}{\partial r}(r\frac{\partial u_r}{\partial r}) - u_r[\frac{n^2+1}{r^2} + k^2 + i(\frac{nv_b}{r} + kw_b)(1-\epsilon T_b)] \\
& + \frac{2v_b}{r}(1-\epsilon T_b)u_\theta - \frac{2in}{r^2}u_\theta - \frac{\epsilon v_b^2}{r}T', \qquad (2.22a) \\
\lambda u_\theta = {} & \frac{1}{r}\frac{\partial}{\partial r}(r\frac{\partial u_\theta}{\partial r}) - u_\theta[\frac{n^2+1}{r^2} + k^2 + i(\frac{nv_b}{r} + kw_b)(1-\epsilon T_b)] \\
& - (\frac{\partial v_b}{\partial r} + \frac{v_b}{r})(1-\epsilon T_b)u_r + \frac{2in}{r^2}u_r, \qquad (2.22b) \\
\lambda u_z = {} & \frac{1}{r}\frac{\partial}{\partial r}(r\frac{\partial u_z}{\partial r}) - u_z[\frac{n^2}{r^2} + k^2 + i(\frac{nv_b}{r} + kw_b)(1-\epsilon T_b)] \\
& + \frac{\partial w_b}{\partial r}(\epsilon T_b - 1)u_r + GT', \qquad (2.22c) \\
\lambda T' = {} & \frac{1}{\sigma r}\frac{\partial}{\partial r}(r\frac{\partial T'}{\partial r}) - T'[\frac{1}{\sigma}(\frac{n^2}{r^2} + k^2) + i(\frac{nv_b}{r} + kw_b)] - \frac{\partial T_b}{\partial r}u_r. \qquad (2.22d)
\end{aligned}$$

Note that here the continuity equation and pressure terms are omitted because the Petrov–Galerkin method chosen to solve the resulting system of equations automatically satisfies the continuity equation and eliminates the pressure by using a proper projection (see next subsection).

2.4.3 Numerical method

In order to solve numerically the eigenvalue problem described in the previous subsection, a spatial discretization of the domain must be made. This is accomplished by projecting the equations (2.22) onto a basis carefully chosen to simplify the process,

$$V_3 = \{\mathbf{v} \in (\mathscr{L}_2(r_i, r_o))^3 \mid \nabla \cdot \mathbf{v} = 0,\ \mathbf{v}(r_i) = \mathbf{v}(r_o) = 0\}, \qquad (2.23)$$

where $(\mathscr{L}_2(r_i, r_o))^3$ is the Hilbert space of square integrable vectorial functions defined on the interval (r_i, r_o), with the inner product

$$\langle \mathbf{v}, \mathbf{u} \rangle = \int_{r_i}^{r_o} \mathbf{v}^* \cdot \mathbf{u}\ r dr, \qquad (2.24)$$

where * denotes the complex conjugate. For any $\mathbf{v} \in V_3$ and any function p, using the incompressibility condition, the boundary conditions and integrating by parts,

$$\langle \mathbf{v}, \nabla p \rangle = \int_{r_i}^{r_o} (\mathbf{v}^* \cdot \nabla p) r dr = \int_{r_i}^{r_o} r v_r^* \partial_r p \, dr = r p v_r^* |_{r_i}^{r_o} - \int_{r_i}^{r_o} p \partial_r (r v_r^*) dr = 0. \quad (2.25)$$

This consideration allows us to eliminate the pressure from the equations as we project them onto the basis (Canuto *et al.*, 2007). Moreover, the continuity equation is satisfied by definition of the space V_3. For the temperature perturbation the appropriate space is

$$V_1 = \{ f \in \mathscr{L}_2(r_i, r_o) \mid f(r_i) = f(r_o) = 0 \}. \quad (2.26)$$

We expand the variables of the problem as follows

$$\mathbf{X} = \begin{bmatrix} \mathbf{u}(r) \\ T'(r) \end{bmatrix} = \sum_j a_j \mathbf{X}_j \qquad \mathbf{X}_j \in V_3 \times V_1, \quad (2.27)$$

and projecting (2.22) onto $V_3 \times V_1$, we arrive at a linear system of equations for the coefficients a_j.

The solution of the system is performed by means of a Petrov-Galerkin scheme, where the basis used in the expansion is different from the one used in the projection. The bases are composed of functions built on Chebyshev polynomials satisfying the boundary conditions. A detailed description of the method as well as the basis and functions used for the velocity field can be found in Meseguer & Marques (2000) and Meseguer *et al.* (2007), respectively. The basis functions for the temperature (last component of $\mathbf{X}_j$ in 2.27), and for the projection (with $\tilde{}$) are:

$$h_j(r) = (1 - y^2) T_{j-1}(y), \qquad \tilde{h}_j(r) = r^2 (1 - y^2) T_{j-1}(y), \quad (2.28)$$

where $y = 2(r - r_i) - 1$ and T_j are the Chebyshev polynomials. As a result of this process, we obtain a generalized eigenvalue system of the form

$$\lambda M_1 x = M_2 x, \quad (2.29)$$

where x is a vector containing the complex spectral coefficients(a_j) and the matrices M_1 and M_2 depend on the parameters of the problem, the axial wavenumber k and the azimuthal mode n. This system is solved by using *LAPACK*. The numerical code written to perform this work implements the described method and analyses a range of k, n and G provided by the user for a fixed Re number, searching for the critical values ($\Re\lambda = \lambda_r = 0$). The code has been tested by computing critical values for several cases in (McFadden *et al.*, 1984) and (Ali & Weidman, 1990), obtaining an excellent agreement with their results, as shown in table 2.4.3: the critical values computed coincide up to the last digit shown with those in the mentioned references. In both cases the outer cylinder is at rest ($\mathrm{Re}_o = 0$).

	Parameters			Critical values				
	η	σ	Ta	G_c	k_c	n_c	λ_i	$c = \lvert\lambda_i\rvert/k_c$
(a)	0.99	0.71	0	8038.0	2.80	0		0.25424
	0.60	0.71	0	8512.4	2.75	0		13.39899
	0.60	3.5	0	8347.5	2.75	0		12.97744
	0.99	3.5	0	7857.1	2.75	0		0.24673
(b)	0.6	4.35	2591.0	50.0	3.15	0	-0.50294	
	0.6	4.35	380.3	700.0	1.88	-3	18.66889	
	0.6	15	111.1	280.0	1.68	-2	6.58916	
	0.6	15	26.88	700.0	0.77	-4	7.19973	

Table 2.3: Code testing. The cases computed correspond to parameter values in (a) (McFadden *et al.*, 1984, table 1), and (b) Ali & Weidman (1990, table 1, pg 67). $Ta = 2(1-\eta)\mathrm{Re}_i/(1+\eta)$ is the Taylor number, $\lambda_i = \Im[\lambda]$ is the imaginary part of the critical eigenvalue, for which $\Re[\lambda] = 0$, and c is the dimensionless axial wave speed. The sign of n_c in our computation is opposite to that of (Ali & Weidman, 1990) because of the definition of the normal Fourier modes in (2.21).

2.5 Solver for three dimensional flow in a finite cylindrical cavity heated from below

For the simulations of rotating Rayleigh-Benard convection (finite rotating cylinder heated from below), we have used the code written by Mercader *et al.* (2010). The governing equations differ from (2.1) because they are formulated in a non-inertial reference frame and utilize a different non-dimensionalization. They read as

$$(\partial_t + \mathbf{v}\cdot\nabla)\mathbf{v} = -\nabla p + \sigma\nabla^2\mathbf{v} + Ra\sigma T\hat{\mathbf{e}}_\mathbf{z} + 2\sigma\Omega u\times\hat{\mathbf{e}_\mathbf{z}} - \frac{\sigma Fr Ra}{\Gamma}(1-z+T)r\hat{\mathbf{e}_\mathbf{r}}, \tag{2.30a}$$

$$(\partial_t + \mathbf{v}\cdot\nabla)T = w + \nabla^2 T, \tag{2.30b}$$

$$\nabla\cdot\mathbf{v} = 0, \tag{2.30c}$$

where $\mathbf{v} = (u, v, w)$ denotes the velocity field in cylindrical coordinates (r, θ, z), T is the deviation from the mean temperature T_c, p is the pressure and $\hat{\mathbf{e}}_\mathbf{z}$ and $\hat{\mathbf{e}}_\mathbf{r}$ are the unit vectors in axial and radial directions respectively. The Boussinesq approximation is used to deal with the small density variations stemming from changes in T. The equations are rendered dimensionless by using the height h as length scale, the vertical thermal diffusion time h^2/κ, where κ is the thermal diffusivity, as the time scale and the temperature difference between the top and bottom lids ΔT as the temperature scale.

Four dimensionless numbers arise:

$$\text{Rayleigh number} \qquad Ra = \alpha g \Delta T h^3 / \nu\kappa, \tag{2.31a}$$

$$\text{Froude number} \qquad Fr = \frac{\omega^2 R}{g}, \tag{2.31b}$$

$$\text{Coriolis number} \qquad \Omega = \frac{\omega h^2}{\nu}, \tag{2.31c}$$

$$\text{Prandtl number} \qquad \sigma = \nu/\kappa, \tag{2.31d}$$

where ω is the angular velocity of the system, R is the radius, g is the gravity acceleration and ν the kinematic viscosity.
The spatial and temporal discretizations as well as the the methodology used to solve the Helmholtz and Poisson equations are the same as those exposed in 2.2. A major difference between codes considering annular and pure cylindrical geometries is the presence of $r = 0$ in the domain. This poses a problem due to the singularity of the cylindrical coordinates at this point. This issue is addressed by forcing the proper parity of the Fourier expansions in the radial direction, so that clustering of collocations points near $r = 0$ is avoided (see Mercader *et al.*, 2010, for further details).

2.6 Continuation code for rotating waves in a finite cylindrical cavity heated from below

The unstable states of the flow , which play a relevant role in understanding the behavior of dynamical systems, can only be transiently captured when the governing equations are numerically integrated. Therefore, it is needed to implement additional techniques in order to compute them, such as Newton-like methods that allow us to iteratively solve a system of non-linear equations searching for steady states, no matter if they are stable or unstable.

The purpose of the code here described is to continue branches of unstable rotating waves, which are time dependent-flows precessing with a certain wave speed ω. That means that as a first step to apply Newton methods, the equations (2.30) must be formulated in a reference frame moving with the rotating wave so that these flow structures become steady. This is easily accomplished with a coordinate change $\hat{\theta} = \theta - \omega t$, such that any variable of the problem is expressed as $X(r, \theta, z, t) = X(r, \hat{\theta}, z)$. The resulting steady system of equations shows two differences with respect to that stemming from (2.30). There is an additional term as a consequence of the time derivative

$\partial_t X = -\omega \partial_{\hat{\theta}} X$. It does not pose any numerical challenge since it is treated explicitly together with the non-linear terms. Nevertheless, it introduces a new unknown ω, and thus a supplementary equation is required. The simplest choice is to fix the phase of the solution, which is performed by forcing the real or imaginary part of a certain Fourier mode for a single point in (r, z) to be zero.
Each iteration of the Newton method used to solve the steady non-linear system of equations obtained after the change of coordinates can be written as

$$(L + N_X)\delta X = (L + N)X \tag{2.32a}$$

$$X \leftarrow X - \delta X \tag{2.32b}$$

where X stands for any of the spatially discretized variables of the problem, L and N are respectively the spatially discretized linear and non-linear operators, N_X is the Jacobian of the non-linear term evaluated at X and δX is the correction to be applied on X.
Given a first -order semi-implicit time scheme such as

$$\frac{X^{i+1} - X^i}{\Delta t} = LX^{i+1} + NX^i = (I - \Delta t L^{-1})(L + N)X^i \tag{2.33}$$

where Δt is the time difference between the steps i and $i+1$ and I denotes the identity matrix. The linear system of equations (2.32a) can be solved using $P = (I - \Delta t L^{-1})$, with a sufficiently large value of ΔT, as a preconditioner

$$(I - \delta t L^{-1})(L + N_X)\Delta X = (I - \Delta t L^{-1})(L + N)X \tag{2.34}$$

The matrices $B = P(L + N)X$ and $A = P(L + N_X)$, on the right and left hand sides of (2.34), are straightforward to compute, since they correspond to one step evolution of (2.33) for the original and linearized systems respectively. The resolution of the system $AX = B$ is performed by using the *GMRES* library. Therefore, implementing the new methodology consists in a simple modification of the code described in section 2.5 to convert the second order time-stepper into a first order one, and include the *GMRES* subroutines needed to solve the resulting system. This method, which was first proposed by Mamun & Tuckerman (1995) and later implemented by Mercader *et al.* (2006), allows for efficiently solve (2.32a) since the computation and subsequent inversion of the Jacobian, which are very time consuming tasks, are avoided. Furthermore, the resulting system is well conditioned.
For the continuation of the solutions, a predictor-corrector method has been implemented. Given two previous solutions X_j and X_{j-1} the next state is guessed using the

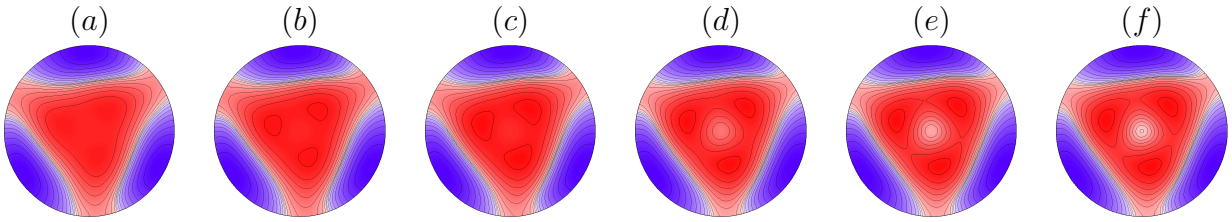

Figure 2.4: Smooth transition between the rotating wave patterns $C3$ and $D3$ obtained in Lopez & Marques (2009). This calculation has been used as a validation test of the new code. In all cases the deviation of the temperature T is shown in a horizontal section at mid-height for $Fr = 0.3$ and (a) $Ra = 10000$; (b) $Ra = 12500$; (c) $Ra = 13000$; (d) $Ra = 13500$; (e) $Ra = 14000$; (f) $Ra = 14500$.

secant prediction

$$\hat{X_{j+1}} = X_j + h_j v_j \tag{2.35a}$$

$$v_j = \frac{X_{j-1} - X_j}{\|X_{j-1} - X_j\|} \tag{2.35b}$$

where h_j is the step size of the continuation. The predicted state $\hat{X_{j+1}}$ is then used as initial condition for the Newton method above described, where it is corrected up to reach X_{j+1} within a specified accuracy. Nevertheless, a continuation method involves considering a control parameter as a dependent variable, in this case the Rayleigh Ra or Froude Fr numbers, and since a Newton method can only solve systems where the number of equations equals the number of unknowns, an extra condition has to be imposed to carry out this procedure. To this end we apply natural continuation, which consists in fixing the component of $\hat{X_{j+1}}$ that is changing faster, $\hat{X_{j+1_i}} = X_{j+1_i}$, where the index i is provided by the largest absolute value in v_j. Once X_{j+1} is obtained, the step size is varied depending on the iterations that have been required to converge, that is, if the solution converges in a few iterations h_j is increased, and conversely, h_j is decreased in the case of slow convergence. For further details on continuation methods we refer to Kuznetsov (1998). The Newton solver and continuation method have been validated by reproducing the solutions in Lopez & Marques (2009). One of these tests is illustrated in figure 2.4, showing the smooth transition between two rotating waves, termed as $C3$ and $D3$ in Lopez & Marques (2009), for $Fr = 0.3$ as Ra is varied. The same sequence can be found in the figure 5 of this reference.

CHAPTER 3

BIFURCATIONS WITH IMPERFECT $SO(2)$ SYMMETRY AND PINNING OF ROTATING WAVES

3.1 Introduction

Dynamical systems theory plays an important role in many areas of mathematics and physics because it provides the building blocks that allow us to understand the changes many physical systems experience in their dynamics when parameters are varied. These building blocks are the generic bifurcations (saddle-node, Hopf, etc.) that any arbitrary physical system experiences under parameter variation, regardless of the physical mechanisms underlying the dynamics. When one single parameter of the system under consideration is varied, codimension-one bifurcations are expected. If the system depends on more parameters, higher codimension bifurcations appear and they act as organizing centers of the dynamics.

The presence of symmetries changes the nature and type of bifurcations that a dynamical system may undergo. Symmetries play an important role in many idealized situations, where simplifying assumptions and the consideration of simple geometries result in dynamical systems equivariant under a certain symmetry group. Bifurcations with symmetry have been widely studied (Golubitsky & Schaeffer, 1985; Golubitsky *et al.*, 1988; Chossat & Iooss, 1994; Golubitsky & Stewart, 2002; Chossat & Lauterbach, 2000; Crawford & Knobloch, 1991). However, in any real system, the symmetries are only approximately fulfilled, and the breaking of the symmetries, due to the presence of noise, imperfections and/or other phenomena, is always present. There are numerous studies of how imperfect symmetries lead to dynamics that are unexpected in the symmetric problem (Keener, 1987; Campbell & Holmes, 1992; Knobloch *et al.*, 1995; Hirschberg & Knobloch, 1996; Dangelmayr *et al.*, 1997; Lamb & Wulff, 2000). However, a complete theory is currently unavailable. One observed consequence of imperfections in systems that support propagating waves is that the waves may become trapped by the imperfections (Keener, 1987; Westerburg & Busse, 2003; Thiele & Knobloch, 2006*a*,*b*). In these various examples, the propagation direction is typically biased. However, a more recent experiment has considered a case of a rotating wave pinned by symmetry-breaking imperfections for parameter values near where its sense of precession changes sign (Abshagen *et al.*, 2008).

When a system is invariant to rotations about an axis (invariance under the $SO(2)$ symmetry group), $SO(2)$-symmetry-breaking Hopf bifurcations result in rotating waves, consisting of a pattern that rotates about the symmetry axis at a given precession frequency without changing shape. This frequency is parameter dependent, and in many problems, when parameters are varied, the precession frequency changes sign along a curve in parameter space. What has been observed in different systems is that in the presence of imperfections, the curve of zero frequency becomes a band of finite width in parameter space. Within this band, the rotating wave becomes a steady solution. This is the so-called pinning phenomenon. It can be understood as the attachment of the rotating pattern to some stationary imperfection of the system, so that the pattern becomes steady, as long as its frequency is small enough so that the imperfection is able to stop the rotation. This pinning phenomenon bears some resemblance to the frequency locking phenomena, although in the frequency locking case we are dealing with a system with two non-zero frequencies and their ratio becomes constant in a region of parameter space (a resonance horn), whereas here we are dealing with a single frequency crossing zero.

In the present chapter we analyze the breaking of $SO(2)$ symmetry in a dynamical system close to a Hopf bifurcation whose frequency changes sign along a curve in parameter space. The analysis shows that breaking $SO(2)$ symmetry is much more complex than expected, resulting in a bifurcation of high codimension (about nine). Although it is not possible to analyze in detail such a complex and high-codimension bifurcation, we present here the analysis of a specific case in which the $SO(2)$ symmetry is broken by adding a ϵ term to the normal form. We find that a band of pinned solutions appears around the zero frequency curve of the symmetric case, and that this band is delimited by curves of infinite-period bifurcations. A complicated dynamics with several codimension-two bifurcations occurring in a small region of parameter space is found in the junction between the infinite-period bifurcation curves and the Hopf bifurcation curve. We also present a fluid dynamics example of pinning owing to the $SO(2)$ symmetry breaking in a rotating cylinder subject to vertical convection. This is a particularly interesting case, because the symmetry breaking occurs at a subcritical Hopf bifurcation, unlike previously reported pinning phenomena in Taylor Couette flows (Pacheco *et al.*, 2011; Abshagen *et al.*, 2008), which always occurred at supercritical bifurcations.

The chapter is organized as follows. In section 3.2 the properties of a Hopf bifurcation with $SO(2)$ symmetry with the precession frequency crossing through zero are summarized, and the general unfolding of the $SO(2)$ symmetry breaking process is discussed. The next section, 3.3, explores the particulars of breaking the symmetry at order zero.

The pinning of rotating waves in a rotating convective cylinder given in section 3.4 illustrates the application of the general theory to a real problem in fluid dynamics. The governing equations and methodology used to deal with the problem are introduced in 3.4.1, in 3.4.2, the bifurcation scenario is briefly described, and finally, 3.4.3 provides evidences of the infinite period bifurcation taking place as a consequence of the $SO(2)$ symmetry breaking. Conclusions and perspectives are presented in 3.5.

3.2 Hopf bifurcation with $SO(2)$ symmetry and zero frequency

The normal form for a Hopf bifurcation is

$$\dot{z} = z(\mu + i\omega - c|z|^2), \tag{3.1}$$

where z is the complex amplitude of the bifurcating periodic solution, μ is the bifurcation parameter, and ω and c are functions of μ and generically at the bifurcation point ($\mu = 0$) both are different from zero. It is the non-zero character of ω that allows one to eliminate the quadratic terms in z in the normal form. This is because the normal form $\dot{z} = P(z, \bar{z})$ satisfies (e.g., see Haragus & Iooss, 2011)

$$P(\mathrm{e}^{-\mathrm{i}\omega t}z, \mathrm{e}^{\mathrm{i}\omega t}\bar{z}) = \mathrm{e}^{-\mathrm{i}\omega t}P(z, \bar{z}), \tag{3.2}$$

where P is a low order polynomial that captures the dynamics in a neighborhood of the bifurcation point. If $\omega = 0$, this equation becomes an identity and P cannot be simplified. The case $\omega = 0$ is a complicated bifurcation and it depends on the details of the double-zero eigenvalue of the linear part L of P; as $z = x + \mathrm{i}y$ is complex, the matrix of L using the real coordinates (x, y) is a real 2×2 matrix. If L is not completely degenerate, that is

$$L = \begin{pmatrix} 0 & 1 \\ 0 & 0 \end{pmatrix}, \tag{3.3}$$

then we have the well-studied Takens–Bogdanov bifurcation, whereas the completely degenerate case,

$$L = \begin{pmatrix} 0 & 0 \\ 0 & 0 \end{pmatrix}, \tag{3.4}$$

is a high-codimension bifurcation that has not been completely analyzed.

If the system has $SO(2)$ symmetry, it must also satisfy

$$P(\mathrm{e}^{\mathrm{i}m\theta}z, \mathrm{e}^{-\mathrm{i}m\theta}\bar{z}) = \mathrm{e}^{\mathrm{i}m\theta}P(z, \bar{z}), \tag{3.5}$$

where Z_m is the discrete symmetry retained by the bifurcated solution. When the group Z_m is generated by rotations of angle $2\pi/m$ about an axis of m-fold symmetry, as is usually the case with $SO(2)$, then the group is also called C_m. Equations (3.2) and (3.5) are completely equivalent and have the same implications for the normal form structure. Advancing in time is the same as rotating the solution by a certain angle ($\omega t = m\theta$); the bifurcated solution is a rotating wave. Therefore, if ω becomes zero by varying a second parameter, we still have the same normal form (3.1), due to (3.5), with ω replaced by a small parameter ν:

$$\dot{z} = z(\mu + i\nu - c|z|^2). \tag{3.6}$$

The Hopf bifurcation with $SO(2)$ symmetry and zero frequency is, in this sense, trivial. Introducing the modulus and phase of the complex amplitude $z = re^{i\phi}$, the normal form becomes

$$\begin{aligned} \dot{r} &= r(\mu - ar^2), \\ \dot{\phi} &= \nu - br^2, \end{aligned} \tag{3.7}$$

where $c = a + ib$, and let us assume for the moment that a and b are positive. The bifurcation frequency in (3.7) is now the small parameter ν. The bifurcated solution RW_m exists only for $\mu > 0$, and has amplitude $r = \sqrt{\mu/a}$ and frequency $\omega = \nu - b\mu/a$. The limit cycle RW_m becomes an invariant set of steady solutions along the straight line $\mu = a\nu/b$ (labeled L in figure 3.1) where the frequency of RW_m goes to zero; the angle between L and the Hopf bifurcation curve (the horizontal axis $\mu = 0$) is α_0. The bifurcation diagram and a schematic of the bifurcations along a one-dimensional path is also shown in figure 3.1. The bifurcation point $\mu = \nu = 0$, labeled ZF (zero-frequency Hopf point) in figure 3.1(a), is a codimension-two bifurcation. It coincides with the generic Hopf bifurcation, except that it includes a line L along which the bifurcated solution has zero frequency.

Assuming $c \neq 0$, we can simplify (3.7) by scaling z so that $|c| = 1$; we will write

$$c = a + ib = ie^{-i\alpha_0} = \sin\alpha_0 + i\cos\alpha_0, \quad b + ia = e^{i\alpha_0}, \tag{3.8}$$

which helps simplify subsequent expressions. The case a and b both positive, which we consider in our theoretical approach, corresponds to the fluid dynamics problems that motivated the present analysis (Abshagen *et al.*, 2008; Pacheco *et al.*, 2011).

For other signs of a and b, analogous conclusions can be drawn. It is of particular interest to consider the subcritical case $a < 0$ as it corresponds to the fluid dynamics problem illustrated in section 3.4. By reversing time and changing the sign of μ and ν, we obtain

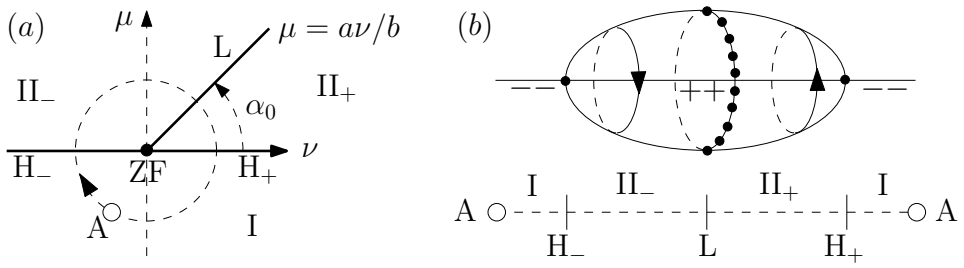

Figure 3.1: Hopf bifurcation with $SO(2)$ symmetry and zero frequency; part (a) shows the bifurcation diagram, where the thick lines are bifurcation curves, and part (b) shows the bifurcations along the path A shown in (a). The fixed point curve is labeled with the signs of its eigenvalues. In regions II_- and II_+ the limit cycles, born at the Hopf bifurcations H_- and H_+, rotate in opposite senses. L is the line where the limit cycle becomes an invariant curve of fixed points.

exactly the same normal form (3.7) but with the opposite sign of a and b. By changing the sign of ϕ and ν, we obtain (3.7) with the opposite sign of b. Therefore, all possible cases corresponding to different signs of a and b can be reduced to the case where a and b are both positive.

3.2.1 Unfolding the Hopf bifurcation with zero frequency

If the $SO(2)$ symmetry in the normal form (3.6) is completely broken, and no symmetry remains, then the restrictions imposed on the normal form by (3.5) disappear completely and all the terms in z and $\bar{z}$ missing from (3.6) will reappear multiplied by small parameters. This means that the normal form will be

$$\dot{z} = z(\mu + i\nu - c|z|^2) + \epsilon_1 + \epsilon_2\bar{z} + \epsilon_3\bar{z}^2 + \epsilon_4 z\bar{z} + \epsilon_5 z^2, \tag{3.9}$$

where additional cubic terms have been neglected because we assume $c \neq 0$ and that $cz|z|^2$ will be dominant. As the ϵ_i are complex, we have a problem with 12 parameters. Additional simplifications can be made in order to obtain the so-called hypernormal form; this method is extensively used by Kuznetsov (2004), for example. Unfortunately, many of the simplifications rely on having some low-order term in the normal form being non-zero with a coefficient of order one. For example, if $\omega \neq 0$, it is possible to make c real by using a time re-parametrization. In our problem, all terms up to and including second order are zero or have a small coefficient, and so only a few simplifications are possible. These simplifications are an infinitesimal translation of z (two parameters), and an arbitrary shift in the phase of z (one parameter). Using these transformations

the twelve parameters can be reduced to nine. In particular, one of either ϵ_4 or ϵ_5 can be taken as zero and the other can be made real. By rescaling z, we can make c of modulus one, as in (3.8). A complete analysis of a normal form depending on nine parameters, i.e. a bifurcation of codimension of about nine, is completely beyond the scope of the present study. In the literature, only codimension-one bifurcations have been completely analyzed. Most of the codimension-two bifurcations for ODE and maps have also been analyzed, except for a few bifurcations for maps that remain outstanding (Kuznetsov, 2004). A few codimension-three and very few codimension-four bifurcations have also been analyzed (Chow *et al.*, 1994; Dumortier *et al.*, 1997), but to our knowledge, there is no systematic analysis of bifurcations of codimension greater than two. Therefore, the only way we can address this analysis is by considering the five cases, ϵ_1 to ϵ_5, separately. In the following section, we describe in detail the case in which the SO(2) symmetry is broken with a ϵ_1 parameter, which provides the theoretical background for the dynamics illustrated in 3.4. A comprehensive study of the remaining cases can be found in Marques *et al.* (2013, 2012).

Before going into detail with the ϵ_1 case, some general comments can be made about the five cases, which are of the form

$$\dot{z} = z(\mu + i\nu - c|z|^2) + \epsilon z^q \bar{z}^{p-q}, \tag{3.10}$$

for integers $0 \leq q \leq p \leq 2$, excluding the case $p = q = 1$ which is $SO(2)$ equivariant and so ϵ can be absorbed into μ and ν. By changing the origin of the phase of z, we can modify the phase of ϵ so that it becomes real and positive. Then, by re-scaling z, time t, and the parameters μ and ν as

$$(z, t, \mu, \nu) \to (\epsilon^\delta z, \epsilon^{-2\delta} t, \epsilon^{2\delta}\mu, \epsilon^{2\delta}\nu), \quad \delta = \frac{1}{3-p}, \tag{3.11}$$

we obtain (3.10) with $\epsilon = 1$, effectively leading to codimension-two bifurcations in each of the five cases. We expect complex behavior for $\mu^2 + \nu^2 \lesssim \epsilon^2$, when the three parameters are of comparable size, while the effects of small imperfections breaking $SO(2)$ will correspond to $\mu^2 + \nu^2 \gg \epsilon^2$. From now on $\epsilon = 1$ will be assumed, and we can restore the explicit ϵ-dependence by reversing the transformation (3.11).

The normal forms corresponding to the ϵ_1, ϵ_2 and ϵ_3 cases have already been analyzed in contexts completely different to the $SO(2)$ symmetry-breaking context considered here. The context in which these problems were studied stems from low-order resonances in perturbed Hopf problems. Gambaudo (1985) studied time-periodic forcing near a Hopf bifurcation point, analyzing the problem using the Poincaré stroboscopic map. The normal forms corresponding to the 1:1, 1:2 and 1:3 strong resonances coincide with the

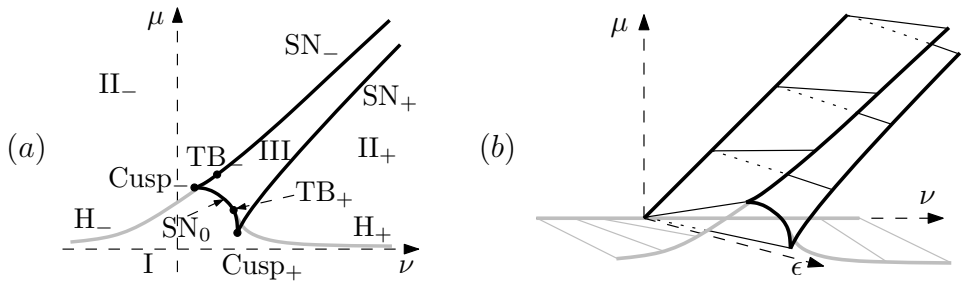

Figure 3.2: (a) Bifurcations of the fixed points corresponding to the normal form (3.12), and (b) is a perspective view of the corresponding codimension-three bifurcation in terms of (μ, ν, ϵ). See table 3.1 for a glossary.

normal form for cases with only the ϵ_1, ϵ_2 and ϵ_3 terms retained in (3.9), respectively. Later, motivated by a problem of a nonlinear oscillator with damping and quasi-periodic driving, a series of papers extended the strong resonances results of Gambaudo (1985) by studying the semi-global bifurcations for periodically and quasi-periodically perturbed driven damped oscillators near a Hopf bifurcation (see Wagener, 2001; Broer *et al.*, 2008; Saleh & Wagener, 2010, and references therein). Nevertheless, the analysis has focused on the regions where μ, ν and ϵ are of comparable size; here we will also consider what happens for $\mu^2 + \nu^2 \gg \epsilon^2$ which is particularly important for the pinning phenomenon.

3.3 Symmetry breaking of $SO(2)$ with an ϵ term

The normal form in this case is (3.10) with $p = q = 0$ and $\epsilon = 1$:

$$\dot{z} = z(\mu + i\nu - c|z|^2) + 1\,. \tag{3.12}$$

The fixed points of (3.12) are given by a cubic equation. The parameter space is divided into two regions, region III has three fixed points and the rest of parameter space has one fixed point, separated by a saddle-node curve shown in figure 3.2(a) as a thick black line. The saddle-node curve is divided into three different arcs $\mathrm{SN}_\pm$ and SN_0 by two codimension-two cusp bifurcation points, $\mathrm{Cusp}_\pm$. The fixed points also undergo Hopf bifurcations along the curves $\mathrm{H}_\pm$ shown in grey in figure 3.2(a). Figure 3.2(b) shows what happens when the ϵ dependence is restored; what we have is that figure 3.2(a) just scales with ϵ as indicated in (3.11), and the pinning region collapses onto the line L of the perfect case with $SO(2)$ symmetry. For $|\nu| \to \infty$, the Hopf curves $\mathrm{H}_\pm$ are asymptotic to the $\mu = 0$ axis, the Hopf curve for $\epsilon = 0$. The other ends of the $\mathrm{H}_\pm$ curves are the Takens–Bogdanov points $\mathrm{TB}_\pm$ on the saddle-node curve. The TB_- and Cusp_- codimension-two bifurcation points are very close to each other. For clarity in

Table 3.1: Glossary of bifurcations.

Codimension-one bifurcations	
$SN_{\pm,0}$	Saddle-node (also called fold) bifurcations
$H_{\pm,0}$	Hopf bifurcations
$PF_{\pm}$	Pitchfork bifurcations
CF	Cyclic fold: two limit cycles are born simultaneously
L, $L_{l,u}$	Limit cycle becoming a family of fixed points
$Hom_{\pm,0}$, Hom	Homoclinic collision of a limit cycle with a saddle
$Het_{\pm,0}$	Heteroclinic collision of a limit cycle with saddles
$SNIC_{\pm,0}$	Saddle-node appearing on a limit cycle
Glu	Gluing bifurcation – two limit cycles collide with a saddle
Codimension-two bifurcations	
$Cusp_{\pm}$	Cusp bifurcations
$TB_{\pm}$, TB	Takens–Bogdanov bifurcations
$dPF_{\pm}$	Degenerate pitchfork – zero cubic term
Ba	Bautin bifurcation – degenerate Hopf with zero cubic term
PfGl	Simultaneous gluing Gl and pitchfork PF bifurcations
CfHom	Simultaneous cyclic-fold CF and homoclinic collision Hom
$CfHet_{\pm}$	Simultaneous cyclic-fold CF and heteroclinic collision Hom
$SnicHom_{\pm,0}$	Simultaneous SNIC and homoclinic collision
$SnicHet_{\pm,0}$	Simultaneous SNIC and heteroclinic collision

the schematics shown in figures 3.2(a) and 3.3, we have exaggerated their separation. In region I there is a single stable fixed point. It loses stability along the Hopf curves $H_{\pm}$, so in regions $II_{\pm}$ there exist an unstable fixed point and a stable rotating wave; the rotating waves in $II_{\pm}$ rotate in opposite directions, and III is the pinning region where the rotation stops and we have a stable fixed point. Solutions with $\omega = 0$, that existed only along a single line in the absence of imperfections, now exist in a region of finite width.

From the Takens–Bogdanov points, dynamical systems theory says that two curves of homoclinic bifurcations emerge, resulting in global bifurcations around these points. Moreover, the stable limit cycles in regions $II_{\pm}$ do not exist in region III, so they must disappear in additional bifurcations. Figure 3.3 summarizes all the bifurcation curves that appear in the present case. There are nine codimension-two points organizing the dynamics of the normal form (3.12), and most of the bifurcation curves correspond to global bifurcations of limit cycles; they are described in detail in Marques *et al.* (2012).

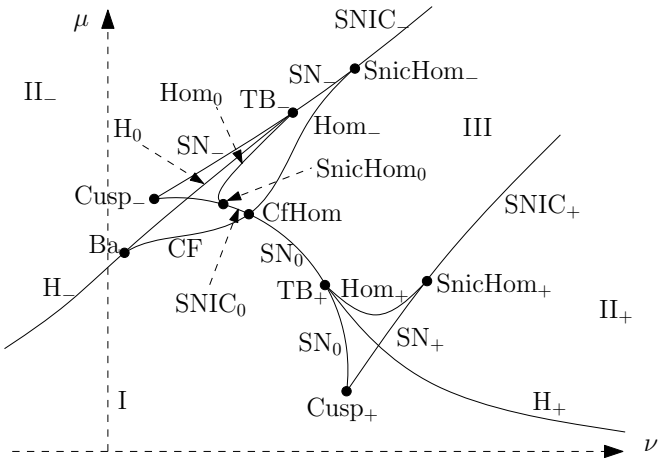

Figure 3.3: Schematic of the bifurcations of the normal form (3.12). There are seven curves of global bifurcations, $\mathrm{Hom}_{\pm}$, Hom_0 (homoclinic collisions of a limit cycle with a saddle), CF (a cyclic-fold), $\mathrm{SNIC}_{\pm}$ and SNIC_0, and nine codimension-two points (black circles). The regions around the codimension-two points have been enhanced for clarity. See table 3.1 for a glossary.

For large values of $\mu^2 + \nu^2$ the stable limit cycles in regions $\mathrm{II}_{\pm}$ disappear at $\mathrm{SNIC}_{\pm}$ (saddle-node on an invariant circle) bifurcation curves. On these curves, a saddle-node bifurcation of fixed points takes place on top of the limit cycle, and the cycle disappears in an infinite-period bifurcation. What remains, and is observable, is the stable fixed point born at the saddle-node.

The width w of the pinning region at a distance $d = \sqrt{\mu^2 + \nu^2}$ from the origin is measured transversally to the straight line L. In the case considered here, it is given by $w = 2/\sqrt{d}$. Restoring the ϵ-dependence, we obtain $w(d, \epsilon) = 2\epsilon/\sqrt{d}$. The pinning region becomes narrower with increasing distance from the bifurcation point, and its width is proportional to ϵ, the magnitude of the imperfection (see figure 3.2*b*).

Further details relating to the calculation of the fixed points and bifurcation curves can be found in Marques *et al.* (2012).

3.4 Pinning of rotating waves in rotating Rayleigh-Bénard convection

Up to now, we have considered the zero-frequency Hopf problem in the context of a supercritical Hopf bifurcation. However, in some pinning regions reported in fluid dynamics problems, such as Taylor–Couette flow (Pacheco *et al.*, 2011), the zero frequency

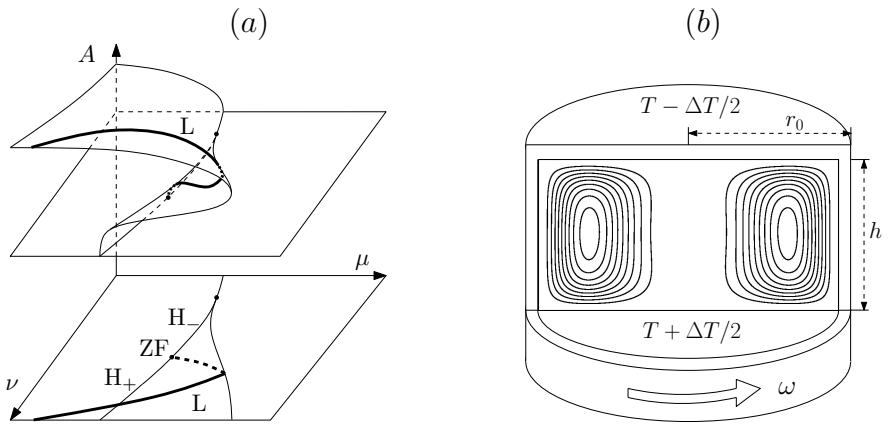

Figure 3.4: (a) Schematic of the Bautin bifurcation, including the path L of frequency zero bifurcated states in the $SO(2)$ perfect system, shown in a two parameter space (μ, ν) with A a global measure of the solution. Also shown is the projection of the saddle-node surface on parameter space. (b) Schematic of the rotating convection apparatus, with the streamlines of the basic state shown in the inset

occurs quite close to a Bautin bifurcation, at which the Hopf bifurcation switches from being supercritical to subcritical, and a natural question is what are the consequences of the zero-frequency occurring on a subcritical Hopf bifurcation. The normal form theory for the behavior local to the Hopf bifurcation carries over by changing the direction of time and the sign of the parameters μ and ν as discussed before, but then both the limit cycle and the pinned state are unstable and not observable in a physical experiment or direct numerical simulation. The limit cycle becomes observable as it undergoes a saddle-node of limit cycles (a cyclic fold) bifurcation at the fold associated with the Bautin bifurcation (see figure 3.4 a), and we expect that the pinned state does likewise with a saddle-node of fixed points bifurcation along the same fold. We have identified a rotating convection problem where precisely this occurs (Marques *et al.*, 2007; Lopez & Marques, 2009), and conducted numerical simulations by introducing a $SO(2)$ symmetry-breaking bifurcation that produces a pinning region on the upper branch of the subcritical Hopf bifurcation.

3.4.1 Governing equations and work methodology

The rotating convection problem consists of a fluid-filled cylinder of radius r_0 and height h, rotating at a constant rate ω rad/s. The cold top and hot bottom endwalls are maintained at constant temperatures $T_0 \mp 0.5\Delta T$, where T_0 is the mean temperature and ΔT is the temperature difference between the end walls. The sidewall has zero heat

flux. Figure 3.4 *b* shows a schematic of the flow configuration.

Using the Boussinesq approximation that all fluid properties are constant except for the density in the gravitational and centrifugal buoyancy terms, and using h as the length scale, h^2/κ as the time scale, and ΔT as the temperature scale, the governing equations written in the rotating frame of reference are:

$$(\partial_t + \boldsymbol{u}\cdot\nabla)\boldsymbol{u} = -\nabla p + \sigma\nabla^2\boldsymbol{u} + \sigma Ra\Theta\hat{z} + 2\sigma\Omega\boldsymbol{u}\times\hat{z} - \frac{\sigma FrRa}{\Gamma}(\Theta - z)\boldsymbol{r}, \quad (3.13)$$

$$(\partial_t + \boldsymbol{u}\cdot\nabla)\Theta = w + \nabla^2\Theta, \qquad \nabla\cdot\boldsymbol{u} = 0\,, \quad (3.14)$$

where $\boldsymbol{u} = (u, v, w)$ is the velocity field in cylindrical coordinates (r, θ, z), p is the kinematic pressure (including gravitational and centrifugal contributions), $\hat{z}$ the unit vector in the vertical direction z, and $\boldsymbol{r}$ is the radial vector in cylindrical coordinates. Instead of the non-dimensional temperature T, we have used the temperature deviation Θ with respect to the conductive profile, $T = T_0/\Delta T - z + \Theta$, as is customary in many thermal convection studies.

There exist five dimensionless parameters: the Rayleigh number, $Ra = \alpha g h^3\Delta T/(\kappa\nu)$, the Froude number $Fr = \omega^2 r_0/g$, the Coriolis number, $\Omega = \omega h^2/\nu$, the Prandtl number, $\sigma = \nu/\kappa$, and the aspect ratio, $\Gamma = r_0/h$, where α is the coefficient of volume expansion, g is the gravitational acceleration, κ is the thermal diffusivity, and ν is the kinematic viscosity. The control parameters are Ra and Fr so that flow states are determined by the competition between gravitational and centrifugal buoyancy. The remaining parameters have been fixed: $\Gamma = 1$, in order to prevent from very high azimuthal wavenumber modes m, $\sigma = 7.0$, which corresponds to water near room temperature and $\Omega = 100$. Note that Ω depends on ω, and thus it should vary as Fr changes. Nevertheless, we keep it fixed in order to reduce the complexity of the problem. For any $Fr \neq 0$, the system is not invariant to the so-called Boussinesq symmetry corresponding to invariance to a reflection K_z about the half-height $z = 0$. The system is only invariant under rotations about the axis of the cylinder, the $SO(2)$ symmetry.

The governing equations have been advanced in time using the code described in 2.5. We have used $n_r = 36$, $n_\theta = 40$ and $n_z = 64$ spectral modes in r, θ and z and a time-step $dt = 2\times10^{-5}$ thermal time units in all computations. We have checked the spectral convergence of the code using the infinity norm of the spectral coefficients of the computed solutions. The trailing coefficients of the spectral expansions are at least five orders of magnitude smaller than the leading coefficients. In order to compute the zero-frequency line L in the subcritical region of the Bautin bifurcation, where the fixed points and limit cycles involved are unstable, we have used the continuation code

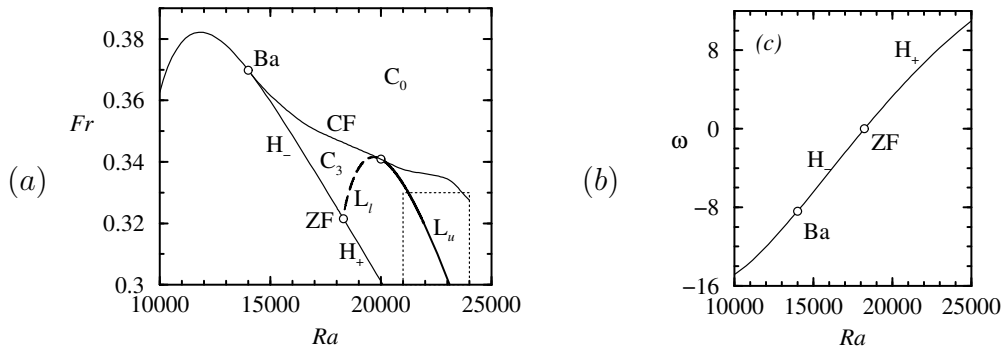

Figure 3.5: (a) Bifurcation curves for $\Omega = 100$, $\sigma = 7$ and $\Gamma = 1$, where $\mathrm{H}_{\mp}$ are the segments of the Hopf bifurcation with negative and positive frequency, the Bautin point Ba is where the Hopf bifurcation switches from super- to subcritical and the cyclic-fold bifurcation curve CF emerges. The lines L_l and L_u are the loci where the rotating wave(C_3) has zero frequency on the lower and upper branches of the cyclic fold. The rectangle around L_u corresponds to figure 3.7a. The base flow is denoted as C_0. (b) The frequency along the Hopf bifurcation $\mathrm{H}_{\mp}$ with the Bautin point and the point ZF, where the sense of precession changes, marked as open symbols.

outlined in 2.6.

3.4.2 Bifurcation scenario

Figure 3.5(a) shows the parameter region of interest in this convection problem. In the region of high Froude number we have a stable steady solution C_0, consisting of a single axisymmetric convective roll where the warm fluid moves upwards close to the axis (due to the rotation of the container), and returns along the sidewall. The figure 3.6 shows the temperature profile of C_0 at $Ra = 2 \times 10^4$ and $Fr = 0.38$, plotted in a meridional plane and in a horizontal section at mid-height. It is clearly illustrated that C_0 is $SO(2)$-equivariant with respect to rotations about the cylinder axis. The cool (heavier) fluid at the top is centrifuged radially outward, whereas the hot (lighter) fluid at the bottom is centrifuged radially inward, forming an upwelling plume near the axis. This base state loses stability when the Froude number Fr decreases, in a Hopf bifurcation along the curves $\mathrm{H}_{\pm}$. The bifurcation is supercritical for $Ra < 14\,157$ and subcritical for higher Ra. Contours of the temperature of the new state C_3 are illustrated in figure 3.8 (a), plotted in a horizontal section at mid-height. The change from supercritical to subcritical happens at the codimension-two Bautin bifurcation point Ba, at $(Ra, Fr) \approx (14\,157, 0.3684)$. The bifurcated limit cycle, a rotating wave with azimuthal wave number $m = 3$, is unstable, but becomes stable at the cyclic fold curve CF (a saddle-node bifurcation of limit cycles). This curve CF originates at the Bautin point Ba. There are other flow

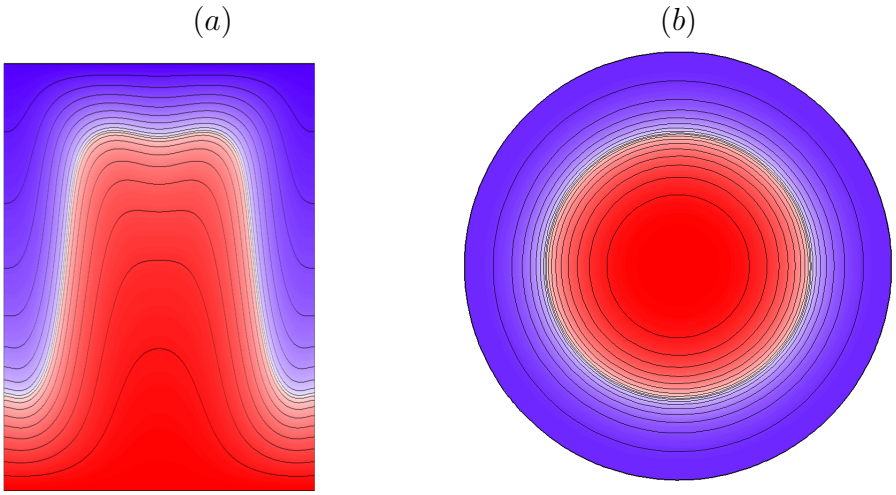

Figure 3.6: Contours of the temperature for the base state at $Ra = 2\times10^4$ and $Fr = 0.38$ in (a) Meridional section and (b) Horizontal section at mid-height.

states that are stable in this same region (Lopez & Marques, 2009); these additional states are well separated in phase space and the numerics we describe below are focused on the base state and the $m = 3$ bifurcated rotating wave.

Figure 3.5(b) shows the computed frequency of the limit cycle along the Hopf bifurcation curve. This frequency is negative along H_- and positive along H_+, and is zero at the ZF (zero frequency) point. At this point we have precisely the scenario discussed in the present chapter: a flow (the base state) with $SO(2)$ symmetry undergoing a Hopf bifurcation that has zero frequency at that point. Figure 3.5(a) also includes the line L where the frequency of the bifurcated states is zero. This curve has been computed using continuation methods since the zero-frequency state is unstable in the lower part (L_l) of the saddle-node CF, and therefore cannot be obtained via time evolution. The zero frequency state becomes stable upon crossing the saddle-node curve CF and moving to the upper part L_u of the saddle-node CF, and becomes observable both experimentally and by numerical simulations advancing the Navier-Stokes equations in time.

3.4.3 Pinned solutions and infinite period bifurcation curves

In order to break the $SO(2)$ symmetry and see if a pinning region appears, an imperfection has been introduced, in the form of an imposed linear profile of temperature at the top lid, $\Theta(r, \theta, z = 0.5) = \epsilon\, r \cos\theta$, where ϵ is a measure of the symmetry breaking. This term completely breaks the rotational symmetry of the governing equations, and no symmetry remains. Figure 3.7(a) shows that the line L becomes a band of pinned

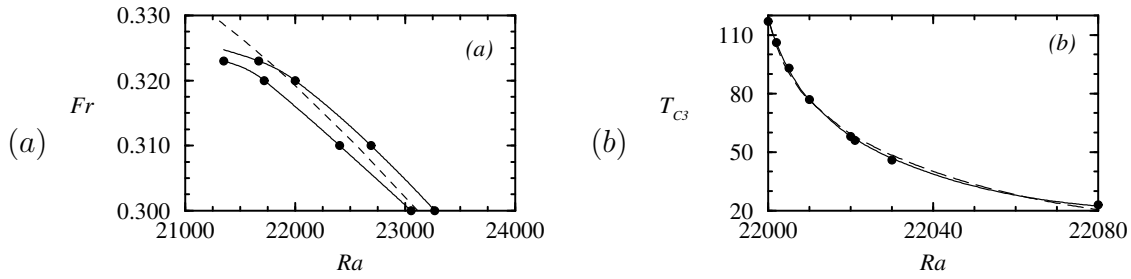

Figure 3.7: (a) SNIC bifurcation curves in (Ra, Fr) space bounding the pinning region for $\Omega = 100$, $\sigma = 7$ and $\Gamma = 1$. The region shown is the rectangle in figure 3.5a, and the dashed line is the L_u curve in the perfect case. (b) The period of the rotating wave C3(black filled circles) as it approaches the SNIC bifurcations at $Fr = 0.32$ and other parameters as in (a). Solid and long dashed line represent square root and logarithmic fits respectively, corresponding to the scaling laws of SNIC and homoclinic bifurcations.

solutions, steady solutions with frequency zero, as predicted by the normal form theory presented in 3.3. We can also check the nature of the bifurcation taking place at the boundary of the pinning region. Figure 3.7(b) shows the variation of the period of the limit cycle approaching the pinning region. The period substantially increases as Ra comes close to the bifurcation, which points to the existence of an infinite period bifurcation. In a system like the one we are presenting here, where a limit cycle bifurcates into three steady states, two types of infinite period bifurcations become possible. The first type of bifurcation is a SNIC (saddle node on invariant circle) that occurs when a saddle node emerges on the limit cycle. The second type corresponds to a homoclinic bifurcation in which the stable limit cycle merges with a saddle node. The scaling laws for the period of a limit cycle approaching either a homoclinic or a SNIC bifurcation are

$$T_{\mathrm{Het}} = \frac{1}{\lambda} \ln \frac{1}{\mu - \mu_c} + O(1), \quad T_{\mathrm{SNIC}} = \frac{k}{\sqrt{\mu - \mu_c}} + O(1), \tag{3.15}$$

where λ is the positive eigenvalue of the saddle and k is a constant. In order to distinguish between these two bifurcations, the computed periods have been fitted with 3.15. The square root fit (solid line in figure 3.7 (b)) works better than the logarithmic fit (long dashed line in figure 3.7 (b)), so we estimate that the bifurcation is a SNIC bifurcation, as the normal form theory presented predicts it should be sufficiently far from the zero frequency point ZF.

Figure 3.8 shows snapshots of isotherms at mid-height ($z = 0$) with $Ra = 21950$ and $Fr = 0.32$, which is a parameter point inside the pinning region (see figure 3.7a). Part (a) shows solution in the symmetric system ($\epsilon = 0$) and (b) is the pinned solution with an imperfection of $\epsilon = 0.05$, corresponding to a maximum variation of temperature of $5\%\Delta T$ at the top lid. The steady pinned solution has broken the $SO(2)$ symmetry;

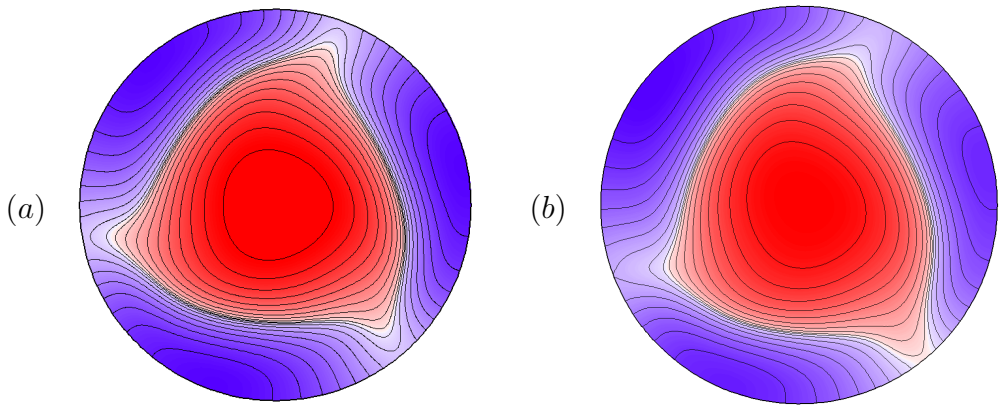

Figure 3.8: Temperature contours at mid height ($z = 0$) for $\Omega = 100$, $\sigma = 7$, $\Gamma = 1$, $Ra = 21950$ and $Fr = 0.32$. (a) is the symmetric solution without imperfection ($\epsilon = 0$), and (b) is a pinned solution with an imperfection $\epsilon = 0.05$. There are 20 quadratically spaced contours in the interval $T \in [-0.31, 0.31]$, with blue (red) for the cold (warm) fluid.

one of the three arms of the solution is closer to the wall than the other two. The attachment of the solution to the sidewall, due to the imperfection at the top lid, results in the pinning phenomenon.

3.5 Summary and conclusions

The aim of this chapter has been to provide a general dynamical systems description of the pinning phenomenon which is observed in systems possessing two ingredients: slowly traveling or rotating waves and imperfections. The description boils down to the unfolding of a Hopf bifurcation in an $SO(2)$ equivariant system about the point where the Hopf frequency is zero. We have identified some interesting facts. These are that the curve of zero frequency splits into a region in parameter space of finite width that scales with the strength of the imperfection, and this region is delimited by SNIC bifurcations. In the very small neighborhood of the zero frequency Hopf bifurcation point, where the SNIC curves and the Hopf curve approach each other, the dynamics is extremely complicated, consisting in a multitude of codimension-two local bifurcations and global bifurcations. We provide an example in rotating Rayleigh-Bénard convection to illustrate both the pinning phenomenon and the use of the theory to describe it. Unlike previously reported pinning areas in other canonical fluid dynamics problems, the Hopf bifurcation which gives rise to the rotating waves is subcritical. Nevertheless, this fact does not modify the theoretical prediction, and a pinning region is found when

the $SO(2)$ invariance is broken and rotating waves are precessing with a frequency near zero.

CHAPTER 4

THE BOUSSINESQ APPROXIMATION IN RAPIDLY ROTATING FLOWS

4.1 Introduction

In 1903 Boussinesq observed that: "The variations of density can be ignored except where they are multiplied by the acceleration of gravity in the equation of motion for the vertical component of the velocity vector" (Boussinesq, 1903). This simple approximation has had a far-reaching impact on many areas of fluid dynamics; it allows us to approximate flows with small density variations as incompressible, whilst retaining the leading order effects due to the density variations. Moreover, it is of great importance both analytically and numerically as it eliminates acoustic modes, which are challenging to treat. Many problems in fluid dynamics have been tackled with Boussinesq-type approximations, rendering in most cases successful results in good agreement with experiments. However, some problems feature important physics neglected in the original Boussinesq approximation. For example, in many investigations of systems subject to rotation, the centrifugal term in the Navier-Stokes equations is treated as a gradient and is absorbed into the pressure (Chandrasekhar, 1961). Under this assumption centrifugal buoyancy enters the hydrostatic balance but does not play a dynamic role, making an analytical treatment of the equations possible. In contrast, the inclusion of centrifugal terms in numerical simulations requires a minimal coding and computing effort. Therefore, it should always be included in the simulations (Randriamampianina *et al.*, 2006), and whether it is dynamically significant or not should be determined a posteriori.

In systems rotating at angular velocity Ω the dynamical role of centrifugal buoyancy is straightforward to model. Typically, a term acting in the radial direction and proportional to $\rho'\Omega^2$, where ρ' is the density variation, is added to the Navier-Stokes equation (Barcilon & Pedlosky, 1967; Homsy & Hudson, 1969). One example where this term has been included is rotating Rayleigh-Bénard convection. Hart (2000) studied the effect of centrifugal buoyancy using a self-similar and perturbative approach, confirmed by numerical simulations in the axisymmetric case (Brummell *et al.*, 2000). More recently, Marques *et al.* (2007); Lopez & Marques (2009) conducted full 3D simulations in the same geometry. All these investigations show the relevance of centrifugal buoyancy in rotating convection. In these studies the imposed temperature gradient is parallel to gravity, while in the present work both gradients are perpendicular, and additional centrifugal effects, besides the traditional $\rho'\Omega^2$ term, are also included.

Note that in the traditional approach, described in the previous paragraph, effects due to differential rotation or strong internal vorticity, of especial importance in rapidly rotating flows, are neglected. The increasing interest in these flows because of their industrial (e.g. cyclonic dust collectors or vortex chambers) and scientific (astrophysical and atmospheric turbulence) applications (see Elperin *et al.*, 1998) motivates the development of a new approximation, which we here undertake. It is based on the Boussinesq approximation but it includes additional physical effects stemming from the advection term in the Navier–Stokes equations. It allows it to accurately cast rapidly rotating flows with mild variations of density into an incompressible formulation. In section §2, we describe a systematic way to achieve this, and we provide two different and easy to implement ways to account for centrifugal buoyancy effects in rotating problems.

We compare the different ways of including centrifugal effects in the Boussinesq-Navier-Stokes equations by numerically studying the linear stability of fluid between two differentially rotating cylinders subject to a negative radial temperature gradient. Apart from its intrinsic interest, this setting has been widely used to model both atmospheric (Hide & Fowlis, 1965) and astrophysical flows (Petersen *et al.*, 2007), where the fluid reaches high rotational speeds. Our simulations show that the traditional Boussinesq approximation (i.e. with the $\rho'\Omega^2$ term) is valid in a wide range of angular speeds. However, for rapidly rotating flows important centrifugal effects arise. Here even the linear behavior of the problem is significantly different for both approximations, justifying the application of our approximation to account for centrifugal effects.

The chapter is organized as follows. After introducing the new approximation in section 4.2, we compare it in section 4.3 to other approximations used in accretion disk models. Section 4.4 gives a description of the system as well as the governing equations of the problem. In section 4.5 the linear stability of the system considering both ways to introduce the centrifugal buoyancy is compared. Various cases of interest are analyzed. In 4.5.1 we consider fluid rotating as a solid body, whereas in 4.5.2 shear is introduced in the system. We study first a system rotating close to solid body subjected to weak shear, and subsequently, a quasi-Keplerian rotating fluid is analyzed. Discussion and concluding remarks are given in section 4.6.

4.2 Boussinesq-type approximation for the centrifugal term

In rotating thermal convection or stratified fluids the Navier-Stokes-Boussinesq equations are usually formulated in the rotating reference frame, with angular velocity vector $\mathbf{\Omega}$.

The momentum equation in this non-inertial reference frame includes four inertial body force terms (Batchelor, 1967), also called d'Alembert forces:

$$\begin{aligned}\rho(\partial_t + \mathbf{u}\cdot\nabla)\mathbf{u} = &-\nabla p + \nabla\cdot\boldsymbol{\sigma} + \rho\,\mathbf{f} - \rho\nabla\Phi \\ &- \rho\mathbf{A} - \rho\,\boldsymbol{\alpha}\times\mathbf{r} - 2\rho\,\boldsymbol{\Omega}\times\mathbf{u} - \rho\,\boldsymbol{\Omega}\times(\boldsymbol{\Omega}\times\mathbf{r}).\end{aligned} \tag{4.1}$$

Here $-\rho\mathbf{A}$ is the translation force due to the acceleration $\mathbf{A}$ of the origin of the rotating reference frame, $-\rho\,\boldsymbol{\alpha}\times\mathbf{r}$ is the azimuthal force (also called Euler force) due to the angular acceleration $\boldsymbol{\alpha} = d\boldsymbol{\Omega}/dt$, $-2\rho\mathbf{u}\times\boldsymbol{\Omega}$ is the Coriolis force and $-\rho\,\boldsymbol{\Omega}\times(\boldsymbol{\Omega}\times\mathbf{r})$ is the centrifugal force (all of them per unit volume). In (4.1), ρ, p and $\mathbf{u}$ are the density, pressure and velocity field of the fluid, $\mathbf{r}$ is the position vector of the fluid parcel, and Φ is the gravitational potential, so $-\rho\nabla\Phi$ is the gravitational force. The term $\rho\mathbf{f}$ accounts for additional body forces that may act on the fluid. For a Newtonian fluid the stress tensor $\boldsymbol{\sigma}$ reads

$$\boldsymbol{\sigma} = -p\,\mathbb{I} + \mu(\nabla\mathbf{u} + \nabla\mathbf{u}^T) + \lambda\nabla\cdot\mathbf{u}\,\mathbb{I}, \tag{4.2}$$

where $\mathbb{I}$ is the identity tensor, μ is the dynamic viscosity, and λ is the second viscosity.

4.2.1 The Boussinesq approximation in a rotating reference frame

In the Boussinesq approximation all fluid properties are treated as constant, except for the density, whose variations are considered only in the "relevant" terms. Density variations are assumed to be small: $\rho = \rho_0 + \rho'$, with ρ_0 constant and $\rho'/\rho_0 \ll 1$; the ρ' term usually includes the temperature dependence, density variations due to fluid density stratification, density variations in a binary fluid with miscible species of different densities, etc. With this assumption the continuity equation reduces to $\nabla\cdot\mathbf{u} = 0$ and the fluid can be treated as incompressible. As a direct consequence the shear stress term in the momentum equation (4.1) simplifies to the vector Laplacian, i.e. $\nabla\cdot\boldsymbol{\sigma} = \mu\nabla^2\mathbf{u}$.

Identifying the relevant terms in the momentum equation is a more delicate issue. Any term in (4.1) with a factor ρ splits into two terms, one with a factor ρ_0 and the other with a factor ρ'. If a ρ_0 term is not a gradient, it is the leading-order term, and the associated ρ' term may be neglected. If the ρ_0 term is a gradient, it can be absorbed into the pressure gradient and does not play any dynamical role, and therefore the associated ρ' term must be retained in order to account for the associated force at leading order. This is exactly what happens with the gravitational term: $-\rho_0\nabla\Phi = \nabla(-\rho_0\Phi)$, which is

absorbed into the pressure gradient term and we must retain the $-\rho'\nabla\Phi$ term to account for gravitational buoyancy. The same treatment must be applied to the translation and centrifugal terms, yielding the gradient terms

$$-\rho_0\mathbf{A} - \rho_0\boldsymbol{\Omega}\times(\boldsymbol{\Omega}\times\mathbf{r}) = \nabla\big(\frac{1}{2}\rho_0|\boldsymbol{\Omega}\times\mathbf{r}|^2 - \rho_0\mathbf{A}\cdot\mathbf{r}\big), \tag{4.3}$$

as well as $-\rho'\mathbf{A}$ and $-\rho'\boldsymbol{\Omega}\times(\boldsymbol{\Omega}\times\mathbf{r})$, which must be also retained.

The ρ_0 part of the remaining terms in equation (4.1) (so far, we have considered the gravitational, centrifugal and translational forces) are not gradients, so they are retained as leading order terms and the corresponding ρ' terms are neglected, leading to the Boussinesq approximation equations in the rotating reference frame:

$$\begin{aligned}\rho_0(\partial_t + \mathbf{u}\cdot\nabla)\mathbf{u} &= -\nabla p^* + \mu\nabla^2\mathbf{u} + \rho\,\mathbf{f} - \rho'\nabla\Phi \\ &\quad - \rho'\mathbf{A} - \rho_0\boldsymbol{\alpha}\times\mathbf{r} - 2\rho_0\boldsymbol{\Omega}\times\mathbf{u} - \rho'\boldsymbol{\Omega}\times(\boldsymbol{\Omega}\times\mathbf{r}),\end{aligned} \tag{4.4}$$

where

$$p^* = p + \rho_0\Phi - \frac{1}{2}\rho_0|\boldsymbol{\Omega}\times\mathbf{r}|^2 + \rho_0\mathbf{A}\cdot\mathbf{r}, \tag{4.5}$$

together with the incompressibility condition $\nabla\cdot\mathbf{u} = 0$. Of course, supplementary equations are often needed; for example, if ρ' depends on the temperature, an evolution equation for the temperature must be included.

4.2.2 Formulation in the inertial frame

In many cases the fluid container is not rotating at a given angular speed, but different parts may rotate independently. For example Taylor-Couette flows with stratification and/or heating, cylindrical containers with the lids rotating at different angular velocities, etc. In these flows, there is not a natural or unique angular velocity $\boldsymbol{\Omega}$ to use in (4.4) and it may be more convenient to write the governing equations in the laboratory reference frame. In this section we first derive the momentum equation in the laboratory frame but for the sake of simplicity we assume that the fluid container rotates with angular speed $\boldsymbol{\Omega}$. Later we show how the formulation is easily extended to account for the general case where a unique rotating reference frame cannot be identified.

Formulation in the inertial frame: container rotating at angular velocity $\boldsymbol{\Omega}$

The laboratory frame is an inertial reference frame, so the four inertial terms in (4.1) are absent, and the momentum equation is

$$\rho(\partial_t + \mathbf{v}\cdot\nabla)\mathbf{v} = -\nabla p + \mu\nabla^2\mathbf{v} - \rho\nabla\Phi + \rho\,\mathbf{f}, \tag{4.6}$$

where we have used $\mathbf{v}$ for the velocity field in the inertial reference frame, to distinguish it from the velocity $\mathbf{u}$ in the rotating frame. In order to implement the Boussinesq approximation, we could naïvely repeat the previous analysis; since the only term which is a gradient is the gravitational force $-\rho_0\nabla\Phi$, we end up with an equation containing only the gravitational buoyancy, and the centrifugal buoyancy is absent. This appears reasonable, because the governing equations do not contain the rotation frequency $\boldsymbol{\Omega}$ of the container. However, $\boldsymbol{\Omega}$ appears in the boundary conditions for the velocity, so it must be taken into account by a careful analysis of the nonlinear advection term. The easiest way to do this is by decomposing the velocity field as $\mathbf{v} = \mathbf{u} + \boldsymbol{\Omega}\times\mathbf{r}$, so the $\boldsymbol{\Omega}\times\mathbf{r}$ part accounts for the boundary conditions (rotating container); $\mathbf{u}$ is precisely the velocity of the fluid in the rotating reference frame, with zero velocity boundary conditions. The advection term splits into four parts:

$$\mathbf{v}\cdot\nabla\mathbf{v} = \mathbf{u}\cdot\nabla\mathbf{u} + \mathbf{u}\cdot\nabla(\boldsymbol{\Omega}\times\mathbf{r}) + (\boldsymbol{\Omega}\times\mathbf{r})\cdot\nabla\mathbf{u} + (\boldsymbol{\Omega}\times\mathbf{r})\cdot\nabla(\boldsymbol{\Omega}\times\mathbf{r}). \tag{4.7}$$

Using the incompressibility character of $\mathbf{u}$, the dependence of $\boldsymbol{\Omega}$ on time but not on the spatial coordinates, and some vector identities, we can transform the advection term into

$$\mathbf{v}\cdot\nabla\mathbf{v} = \mathbf{u}\cdot\nabla\mathbf{u} + 2\,\boldsymbol{\Omega}\times\mathbf{u} + \boldsymbol{\Omega}\times(\boldsymbol{\Omega}\times\mathbf{r}) + \nabla\times\big(\mathbf{u}\times(\boldsymbol{\Omega}\times\mathbf{r})\big). \tag{4.8}$$

We have recovered the Coriolis and centrifugal terms, and because $\boldsymbol{\Omega}\times(\boldsymbol{\Omega}\times\mathbf{r})$ is a gradient, we must add a centrifugal contribution also in the inertial reference frame.

The last term in (4.8) accounts for the difference between the time derivatives in the inertial and rotating reference frames respectively. An easy way to see this is by considering the simple case where the two reference frames have the same origin, and $\boldsymbol{\Omega} = \Omega\hat{\mathbf{k}}$, where $\hat{\mathbf{k}}$ is the vertical unit vector and Ω is constant. Using cylindrical coordinates (r,θ,z), with z in the vertical direction, we obtain

$$\nabla\times\big(\mathbf{u}\times(\boldsymbol{\Omega}\times\mathbf{r})\big) = \Omega\partial_\theta\mathbf{u}. \tag{4.9}$$

The change of coordinates between the inertial and rotating frame is

$$\left.\begin{aligned} r &= r', & z &= z', \\ \theta &= \theta' + \Omega t, & t &= t', \end{aligned}\right\} \tag{4.10}$$

where (r', θ', z') are the cylindrical coordinates in the rotating frame of the same fluid parcel with coordinates (r, θ, z) in the inertial frame; t and t' are the times in both reference frames. From (4.10) we obtain $\partial_{t'} = \partial_t + \Omega\partial_\theta$, so the last term in (4.8), combined with $\partial_t \mathbf{u}$ results in the term $\partial_{t'}\mathbf{u}$ in the rotating frame. Finally, $\partial_t \mathbf{v}$ in the inertial frame contains an extra term, $\partial_t(\boldsymbol{\Omega} \times \mathbf{r}) = \boldsymbol{\alpha} \times \mathbf{r}$. Therefore, we have recovered all the inertial forces in the rotating frame (4.1), except for the translation force $-\rho\mathbf{A}$, because in the example considered, (4.10), both reference frames have the same origin, and the translation is absent; by including a translation term in (4.10) we could also recover it. Now, the two formulations, including centrifugal buoyancy in both reference frames (inertial and rotating), fully agree.

In the inertial reference frame, we are interested in a formulation in terms of the velocity field in the inertial frame $\mathbf{v}$, instead of $\mathbf{u}$ as in (4.8). The analysis presented above considering the advection term results simply in an additional term, the centrifugal buoyancy. We have also discussed the effect of the decomposition $\mathbf{v} = \mathbf{u} + \boldsymbol{\Omega} \times \mathbf{r}$ in the time derivative term. Now it only remains to consider the viscous term. However, $\nabla^2(\boldsymbol{\Omega} \times \mathbf{r}) = 0$ because $\boldsymbol{\Omega} \times \mathbf{r}$ is linear in the spatial coordinates and so its Laplacian is zero. The traditional Boussinesq approximation equations in the inertial reference frame are

$$\rho_0(\partial_t + \mathbf{v} \cdot \nabla)\mathbf{v} = -\nabla p^* + \mu\nabla^2\mathbf{v} + \rho\,\mathbf{f} - \rho'\nabla\Phi - \rho'\boldsymbol{\Omega} \times (\boldsymbol{\Omega} \times \mathbf{r}), \tag{4.11}$$

where $p^* = p + \rho_0\Phi - \frac{1}{2}\rho_0|\boldsymbol{\Omega} \times \mathbf{r}|^2$, and together with the incompressibility condition $\nabla \cdot \mathbf{u} = 0$.

Formulation in the inertial frame: generalization

We have shown that centrifugal buoyancy enters the governing equations via the boundary conditions and the advection term; no other term is affected in the Boussinesq approximation. This now suggests a very simple formulation, consisting in keeping the whole density, $\rho = \rho_0 + \rho'$, in the advection term. This formulation is easy to implement, and since most time-evolution codes for incompressible flows are semi-implicit (i.e. the viscous term is treated implicitly, whereas the advection term is treated explicitly), the speed and efficiency of the codes do not change. The formulation reads

$$\rho_0(\partial_t + \mathbf{v} \cdot \nabla)\mathbf{v} = -\nabla p^* + \mu\nabla^2\mathbf{v} + \rho\,\mathbf{f} - \rho'\nabla\Phi - \rho'(\mathbf{v} \cdot \nabla)\mathbf{v}, \tag{4.12}$$

where $p^* = p + \rho_0\Phi$, and allows one to easily handle situations where different parts of a fluid container rotate independently. In these flows there is not a natural or unique

angular velocity $\mathbf{\Omega}$ to use for a rotating reference frame in the formulation (4.11); however the angular velocities of the problem still enter the governing equations through the boundary conditions and the advection term. Hence formulation (4.12) provides a natural way to account for centrifugal buoyancy effects of these rotating flows in the inertial (laboratory) reference frame. This formulation is also appropriate if additional equations appear coupled with the Navier-Stokes equations, for example for large density variations in stratified flows. The treatment of the centrifugal effects can be carried out exactly in the same way presented here.

Alternative formulation in the inertial frame and physical interpretation

The extra term included in (4.12), $\rho'(\mathbf{v}\cdot\nabla)\mathbf{v}$, can be expressed in a different way, providing a closer resemblance to the expression in (4.11). Close to a rotating wall, the velocity field is $\mathbf{v}\approx\mathbf{\Omega}\times\mathbf{r}$; this expression is exact at the wall (no slip boundary condition at a rigid rotating wall). The dominant part of the advection term is then

$$(\mathbf{v}\cdot\nabla)\mathbf{v}\approx(\mathbf{\Omega}\times\mathbf{r})\cdot\nabla(\mathbf{\Omega}\times\mathbf{r})=\mathbf{\Omega}\times(\mathbf{\Omega}\times\mathbf{r})=-\nabla(\frac{1}{2}|\mathbf{\Omega}\times\mathbf{r}|^2)\approx-\nabla\big(\frac{1}{2}\mathbf{v}^2\big). \quad (4.13)$$

As the dominant term is a gradient, it is necessary to include the ρ' term in the Boussinesq approximation. Replacing $\rho'(\mathbf{v}\cdot\nabla)\mathbf{v}$ by $-\rho'\nabla(\frac{1}{2}\mathbf{v}^2)$ gives the alternative form for (4.12):

$$\rho_0(\partial_t+\mathbf{v}\cdot\nabla)\mathbf{v}=-\nabla p^*+\mu\nabla^2\mathbf{v}+\rho\,\mathbf{f}-\rho'\nabla\Phi+\rho'\nabla\big(\frac{1}{2}\mathbf{v}^2\big). \quad (4.14)$$

This centrifugal effect is not only important when we have rotating walls, but also if a strong vortex appears dynamically in the interior of the domain; therefore it is advisable to always include this term in the Boussinesq approximation in order to account for all possible sources of centrifugal instability.

We have presented two different ways, (4.12) and (4.14), of including the centrifugal buoyancy in rotating problems. One may wonder if there exists a canonical way to extract from the advection term the part that is a gradient, and then multiply this gradient by ρ'. The Helmholtz decomposition (Arfken & Weber, 2005), writing a given vector field as the sum of a gradient and a curl, could serve this purpose, but unfortunately this decomposition is not unique (it depends on the boundary conditions satisfied by the curl part), and moreover it is not a local decomposition (i.e., in order to extract the gradient part, we need to solve a Laplace equation with Neumann boundary conditions). The two formulations presented here, (4.12) and (4.14), are simple and easy to implement, and deciding between one or the other is a matter of taste.

The extra term we have included in (4.14), $\rho'\nabla(\frac{1}{2}\mathbf{v}^2)$, has an important physical interpretation; it is a source of vorticity due to density variations and centrifugal effects. Taking the curl of (4.14) and using

$$\nabla \times (\mathbf{v} \cdot \nabla \mathbf{v}) = \nabla \times (\boldsymbol{\omega} \times \mathbf{v}) = \mathbf{v} \cdot \nabla \boldsymbol{\omega} - \boldsymbol{\omega} \cdot \nabla \mathbf{v}, \tag{4.15}$$

where $\boldsymbol{\omega} = \nabla \times \mathbf{v}$ is the vorticity field, results in an equation for the vorticity:

$$\rho_0(\partial_t + \mathbf{v} \cdot \nabla)\boldsymbol{\omega} = \rho_0 \boldsymbol{\omega} \cdot \nabla \mathbf{v} + \mu \nabla^2 \boldsymbol{\omega} + \nabla \times (\rho\, \mathbf{f}) - \nabla \rho' \times \nabla \Phi + \nabla \rho' \times \nabla\big(\frac{1}{2}\mathbf{v}^2\big). \tag{4.16}$$

The first three terms in the right-hand-side of (4.16) provide the classical vorticity evolution equation for an incompressible flow with constant density. The last two terms are the explicit generation of vorticity due to the gravitational and centrifugal buoyancies, respectively. In the next section we discuss two hydrodynamic approaches to the accretion disk problem in astrophysics, where centrifugal buoyancy is not included, and we show that it can be easily included in the numerical analysis.

4.3 Centrifugal effects in hydrodynamic accretion disk models

There are other approximations used in the literature, which may be also modified to include centrifugal buoyancy. Astrophysics is a very active field where these approximations are used. The book of Tassoul (2000) provides a comprehensive discussion on rotating stellar flows under the influence of shear and stratification. In this section we briefly discuss two approximations used in accretion disk theory. The first is the shearing sheet model (Balbus, 2003; Regev & Umurhan, 2008; Lesur & Papaloizou, 2010), where the Boussinesq approximation is used in a small domain of the accretion disk. The second is the anelastic approximation (Bannon, 1996), used by Petersen *et al.* (2007) in a global model of an accretion disk.

In the shearing sheet approximation the governing equations are written in a small thin rectangular box at a distance r_0 from the center of the accretion disk; the coordinates used are $x = r - r_0$, $y = r_0\theta$, and z, where (r, θ, z) are the cylindrical polar coordinates of the disk. Let $\Omega(r)$ be the Keplerian angular velocity profile of the accretion disk, i.e. its background rotation. The rotating reference frame has $\boldsymbol{\Omega} = \Omega_0 \mathbf{e}_z$, $\mathbf{A} = -r_0\Omega_0^2 \mathbf{e}_r$ and $\boldsymbol{\alpha} = 0$, where $\Omega_0 = \Omega(r_0)$ (see 4.4). In terms of the velocity perturbation with respect to the background rotation, $\mathbf{w} = (u, v, w) = \mathbf{u} - \mathbf{u}_0$, with $\mathbf{u}_0 = r(\Omega(r) - \Omega_0)\mathbf{e}_y$, the governing equations (4.4) are

$$\begin{aligned} \rho_0(\partial_t + \mathbf{w} \cdot \nabla - Sx\partial_y)\mathbf{w} = &-\nabla p^* + \mu \nabla^2 \mathbf{w} - \rho' \nabla \Phi \\ &- 2\rho_0 \boldsymbol{\Omega} \times \mathbf{w} + \rho_0 Su \mathbf{e}_y - 2\rho_0 \Omega_0 Sx \mathbf{e}_x - \rho' \boldsymbol{\Omega} \times \big(\boldsymbol{\Omega} \times (r_0 \mathbf{e}_x + \mathbf{r})\big). \end{aligned} \tag{4.17}$$

Here $S = -r_0 d\Omega/dr|_{r_0}$ is a linear approximation of the shear associated with the background rotation profile $\Omega(r)$. We have assumed as customary that $x \ll r_0$ and expanded $\Omega(r)$ up to first order in x/r_0. We can compare (4.17) with the governing equations in Balbus (2003); Lesur & Papaloizou (2010), and we observe that the centrifugal term $-\rho'\mathbf{\Omega} \times (\mathbf{\Omega} \times \mathbf{r})$ is absent in these references. The baroclinic term $-\rho'\nabla\Phi$ is the only buoyancy term considered in these works, and it points into the radial direction for an axisymmetric mass distribution in the accretion disk. Another source of instability are the shear terms proportional to S, that are independent of the temperature. When centrifugal buoyancy is included, additional terms both in the radial and azimuthal directions appear, competing with the gravitational buoyancy and the shear terms. As a result, the stability analysis and the dynamics of the accretion disk may be modified by the inclusion of centrifugal buoyancy. If the centrifugal effects of internal strong vortices or differential rotation are also taken into account, like in (4.12, 4.14), additional terms may also be included: $-\rho'(\mathbf{v}\cdot\nabla)\mathbf{v}$ or equivalently $\rho'\nabla\left(\frac{1}{2}\mathbf{v}^2\right)$.

The shearing sheet approximation is local, it models a small rectangular neighborhood of a point in the accretion disk. In order to perform a global analysis of the disk in the radial direction, it is necessary to account for large variations in density, which do not fit into the Boussinesq framework. The anelastic approximation is very useful in this case. It is assumed that there is a background state $\rho_0(r)$, $p_0(r)$ in static balance between centrifugal force, gravity and pressure,

$$r\Omega^2(r) = \frac{d\Phi}{dr} + \frac{1}{\rho_0}\frac{dp_0}{dr}, \tag{4.18}$$

and the continuity equation now reads $\nabla\cdot(\rho_0(r)\mathbf{u}) = 0$. The velocity field is not solenoidal, but the governing equations and numerical methods are very similar to those corresponding to the Navier-Stokes-Boussinesq approximation, and in 2D problems (Petersen *et al.*, 2007) a streamfunction can still be defined. Because of the strong differential rotation in the accretion disk problem, the inertial reference frame is usually preferred. As the centrifugal force is included in the static balance (4.18), it may look like centrifugal effects have been included into the governing equations. However, the static balance means that the centrifugal term $-\rho_0\mathbf{\Omega} \times (\mathbf{\Omega} \times \mathbf{r})$ is a gradient, and therefore terms of the form $-\rho'(\mathbf{v}\cdot\nabla)\mathbf{v}$ or $\rho'\nabla\left(\frac{1}{2}\mathbf{v}^2\right)$ should be included in the governing equations, as has been discussed in the preceding section. These terms are not included in studies using the anelastic approximation (Bannon, 1996; Petersen *et al.*, 2007). Therefore centrifugal effects in many geophysical and astrophysical problems could modify the stability analysis and the dynamics obtained so far, particularly at large rotation rates.

4.4 Description of the system

We consider the motion of a fluid of kinematic viscosity ν contained in the annular gap between two concentric infinite cylinders of radii r_i and r_o. The cylinders rotate at independent angular speeds Ω_i and Ω_o. A negative radial gradient of temperature, as in accretion disks, is considered by setting the temperature of the inner cylinder to $T_i = T_c + \Delta T/2$ and the outer cylinder to $T_o = T_c - \Delta T/2$, where T_c is the mean temperature. We fix the radii ratio $\eta = 0.71$, a typical value in experimental facilities, and the Prandtl number $\sigma = 7.16$, corresponding to water. In astrophysics $\sigma \ll 1$ because thermal relaxation is dominated by radiation processes, whereas in geophysics (planetary core and mantle) $\sigma \gg 1$. We assume that the gravitational acceleration is vertical and uniform, as in typical Taylor-Couette experiments. This is in contrast to astrophysical stellar flows, where radial gravity plays a prominent role and cannot be neglected (Tassoul, 2000). For example, the radial buoyancy frequency (absent in our system) defines the stability of rotating astrophysical objects. Similarly, in accretion disks the radial Grashof number (also absent in our system) is more relevant than the vertical one. Another crucial difference is the presence of radial boundaries (cylinders) to drive rotation. As a result, in the quasi-Keplerian regime ($\Omega_i > \Omega_o$ and $r_i^2\Omega_i < r_o^2\Omega_o$) the radial pressure gradient is positive, whereas in accretion disks it may also be negative.

4.4.1 Governing equations

The centrifugal buoyancy in the stationary frame of reference is included as in section 4.2.2

$$\rho_0(\partial_t + \mathbf{v}\cdot\nabla)\mathbf{v} = -\nabla p^* + \mu\nabla^2\mathbf{v} - \rho'\nabla\Phi - \rho'\mathbf{v}\cdot\nabla\mathbf{v}, \tag{4.19}$$

where p^* includes part of the gravitational potential, $\rho_0\Phi$.

We assume $\rho = \rho_0 + \rho' = \rho_0(1 - \alpha T)$, where T is the deviation of the temperature with respect to the mean temperature T_c, and ρ_0 is the density of the fluid at T_c. As the gravity acceleration is vertical and uniform, the gravitational potential is given by $\Phi = gz$; cylindrical coordinates (r, θ, z) are used. With these assumptions, $-\rho'\nabla\Phi = \rho_0\alpha g T\hat{\mathbf{z}}$ where $\hat{\mathbf{z}}$ is the unit vector in the axial direction z and α is the coefficient of volume expansion. The governing equations, including the temperature and incompressibility

condition, are:

$$(\partial_t + \mathbf{v}\cdot\nabla)\mathbf{v} = -\nabla p + \nu\nabla^2\mathbf{v} + \alpha g T\hat{\mathbf{z}} + \alpha T\mathbf{v}\cdot\nabla\mathbf{v}, \tag{4.20a}$$

$$(\partial_t + \mathbf{v}\cdot\nabla)T = \kappa\nabla^2 T, \tag{4.20b}$$

$$\nabla\cdot\mathbf{v} = 0, \tag{4.20c}$$

where κ is the thermal diffusivity of the fluid. The equations are made dimensionless using the gap width $d = r_o - r_i$ as the length scale, the viscous time d^2/ν as the time scale, ΔT as the temperature scale, and $(\nu/d)^2$ for the pressure. In doing so, six independent dimensionless numbers appear:

Grashof number	$G = \alpha g \Delta T d^3/\nu^2,$	(4.21a)
relative density variation	$\epsilon = \alpha\Delta T = \Delta\rho/\rho_0,$	(4.21b)
Prandtl number	$\sigma = \nu/\kappa,$	(4.21c)
radius ratio	$\eta = r_i/r_o,$	(4.21d)
inner Reynolds number	$\mathrm{Re}_i = \Omega_i r_i d/\nu,$	(4.21e)
outer Reynolds number	$\mathrm{Re}_o = \Omega_o r_o d/\nu.$	(4.21f)

where $\Delta\rho$ is the density variation associated with a temperature change of ΔT. In this system the Froude number is not particularly useful because we have two different rotation rates, Ω_i and Ω_o, so the Froude number definition is not unique.

From now on, only dimensionless variables and parameters will be used. The dimensionless governing equations are:

$$(\partial_t + \mathbf{v}\cdot\nabla)\mathbf{v} = -\nabla p + \nabla^2\mathbf{v} + GT\hat{\mathbf{z}} + \epsilon T\mathbf{v}\cdot\nabla\mathbf{v}, \tag{4.22a}$$

$$(\partial_t + \mathbf{v}\cdot\nabla)T = \sigma^{-1}\nabla^2 T, \tag{4.22b}$$

$$\nabla\cdot\mathbf{v} = 0, \tag{4.22c}$$

The only change needed to recover the traditional Boussinesq approximation is to replace the centrifugal term $\epsilon T\mathbf{v}\cdot\nabla\mathbf{v}$ in (4.22a) by $-\epsilon\Omega^2 T r\hat{\mathbf{r}}$, where $\hat{\mathbf{r}}$ is the unit vector in the radial direction r.

4.4.2 Methodology

The code described in 2.4 has been used to analyze the linear stability of equations (4.22) when the centrifugal term is included with the new and traditional Boussinesq

approximations. The base flow, which in this case is calculated analytically, the linearized equations and the numerical method used to deal with the resulting eigenvalue problem are comprehensively discussed in 2.4. From (2.22) the equations for the traditional Boussinesq approximation can be easily obtained by setting $\epsilon = 0$ in all terms except for $-\epsilon(v_b^2/r)T'$. The traditional approximation incorporates only one rotating frame of reference for the system; the expression (2.18b) for the base flow azimuthal velocity $v_b(r) = Ar + B/r$ has two terms, Ar corresponding to solid body rotation, and B/r corresponding to shear. It is natural to identify A as the frequency of the rotating frame of reference, Ω_r. In fact, if we take $\Omega_i = \Omega_o = \Omega$, the Couette flow profile is:

$$v_b(r) = Ar + \frac{B}{r} = \frac{\Omega_o r_o^2 - \Omega_i r_i^2}{r_o^2 - r_i^2} r + \frac{(\Omega_i - \Omega_o)(r_i r_o)^2}{r_o^2 - r_i^2} \frac{1}{r} = \Omega r = \Omega_r r, \tag{4.23}$$

and we recover the linearized version of the centrifugal term considered in the traditional approach, $-\epsilon\Omega^2 T' r\hat{\mathbf{r}}$. In the general case with $\Omega_i \neq \Omega_o$ the traditional Boussinesq approximation is defined in the frame of reference rotating with $\Omega_r = A$. This approximation takes only into account the centrifugal buoyancy acting in the radial direction, which is obviously its main contribution. However, as we will see in 4.5, for high rotation rates other terms acting both in the radial and azimuthal directions become important and change the behavior of the system. Part of the discrepancy stems from the fact that the effect of differential rotation is entirely neglected in the traditional approximation.

4.5 Stability of differentially heated fluid between co-rotating cylinders

In this section we present a detailed comparison of the linear stability of the system using the traditional Boussinesq approximation and the new approximation (2.22). We consider three different cases, all with $\eta = 0.71$ and $\sigma = 7.16$. In the first one the cylinders are rotating at same angular speed, corresponding to fluid rotating as a solid-body. In the second and third cases the stability of a differentially rotating fluid is considered in the presence of weak and strong (quasi-Keplerian) shear.

4.5.1 Cylinders rotating at same angular speed

In this case a rotating frame of reference is readily identified and the shear term B/r in the base flow azimuthal velocity (2.18b) is zero, whereas the term A corresponds to

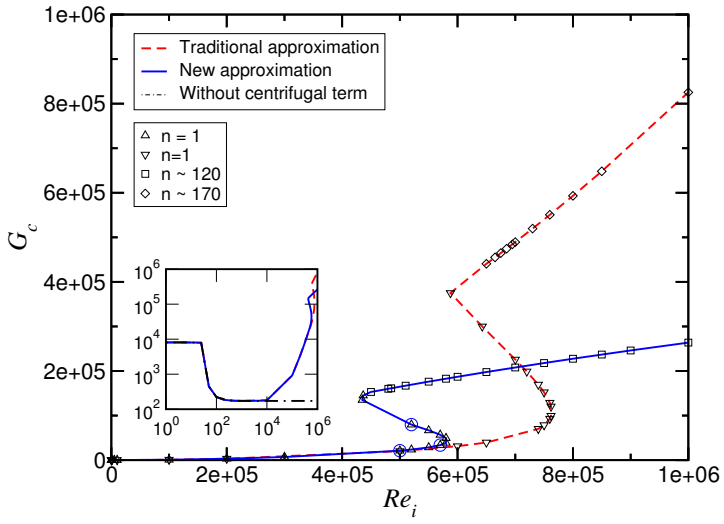

Figure 4.1: Critical Grashof number G_c as function of inner cylinder Reynolds number Re_i for fluid rotating as a solid-body. The solid line is the linear stability curve using the new approximation for the centrifugal buoyancy proposed in this paper, the dashed corresponds to the traditional Boussinesq approach, whereas the dotted-dashed line is the case without centrifugal buoyancy, which can only be distinguished from the horizontal axis in the inset (log-log axes). Different symbols indicate the two distinct mechanisms of instability. Up and down triangles represent the critical points due to the mechanism at moderate Re_i for the new and traditional approximations respectively, whereas squares and diamonds correspond to the mechanism at large Re_i.

the angular velocity of the cylinders. Figure 4.1 shows the critical values of G as the rotation speed, indicated here by the inner cylinder Reynolds number Re_i, is increased. In the case of stationary cylinders instability sets in at $G = 8087.42$, with $k_c = -2.74$ and $n = 0$. The emerging pattern is characterized by pairs of counter-rotating toroidal rolls, that unlike Taylor vortices have a non-zero phase velocity that causes a slow drift of the cellular pattern upward. Extensive information about natural convection instabilities can be found in the literature: Choi & Korpela (1980) and McFadden *et al.* (1984) for infinite geometries, and de Vahl Davis & Thomas (1969) and Lee *et al.* (1982) for finite geometries. Without rotation, traditional (dashed line) and new (solid line) approximations yield identical results to the case where centrifugal buoyancy is neglected (dashed-dotted line). For slow rotation the effect of the centrifugal buoyancy is negligible, and nearly the same critical values are obtained in each case (see inset in figure 4.1). As rotation is increased, the flow is strongly stabilized by centrifugal buoyancy. Note that if this is neglected, the onset of instability asymptotically approaches $G_c = 172.50$ and is qualitatively wrong. The presence of the centrifugal term in any of the ways considered here, entirely modifies the stability of the problem and consequently is an essential element to study these flows. No differences between the two approximations in the linear behavior of the system are observed up to $\mathrm{Re}_i \sim 5 \times 10^5$, where the two curves start to depart from each other. Up to this point and after a small initial region where several azimuthal modes up to $n = 6$ are involved, the base flow loses stability to an azimuthal mode $n = 1$ with small axial wavenumber $k \sim 10^{-3}$. The shape of the critical modes along the stability curve is illustrated in figure 4.2, showing contours of constant temperature in a horizontal cross-section. The three states correspond to the circles in figure 4.1 and depict the transition between the lower and intermediate branches as we consider the new approximation. As we proceed forward along the critical curve the cold fluid progressively penetrates into the warm fluid and vice versa. The same behavior is observed when the traditional approximation is used, nevertheless the values of Re_i and G_c required are larger.

As Re_i increases beyond 5×10^5 the new terms in our approximation start becoming important and lead to different behavior in the linear stability of the system. An analysis of the magnitude of each term in our approximation reveals that the differences observed in figure 4.1 at high Re_i are due to terms involving the product $v_b u_\theta$, implying the existence of an important centrifugal force acting in azimuthal direction as high rotational speeds are reached. This provides evidence that the traditional formulation, including only the main (radial) contribution of centrifugal buoyancy, is a very good approximation if slow rotation is involved but other contributions may not be neglected

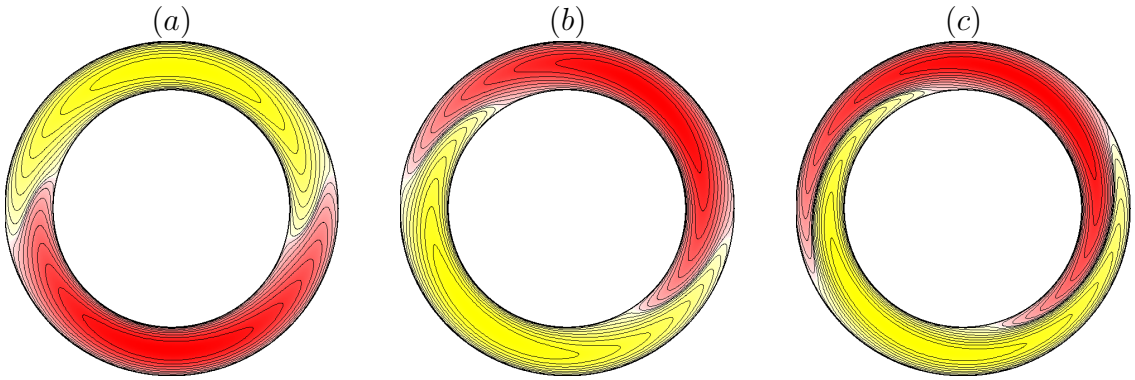

Figure 4.2: Contours of the temperature disturbance T' at a z-constant section corresponding to the points marked as blue circles in figure 4.1. (a): $\mathrm{Re}_i = 5 \times 10^5$, $G_c = 21206.53$. (b): $\mathrm{Re}_i = 5.7 \times 10^5$, $G_c = 33768.37$. (c): $\mathrm{Re}_i = 5.2 \times 10^5$, $G_c = 79670.16$. There are 10 positive (dark gray; red in the online version) and 10 negative (light gray; yellow in the online version) linearly spaced contours. In all cases the critical azimuthal mode is $n = 1$ and $k = O(10^{-3})$.

in rapidly rotating fluids. Once the critical values given by both approximations differ, we can identify two interesting regions in parameter space. For $\mathrm{Re}_i \in [5 \times 10^5, 7.7 \times 10^5]$ the traditional Boussinesq approach yields larger critical G than our approximation, whereas for $\mathrm{Re}_i > 7.7 \times 10^5$ the upper branch of the new approximation yields much lower critical values. Moreover, the differences keep increasing as Re_i grows.

The analysis performed reveals the existence of two mechanisms of instability associated with the lower-intermediate and upper branches in figure 4.1. Different symbols are used to represent the critical values corresponding to each mechanism in each problem. The differences between them are illustrated in figure 4.3, showing the evolution of the critical axial wavenumber k_c and the angle of the spiral modes $\arctan(\frac{k_c}{n})$ versus Re_i. Two regions with distinct characteristics are well-defined. The first mechanism of instability has already been presented (see figure 4.2). Low azimuthal wavenumbers, primarily $n = 1$, and very small axial wavenumbers characterize it. This corresponds to quasi two-dimensional modes and can be readily seen in figure 4.3(b), showing that the angle of the spiral modes remains constant at about 90 degrees. The inset shows the small initial region where the spiral angle increases progressively until it reaches a vertical position. The second mechanism is characterized by $n > 80$ and $k_c \sim O(1)$, also corresponding to quasi two-dimensional modes (see figure 4.3b). Another common feature between the two types of instabilities is that the rotational frequency coincides with the angular velocity of the container in both mechanisms and both approximations. This is in agreement with Maretzke *et al.* (2014), who have analytically proven that two-

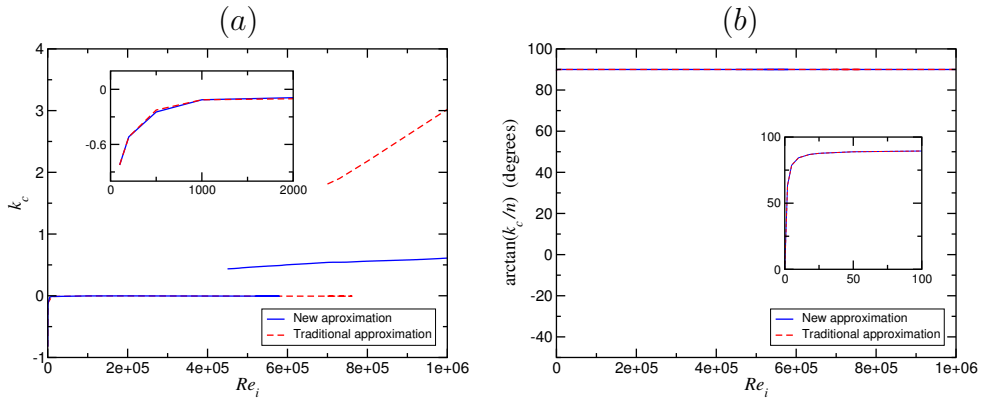

Figure 4.3: (a) Critical axial wavenumber k_c and (b) spiral angle of the modes $\arctan(k_c/n)$ as a function of Re_i for the curves in figure 4.1. The inset is a close up at low Re_i where the first mechanism stops being dominant and is superseded by spiral modes with angle far from 90 degrees, indeed 0, corresponding to $n = 0$, at $Re_i = 0$.

dimensional modes with $k = 0$ always rotate at speed A (2.18b) in Taylor–Couette flows without heating. An interesting distinct feature of the second instability mechanism is localization near the inner cylinder. An example of these wall convection modes is shown in figure 4.4; the critical disturbances are clearly different in the traditional and in the new Boussinesq approximations.

4.5.2 Differentially rotating cylinders

The traditional approximation for the centrifugal buoyancy neglects the part of the base flow containing shear, i.e. the B/r term in (2.18b). To quantify the influence of including shear in the centrifugal terms, we perform the same analysis as in the previous section but for differentially rotating cylinders. The amount of shear introduced is characterized by the ratio of angular velocities $\beta = \Omega_i/\Omega_o$; the further β is from one, the stronger is the shear effect considered.

Weak shear: rotation close to solid body ($\beta = \Omega_i/\Omega_o = 1.006$)

We first consider the case where the container is rotating near solid body. Although shear may be here expected to play only a secondary role, this case serves the purpose of illustrating the importance of including shear effects in the centrifugal term. Figure 4.5 shows the neutral stability curve for the two approaches considered and also without centrifugal buoyancy (dashed-dotted line), which produces qualitatively correct results in

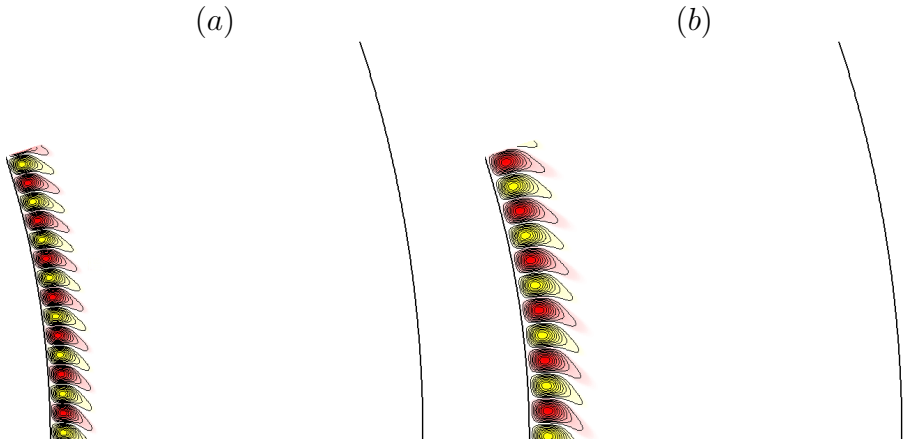

Figure 4.4: Contours of the critical disturbance temperature on a z-constant section for $\mathrm{Re}_i = 700000$. (a) Critical mode using the traditional Boussinesq approximation. Here $G_c = 489371.47$, $k_c = 1.81$ and $n = 150$. (b) Critical mode using the new approximation. Here $G_c = 207906.92$, $k_c = 0.54$ and $n = 116$. In both cases, only 1/20 of the domain is shown. There are 10 positive (darker gray; red online) and negative (light gray; yellow online) contours.

this instance. Unlike in the solid-body case, the critical values G_c increase monotonically as Re_i grows. Besides shear, centrifugal effects are also important in this configuration. From $\mathrm{Re}_i \gtrsim 2\times10^5$ on the linear stability curves obtained by using both approximations become quite different. Similar features with respect to the solid-body case may be identified. At first the traditional approximation gives lower critical value of the Grashof. However, this region is smaller than in the solid-body case and ends at $\mathrm{Re}_i \sim 2.9 \times 10^5$ where both curves intersect. From that point on, the stability region predicted by the new approximation is smaller; the differences between the critical values given by both approximations keep increasing as larger Re_i are considered. At the point where both curves first depart from each other Re_i has half the value of that of the solid-body case. Consequently, the rotational speeds for which the new approximation is necessary are significantly smaller in the presence of weak differential rotation.

Critical axial and azimuthal wavenumbers exhibit similar behavior to the solid-body case and so they are not shown here. Two mechanisms of instability are also found. The first one embraces the region $2 \times 10^5 < \mathrm{Re}_i$ and is characterized by $k_c \sim 0$ and $1 \leq n \leq 6$. Modes are similar to those obtained for the first mechanism in the solid body case. A subtle difference can be nevertheless pointed out. In the solid body situation the temperature disturbances fill the whole annulus, whereas differential rotation confines the perturbation towards the central part (see figure 4.6a). The second mechanism also presents the same features as in the solid body case, high azimuthal modes and

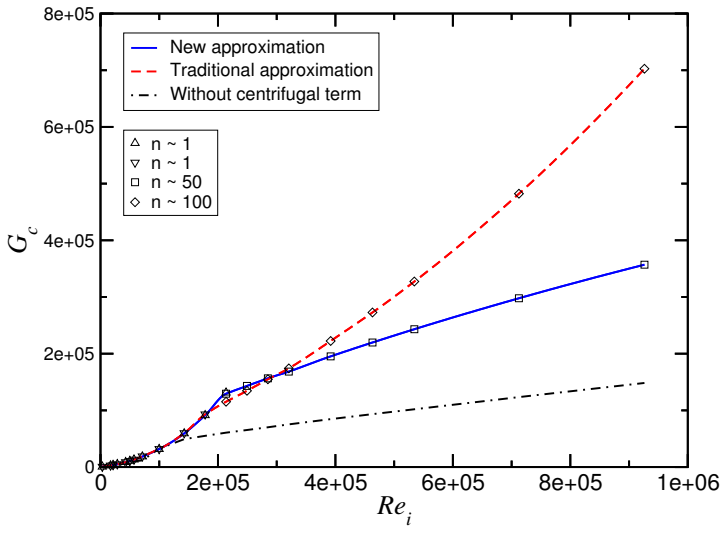

Figure 4.5: Critical Grashof number G_c as function of inner cylinder Reynolds number Re_i for rotation near solid-body ($\beta = 1.006$). Different symbols refer to two distinct instability mechanisms as in figure 4.1.

$k_c \in [0.5, 1.5]$, but differences in the flow appear that deserve to be highlighted. In the traditional approximation the dominant wall modes are located at the inner cylinder, as it occurs in the solid-body case (figure 4.6*b*). In contrast, using the new approximation changes the location of the dominant wall modes to the outer cylinder (figure 4.6*c*). In view of these results we can say that considering shear effects in the centrifugal term of the Navier–Stokes equations may be extremely important: not only regarding the linear stability boundary but also the shape and location of the critical modes.

Strong shear: Quasi-Keplerian rotation ($\beta = \Omega_i/\Omega_o = 1.58$)

If $1/\eta > \beta > 1$ the angular velocity decreases outward but the angular momentum increases. These flows, known as quasi-Keplerian flows, are used as models to investigate the dynamics and stability of astrophysical accretion disks. Here we choose a typical value $\beta = 1.58$ and as in the previous sections consider a negative temperature gradient in the radial direction, as expected in accretion disks. Figure 4.7 shows the neutral stability curve for the two approximations considered, as well as entirely neglecting centrifugal effects ($\epsilon = 0$). The three curves are almost straight lines, that completely overlap in a plot (G_c, Re_i). In order to see the small differences that appear at large Re_i, we have plotted in this case G_c/Re_i versus Re_i. Shear is the completely dominant mechanism in this regime, but small differences can be observed for $Re_i \gtrsim 2 \times 10^5$, that are enhanced in the inset. Surprisingly, shear has a very strong stabilizing effect in this

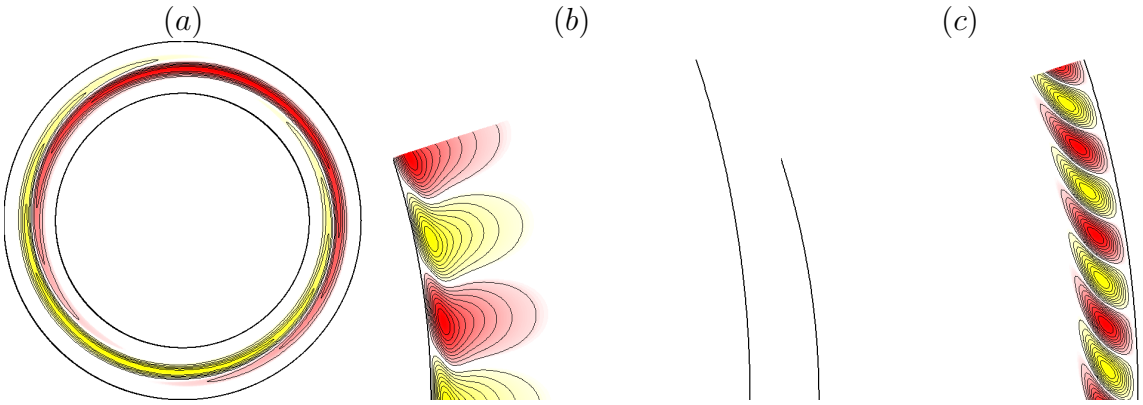

Figure 4.6: Contours of the critical disturbance temperature on a z-constant section. (a) $n = 1$, $\mathrm{Re}_i = 178125$, $G_c = 92987.56$. (b)–(c) Comparison of the traditional (b) and new (c) approximation at $\mathrm{Re}_i = 285000$ (near the crossover point in figure 4.5) showing 1/20 of the annulus. (b) $G_c = 154864.79$, $k_c = 0.24$ and $n = 30$. (c) $G_c = 156547.54$, $k_c = 0.39$ and $n = 75$. There are ten positive (dark gray; red online) and negative (light gray; yellow online) linearly spaced contours.

problem: without shear the critical Grashof number is ten times smaller at $Re_i = 10^6$ than in the quasi-Keplerian case.

Depending on the Reynolds number two mechanisms of instability are again found. The first mechanism exhibits a similar flow structure to that observed in the previous case. It also occurs at low Re_i and is localized in the central part of the annulus due to the action of differential rotation. Figure 4.8(a) shows the contours of the disturbance temperature in an horizontal plane. In contrast to what happens in the weak shear situation, these modes present a clear 3D structure with $k_c \sim -1$. Small azimuthal wavenumbers are involved in this mechanism, ranging from $n = 1$ to $n = 6$. More remarkable differences are found when analyzing the second mechanism. High azimuthal modes $n \sim 50$ arise as this mechanism becomes dominant, but unlike the solid-body and weak shear situations, the azimuthal mode number decreases as Re_i increases. The same behavior is observed in the axial wavenumber, so that the spiral angle quickly converges to 90 degrees as observed in the previous sections. Figure 4.8(b) shows that the instability is characterized by convection wall modes localized at the outer cylinder, as in the case of weak shear using the new approximation. Nevertheless, in quasi-Keplerian flows the dominant modes are always localized at the outer cylinder regardless of how centrifugal terms enter the equations.

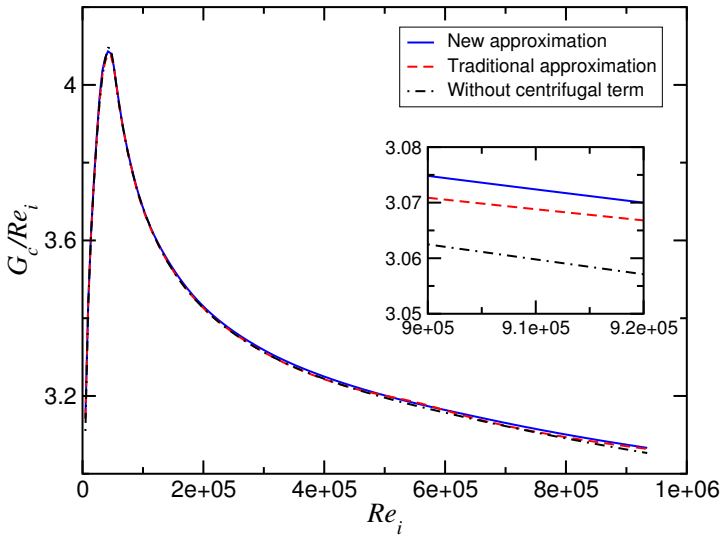

Figure 4.7: Critical ratio G_c/Re_i as function of inner cylinder Reynolds number Re_i for quasi-Keplerian rotation ($\beta = 1.58$). The three curves differ only by about 1% and hence are only distinguishable in the inset.

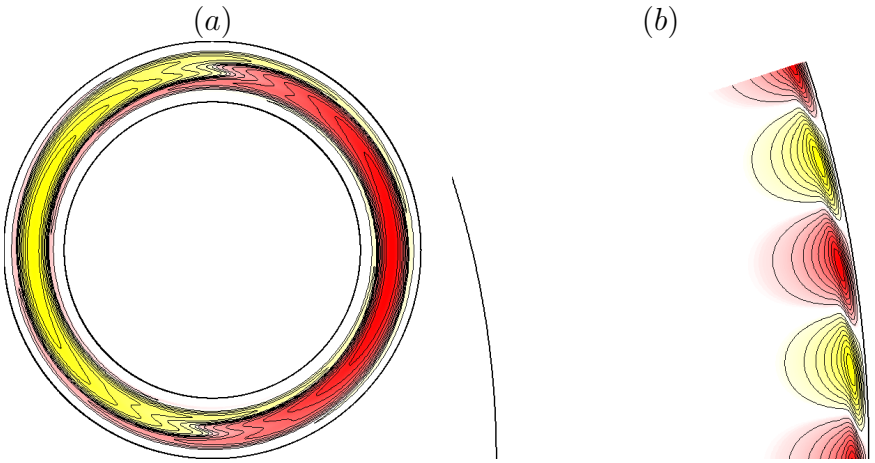

Figure 4.8: Contours of the critical disturbance temperature on a z-constant section. (a) $\mathrm{Re}_i = 11681.03$ with $G_c = 4.1268 \times 10^4$, $k_c = -1.05$ and $n = 1$. (b) $\mathrm{Re}_i = 584051.72$ with $G_c = 1.8511 \times 10^4$, $k_c = 8.21$ and $n = 38$. Ten positive (dark gray; red online) and negative contours (light gray; yellow online) are displayed. Only 1/20 of the domain is shown in (b).

4.6 Summary and discussion

We have identified weaknesses in how the Boussinesq formulation is typically used to account for centrifugal buoyancy in the Navier–Stokes equations. In particular, the traditional approximation (including only the term $\rho'\Omega^2$) neglects the effects associated with differential rotation or strong internal vorticity. This has motivated us to develop a new consistent Boussinesq-type approximation correcting this problem. It consists in keeping the density variations in the advection term of the Navier-Stokes equations and thus it is very easy to implement in an existent solver. The new approximation allows accurate treatment of situations with differential rotation or when strong vortices appear in the interior of the domain, which may cause important centrifugal effects even in flows without global rotation. The latter may be especially relevant in simulations at high Rayleigh numbers (as e.g. in the quest for the 'ultimate regime', Ahlers *et al.*, 2009). Thus we argue that our formulation for the centrifugal terms should be always implemented whenever the Boussinesq approximation is used.

The relevance of the new approximation has been illustrated with a linear stability analysis of a Taylor–Couette system subjected to a negative radial gradient of temperature. Three different cases have been studied. First, we have considered the container rotating as solid-body, i.e. without differential rotation. We note that if centrifugal buoyancy is entirely neglected, the results are even qualitatively wrong. For both traditional and new approximations the critical values obtained agree up to $\mathrm{Re}_i \sim 5.5 \times 10^5$, beyond which discrepancies become significant. Beyond this point the conductive base flow loses stability to quasi two-dimensional wall modes (aligned with the axis of rotation, as expected from the Taylor–Proudman Theorem) localized at the inner cylinder. Note that the large discrepancy in critical Grashof numbers observed at $\mathrm{Re}_i \in [5 \times 10^5, 10^6]$ between both approximations makes it possible to test them against laboratory experiments. For example, in the experiments from Paoletti & Lathrop (2011), and Avila & Hof (2013), which allow for radial temperature gradients, $\mathrm{Re} = 10^6$ can be reached, and the required Grashof numbers 5×10^5 can be obtained with temperature differences about half a degree kelvin.

We have also considered the case in which the cylinders rotate at different angular speeds, thus introducing shear. For weak differential rotation, shear and centrifugal buoyancy effects compete and the critical values obtained with both approximations differ from each other at lower $\mathrm{Re}_i \sim 2 \times 10^5$. Moreover, the new approximation gives rise to wall modes located on the outer cylinder, whereas the traditional approach yields wall modes on the inner cylinder, as in the solid-body case. In quasi-Keplerian flows, shear is so

dominant that centrifugal terms may be entirely neglected in the linear stability analysis (discrepancies in G_c are below 1% regardless of how centrifugal terms enter the equations, if at all). Here the critical modes are always localized at the outer cylinder. Note that such wall modes, similar to those identified by Klahr *et al.* (1999), are not relevant to the accretion disk problem, in which there are no solid radial boundaries. Furthermore, it is worth noting that testing our differential rotation results in the laboratory is very difficult because of axial end wall effects. The large Re involved will necessarily trigger instabilities and transition to turbulence because of the nearly discontinuous angular velocity profile at the junction between axial end walls and cylinders (Avila, 2012).

Although it may be tempting to suggest that laminar quasi-Keplerian flows are stable for weak stratification in the radial direction, our analysis has only axial gravity, and is linear and hence concerned with infinitesimal disturbances only. In more realistic models of accretion disks, nonlinear baroclinic instabilities have been found in similar regimes by Klahr & Bodenheimer (2003), and we expect that subcritical transition via finite amplitude disturbances may occur in the problem investigated here. This remains a key question for incoming numerical and experimental investigations. In fact, even in the classical (isothermal) Taylor–Couette problem this possibility remains open and controversial (see e.g. Balbus, 2011).

CHAPTER 5

INFLUENCE OF THE BOUNDARY CONDITIONS ON SIMPLE MODELS OF BAROCLINIC INSTABILITIES

5.1 Introduction

Since the second half of the past century the baroclinic vorticity production driven by the combination of rotation and thermal gradients has been addressed in an attempt to understand the dynamics of complex geophysical, astrophysical and industrial flows. A laterally heated differentially rotating annulus, often called baroclinic annulus, has been adopted as a simple model to study such flows in the laboratory. The physical mechanism involved in the onset of the baroclinic instability is nowadays well understood, and extensive information about the flow regimes, particularly in a geophysical context, can be found in the literature (see Lappa (2012) for a comprehensive review on this topic). However, an understanding of the source of many of the observed dynamical features is still missing and experiments in baroclinic annuli continue to be an active area of research.

The purpose of this chapter is to analyze the extent to which the stability of baroclinic flows is influenced by the presence of axial end walls. In particular, it is interesting to distinguish features of the flow that arise from the differential rotation and temperature, from those which are determined by end wall boundary layers. To this avail we here investigate the linear stability of the flow in a baroclinic annulus with rigid flat axial boundaries and with axially periodic boundary conditions, which do not generate end wall boundary layers.

We consider the baroclinic annulus in two different contexts depending on the relative rotation of cylinders and sign of the temperature gradient. If the cylinders and end walls rotate at the same angular speeds as a solid-body this model is used to study geophysical flows such as the dynamics of the large-scale flows in the mid-latitudes of the atmosphere or the mesoscale eddies in ocean currents (Pierrehumbert & Swanson, 1995). Although there is an extensive theoretical and experimental literature about this setup (see Hide & Mason (1975) for an excellent review), there are few numerical works mainly focused on reproducing experimental results. Lewis & Nagata (2004) and Sugata & Yoden (1990) reproduced some of the experimental features observed by Fein (1973); Fein & Pfeffer (1976), showing that linear stability analysis correctly predicts the onset of instability in this system. The sequence of flow transitions (Randriamampianina *et al.*, 2006) or

the influence of sloping end walls on the flow stability (Larcher *et al.*, 2013) have also been the subject of recent numerical investigations. The dynamical role of the boundary layers has been vastly addressed from a theoretical point of view (Barcilon, 1964; Holton, 1965; Williams & Robinson, 1974), and it is well known that they significantly stabilize the flow. The results presented in this chapter intend to illustrate in a simple and intuitive way this stabilizing effect, with emphasis being placed in the associated physical mechanisms.

The case of rotating inner cylinder and stationary outer cylinder and end walls is a model for industrial applications such as the cooling of rotating machinery, the solidification of pure metals or techniques of chemical vapor deposition (Kreith, 1968; Singer, 1984; Vivès, 1988). Experiments in this context are not as plentiful as for the previous setup. They can be classified in two groups depending on the geometry of the apparatus. The first group of experiments (Snyder & Karlsson, 1964; Sorour & Coney, 1979; Lepiller *et al.*, 2008) is characterized by large length-to-gap aspect ratio $\Gamma = h/(r_o - r_i) \gg 1$ and narrow gap $\eta = r_i/r_o \lesssim 1$, where r_i and r_o are the radii of the inner and outer cylinder, and h their height. Ali & Weidman (1990) first performed a detailed linear stability analysis of such flows using axial periodicity and reported on the influence of the Prandtl number (σ) and the radius ratio (η) on the stability boundaries. The comparison of their results with previous experiments showed a reasonably good agreement with Snyder & Karlsson (1964) and, to a lesser extent with Sorour & Coney (1979). They attributed the discrepancies to the limitations of linear stability theory and infinite-aspect ratio idealization to capture the experimental details. A similar linear stability analysis (Yoshikawa *et al.*, 2013) reported a good agreement between numerical and related experimental results (Lepiller *et al.*, 2008). Nonlinear simulations for small temperature gradients were provided by Kedia *et al.* (1998) who quantified the heat transfer across the system. A second group of experiments embraces apparatuses with moderate aspect ratio and wide gap. Here, the most remarkable works are due to Ball & Farouk (1987, 1988, 1989), who reported heat transfer measurements as well as the sequence of flow transitions using an experimental setup with $\Gamma = 31.5$ and $\eta \sim 0.5$. Subsequent numerical simulations (Kuo & Ball, 1997) for $\Gamma = 10$ and $\eta = 0.5$ provided insight on the bifurcations taking place in the system, however the results showed significant discrepancies with experiments suggesting strong end walls effects.

The simulations shown in this chapter attempt to elucidate the physical mechanisms causing these discrepancies and also to provide a comparison between these two groups of experiments. Moreover, numerical simulations of astrophysical flows suggest that baroclinic instabilities might be an important mechanism of turbulent transport of mo-

mentum in accretion disks (Klahr & Bodenheimer, 2003). In this context the assumption of axial periodicity is essential, as it simplifies considerably the numerical approach, allowing it to reach large Reynolds numbers. Moreover, it renders an arguably better approximation, as astrophysical accretion flows are not bounded axially. Thus the suitability of laboratory experiments to address this problem will be compromised by the impact of the axial end walls on the dynamics of the flow. The results of this chapter may help in assessing their importance.

The chapter is organized as follows. In section 5.2 we introduce the governing equations and dimensionless numbers. The differences between the basic flows of finite and infinite systems are also discussed. The methodology utilized to deal with the equations is specified in section 5.3. In section 5.4 the linear stability of a laterally heated annulus with rotating inner cylinder is considered. A comparison of the critical boundaries when using rigid flat lids and axial periodicity is presented. The sequence of flow transitions and the variation of the heat transfer coefficient (Nusselt number) when varying the control parameters are also illustrated in each case. The stability of a solid-body rotating laterally heated annulus is shown in section 5.5. A similar comparison to that in 5.4 is provided. Finally, in section 5.6 the main conclusions and remarks are outlined.

5.2 Specification of the system

We consider the motion of an incompressible fluid of kinematic viscosity ν confined in the annular gap between two rigid and concentric rotating cylinders of radii r_i and r_o in two different experimental setups:

- Industrial setup: the inner cylinder is rotating at an angular velocity Ω, whereas the outer cylinder and end walls are kept at rest. A radial thermal gradient is considered by setting the inner cylinder to $T_i = T_c + \Delta T/2$ and the outer cylinder to $T_o = T_c - \Delta T/2$, where T_c is the mean temperature of the fluid.
- Atmospheric setup: the container is rotated as a solid body with angular velocity Ω. In this case the system is heated from the outer cylinder so that the temperatures are opposed to the industrial setup, $T_o = T_c + \Delta T/2$ and $T_i = T_c - \Delta T/2$.

In both cases we assume a vertical and uniform gravitational acceleration g. We study flows with end walls and with periodic boundary conditions. The latter model the

case of infinitely long cylinders, whereas the former reproduce experimental boundary conditions (no-slip for the velocity and thermally insulating end walls).

5.2.1 Governing equations

The same set of equations and dimensionless numbers as in chapter 4 (see section 4.4.1) are considered. Since the outer cylinder is at rest in the industrial setup, $\mathrm{Re}_o = 0$. Centrifugal effects are included in the formulation of the problem through the Boussinesq-type approximation discussed in chapter 4. The control parameters are Re_i and G, whereas the rest of dimensionless numbers have been fixed according to previous experimental and numerical works.

5.2.2 Basic flow

The assumption of axial periodicity allows to considerably simplify the calculation of the basic flow. Owing to the missing end walls the radial velocity is zero and the rest of variables only depend on the radial component. Under these conditions an analytical solution can be found by imposing the zero axial mass flux condition to fix the axial pressure gradient. The resulting steady basic flow is given in 2.4.1.

The presence of end walls in the system leads to the appearance of non-zero radial velocities, modifying the meridional circulation. This strongly affects the base flow calculation since velocity field and temperature depend now on the radial and axial components (r, z). This entails a numerical approach and switches on the contribution of terms which were zero under the axial periodicity assumption. This is especially important in equation (4.22b). If we develop the advection term (4.22b) reads

$$\partial_t T_b + u_b \partial_r T_b + \frac{v_b}{r} \partial_\theta T_b + w_b \partial_z T_b = \sigma^{-1} \nabla^2 T_b, \tag{5.1a}$$

In the infinite case the laminar flow is steady, has no radial velocity ($u_b = 0$) and the temperature (T_b) depends only on r, so all terms in the left hand side are zero. Consequently the basic flow remains unaffected by changes in the fluid properties (σ effect). In contrast, the influence of σ may play a significant role in bounded systems, modifying the basic flow with respect to the idealized periodic situation and thus becoming an important source of discrepancies between the critical stability values in both cases.

5.3 Methodology

The onset of instability was determined via linear stability analysis of the basic flow. Fully nonlinear solutions were also computed in order to obtain the flow patterns occurring in different regions of the parameter space. Here only a brief summary of the codes used for the simulations is given. Details can be found in chapter 2.

5.3.1 Axially periodic boundary conditions

The linear stability analysis was performed using the Petrov-Galerkin scheme of Meseguer *et al.* (2007), which we recently extended to account for non-isothermal flows with the Boussinesq approximation (see 2.4). Here up to 50 Chebyshev radial modes have been used to obtain converged results. Fully nonlinear simulations of the three-dimensional Navier-Stokes equations have been performed using a Boussinesq-extension of the finite-difference-Fourier-Galerkin (hybrid MPI-OpenMP) code of Shi *et al.* (2015) (see 2.3).

5.3.2 Rigid flat end walls

For the simulations with physical no-slip boundary conditions at the end walls we have used the numerical code described in 2.2. The critical stability values are measured from the slope of the modal kinetic energy along the linear regime

$$E_m = \int_0^{2\pi} \int_{-\Gamma/2}^{\Gamma/2} \int_{r_i}^{r_o} \boldsymbol{u}_m \boldsymbol{u}^*{}_m r \mathrm{d}r \mathrm{d}z \mathrm{d}\theta \,, \tag{5.2}$$

where $\boldsymbol{u}_m$ is the mth Fourier mode of the velocity field and $\boldsymbol{u}^*{}_m$ is its complex conjugate. In the simulations presented here the numerical resolution has been chosen to ensure that the infinite norm of the spectral coefficients decays at least four orders in magnitude. Time steps as small as $\delta t = 1 \times 10^{-6}$ have been required for numerical stability and accuracy of the second-order temporal scheme.

5.4 Rotating heated inner cylinder

We begin by studying the stability of fluid heated at the inner cylinder and cooled at the outer cylinder. In addition, the inner cylinder rotates at a constant angular speed,

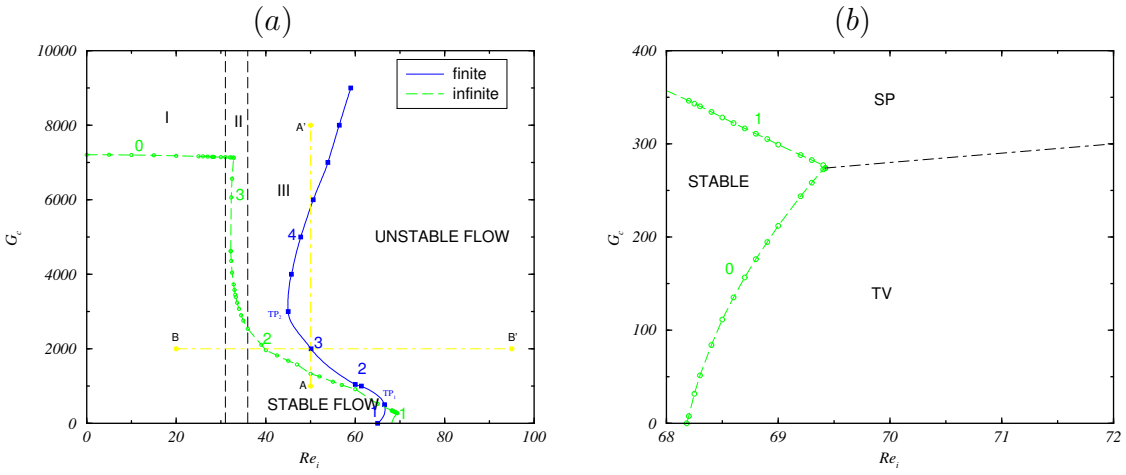

Figure 5.1: (a) Critical stability boundaries (G_c vs Re_i) in a system with rotating heated inner cylinder. The numbers that appear on top of the critical curves are the azimuthal modes associated to the critical perturbations. (Blue) Solid line and squares are used for the finite cylinders case, whereas (green) dashed line and circles stand for the marginal stability in the infinite cylinders case. The working fluid is air ($\sigma = 0.71$) and the geometric parameters are $\eta = 0.5$ and $\Gamma = 10.0$ (in the finite case). (b) Detail of the marginal curve for low G in the infinite cylinders case. The (black) dashed-dotted line marks the transition between spiral flow (SP) and Taylor vortices (TV) after the basic flow is unstable.

whereas the outer cylinder is held stationary. For the analysis we chose the setup used by Kuo & Ball (1997), who used air as the working fluid ($\sigma = 0.71$). The aspect-ratio is $\Gamma = 10$ and the radius ratio is $\eta = 0.5$, which fully specifies the geometry.

In a laterally heated system the meridional circulation is responsible for the convective heat transport between the cylinders. In an infinite system, in which the basic flow has zero radial velocity, the heat transport is purely conductive as long as the basic flow is stable. In contrast, in the finite case the presence of end walls results in strong radial velocities near the lids, commonly referred to as Ekman viscous layers, which enable the convective heat transfer across the system even for laminar flow (Greenspan, 1968; Hide & Mason, 1975). In addition to modifying the convective heat transfer rate, the Ekman layers play an essential role in the dynamics of the flow, especially at large G where infinite and finite systems show a completely opposite behavior (see figure 5.1(a)).

5.4.1 Axially periodic boundary conditions

Primary instability

The stability boundary ((green) dashed line in figure 5.1(a)) has been split into 3 regions corresponding to different mechanisms of instability. Region I is characterized by weak rotation. As G increases, the conductive heat flux becomes insufficient to exchange heat and the basic flow becomes unstable to axisymmetric counter-rotating toroidal rolls. These convection rolls are similar to Taylor vortices, but unlike them, they have an upward non-zero phase velocity. An extensive characterization of these structures for the free convection problem can be found in de Vahl Davis & Thomas (1969).

As the rotation increases the primary instability changes from axisymmetric convection rolls to spiral modes in Region II. This transition occurs for $\mathrm{Re}_i \approx 32$ as the baroclinic vorticity production becomes increasingly significant, which destabilizes the convective axial velocity w_b (Drazin & Reid, 2004).

Region III is characterized by the competition between the spiral convection rolls and the centrifugal instability typical of isothermal Taylor-Couette flow. In this region the stability is often described in terms of the dimensionless Richardson number or mixed convection parameter ($R_i = \frac{G}{Re_i^2}$) (Ball & Farouk, 1988, 1989), which measures the ratio between buoyancy and inertial forces. The Grashof number characterizing the onset of spiral vortices (G_c) and the critical spiral mode (n) progressively decrease as the rotation is increased, resulting in Taylor vortices for $R_i \approx 0.06$. The intersection between the transition curves for spiral flow SP and Taylor vortices TV is depicted in figure 5.1 (b). The (black) dashed-dotted line indicates the transition between both flow regimes after the basic flow is unstable. The value of R_i at which this transition occurs decreases with increasing Re_i, in contrast to the numerical results of Kuo & Ball (1997) in a finite-length system, in which it takes place at a constant R_i.

Secondary instabilities

The figure 5.2 illustrates the sequence of flow patterns found when $\mathrm{Re}_i = 50$ is fixed and G is increased (path A-A' in figure 5.1). Color maps of the temperature in longitudinal sections at $r = \frac{r_o+r_i}{2}$ (upper row) and horizontal sections at mid-height (lower row) are depicted. The axial non-dimensional length $L_z = \frac{2\pi}{k_z}$ of the computational domain is fixed with $k_z = 0.84$. The onset of instability occurs at $G_c \approx 1328$ resulting in a spiral flow pattern with azimuthal mode number $n = 2$. This state is stable only in the vicinity

of the critical point. A small increase in ΔT leads to the emergence of a new spiral state with $n = 3$ (see figure 5.2 (a)) which remains stable when $1500 \lesssim G \lesssim 3500$. A complex spatio-temporal dynamics takes place when G is further increased ($G > 3500$). First, pure spiral states turn into wavy spiral flow patterns like the ones illustrated in figures 5.2 (b) and (c), corresponding to $G = 4000$ and $G = 5000$ respectively. Note that the dominant spiral mode changes from $n = 3$ to $n = 2$ when G is increased, unlike the primary transition, where n gradually increases with G. The existence of wavy spiral flow has been reported in both experimental (Lepiller *et al.*, 2008) and numerical studies (Viazzo & Poncet, 2014) when considering apparatuses with large Γ and $\eta \sim 0.8$. Subsequently increasing G above the wavy spiral flow regime, the flow becomes completely irregular, as is shown in figure 5.2 (d).

The sequence of transitions that the flow undergoes when $G = 2000$ and Re_i is increased (path B-B' in figure 5.1) is shown in figure 5.3. The different states are illustrated through an isosurface of the axial velocity ($w = -20$). L_z is again fixed with $k_z = 0.84$. The primary instability happens at $\mathrm{Re}_i \approx 39$, leading to spiral flow with $n = 3$ (figure 5.3 (a)). With the increase of Re_i the axial force due to thermal buoyancy loses importance in favor of inertial forces, which results in secondary transitions towards spiral flow with decreasing azimuthal mode. The transition from $n = 3$ to $n = 2$ takes place at $\mathrm{Re}_i \approx 52$, whereas the subsequent transition to $n = 1$ occurs at $\mathrm{Re}_i \approx 135$. The ensuing flow patterns are reflected in figures 5.3 (b) and (c) respectively. Further increasing the rotation speed ($\mathrm{Re}_i \approx 260$) the flow becomes quasi-periodic due to the emergence of a low frequency modulation. The resulting state preserves the spiral structure with $n = 1$ and is characterized by the appearance of spatio-temporal defects. An example of these flow patterns in which the defect is localized on the bottom of the fluid domain is illustrated in figure 5.3 (d). Finally, a subsequent increase in Re_i results in the appearance of Taylor vortices (see figure 5.3 (e)), which occurs for $\mathrm{Re}_i \approx 280$.

5.4.2 Rigid flat end walls

Primary instability

Even for weak rotation, convection begins locally near the end walls due to the non-zero radial velocities. Thus, in contrast to the infinite case, the flow remains laminar in regions I and II. The onset of instability occurs in region III as a result of the competition between thermal buoyancy and inertial forces. The marginal curve ((blue) solid line in

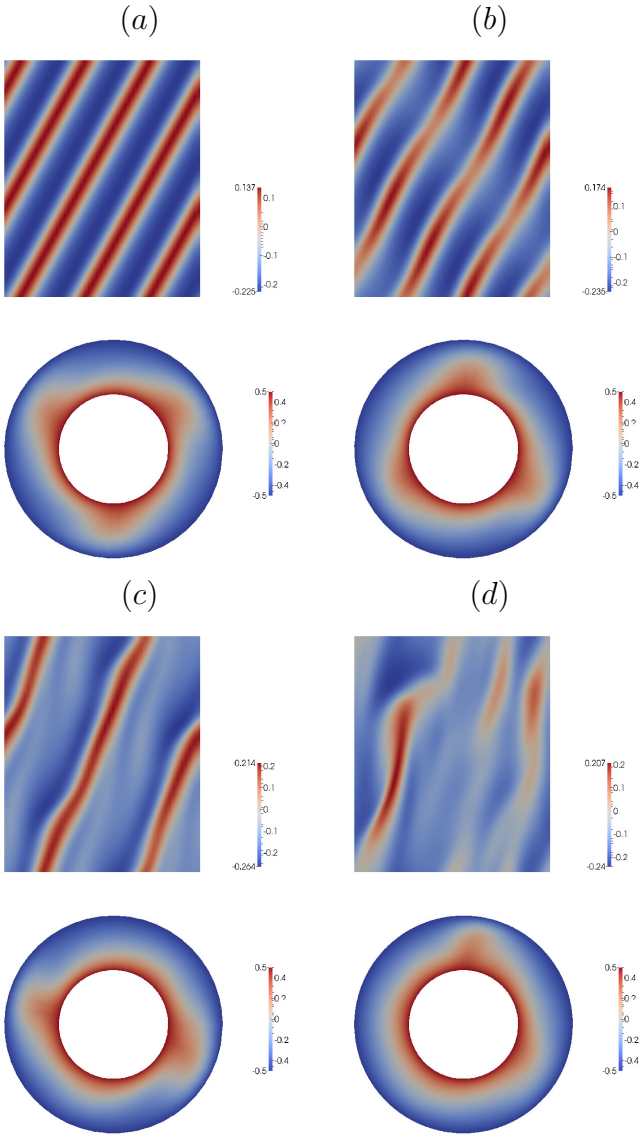

Figure 5.2: Color maps of the temperature in the case of infinite long cylinders with a rotating heated inner cylinder for $\mathrm{Re}_i = 50.0$, $\sigma = 0.71$, $\eta = 0.5$ and $k_z = 0.83$. Longitudinal sections (θ, z) at $r = \frac{r_o + r_i}{2}$ (upper row) and horizontal sections (r, θ) at $z = 0$ (lower row) are depicted in each case. (a) $G = 3000$, $n = 3$ spiral flow; (b) $G = 4000$, $n = 3$ wavy spiral flow; (c) $G = 5000$, $n = 2$ wavy spiral flow; (d) $G = 7000$, irregular flow.

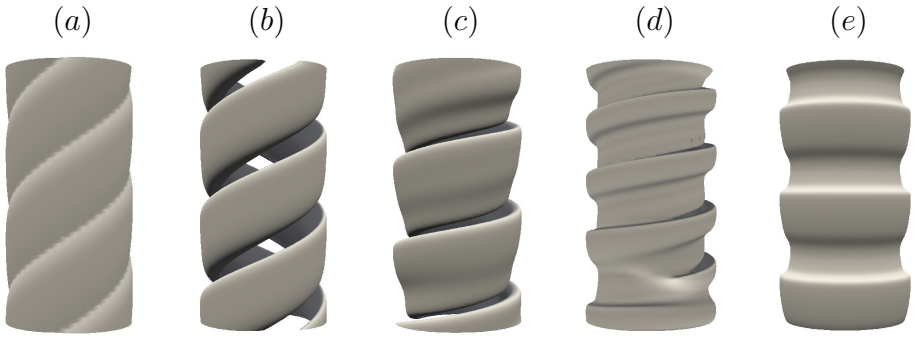

Figure 5.3: Evolution of an isosurface of the axial velocity $w = -20$ as Re_i is varied and $G = 2000$ in the infinite case. (a) $n = 3$ spiral flow pattern, $\mathrm{Re}_i = 50$; (b) $n = 2$ spiral flow pattern, $\mathrm{Re}_i = 70$; (c) $n = 1$ spiral flow pattern, $\mathrm{Re}_i = 100$; (d) $n = 1$ spiral flow pattern with defects, $\mathrm{Re}_i = 260$; (e) Taylor vortices, $\mathrm{Re}_i = 300$;

figure 5.1(a)) exhibits two turning points. The first one, $TP_1 \equiv R_i \approx 0.083$, is equivalent to the intersection point between spiral flow and Taylor vortices illustrated in figure 5.1 (b) for the infinite case, whereas the second one, $TP_2 \equiv R_i \approx 1.58$, only appears in the finite case and is thus directly related to the existence of axial end walls. In presence of weak radial heating the onset of Taylor vortices, which in the isothermal situation takes place at $\mathrm{Re}_i \approx 65$, is shifted towards larger values of Re_i up to reach TP_1. Above this point, laminar flow is destabilized in the region embraced between TP_1 and TP_2, so that spiral flow occurs for lower values of Re_i than Taylor vortices. This behavior is in agreement with the experiments of Snyder & Karlsson (1964) who used an apparatus with a very large aspect ratio. When G is increased above TP_2 the flow is stabilized, causing the reversal of the marginal curve towards larger Re_i. The critical azimuthal wavenumber of the spiral patterns increases with G.

Secondary instabilities

The figure 5.4 shows color maps of the temperature illustrating the sequence of states obtained when G is increased and $\mathrm{Re}_i = 50$ is fixed (path A-A' in figure 5.1). The non-axisymmetric flows are plotted in a longitudinal section at $r = \frac{r_o + r_i}{2}$ and a horizontal section at mid height, whereas the axisymmetric states are represented in a meridional section. The conductive basic flow (fig 5.4 (a)) remains stable up to reach $G_c \approx 2000$, where the instability sets in resulting in spiral flow (figures 5.4 (c) and (d)). The most unstable azimuthal mode near the lower critical boundary is $n = 3$, however, as the radial heating increases ($G \approx 5000$), the critical spiral mode changes to $n = 4$. The

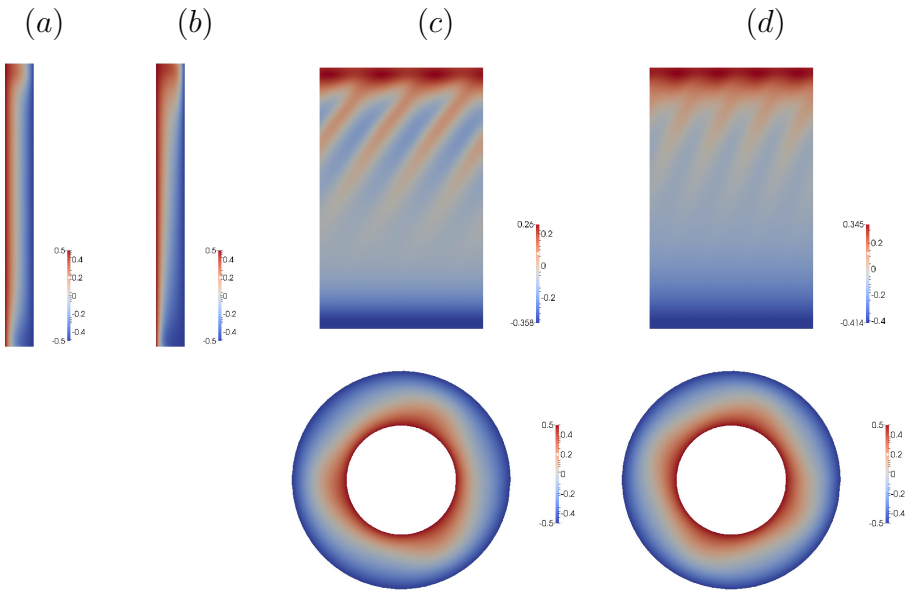

Figure 5.4: Temperature profiles in the finite case at $\mathrm{Re}_i = 50.0$, $\sigma = 0.71$, $\eta = 0.5$ and $\Gamma = 10$; Figures (a) and (b) correspond to axisymmetric states at $G = 2000.0$ and $G = 8000.0$. They are plotted in a meridional (r, z) section, where the inner cylinder is on the left hand side. Figures (c) and (d) display spiral flow in a longitudinal (θ, z) section at $r = \frac{r_o + r_i}{2}$ and in a horizontal section (r, θ) at mid-height, corresponding to (c) $G = 2500.0$, $n = 3$ and (d) $G = 5000.0$, $n = 4$.

increase of n with G was already described in Kuo & Ball (1997) and attributed to the stronger axial force acting on the fluid due to thermal buoyancy. Further increase in G leads to the upper stability boundary. Above this threshold, the spiral patterns settle down to the axisymmetric state shown in figure 5.4 (b), in which the thermal boundary layers at the sidewalls are thinner than in 5.4 (a) as a result of the stronger convective transport. This state is usually termed as convective basic flow (Ali & McFadden, 2005). The transition from spiral flow to this axisymmetric state as ΔT is increased was experimentally visualized by Ball & Farouk (1989) using an apparatus with $\Gamma = 31.5$.

The figure 5.5 illustrates the sequence of flow transitions when the thermal effects are weak ($G = 2000$) and Re_i is increased (path B-B' in figure 5.1). Similarly to figure 5.3, the evolution of an isosurface of the axial velocity ($w = -10$) is depicted. This bifurcation scenario with the precise geometry and working fluid considered here was reported by Kuo & Ball (1997). All transitions mentioned in Kuo & Ball (1997) have been reproduced here, however, we have found a notable difference in the onset of spiral flow, which occurs for lower Re_i in our simulations and corresponds to a critical spiral mode $n = 3$ instead of $n = 2$ in their simulations. The reason for this discrepancy is

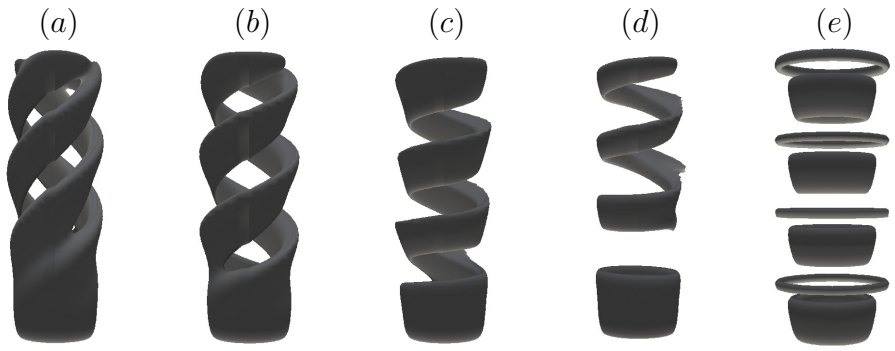

Figure 5.5: Evolution of an isosurface of the axial velocity $w = -10$ for $G = 2000$ as Re_i is varied in the finite case. (a) $n = 3$ spiral flow, $\mathrm{Re}_i = 60$; (b) $n = 2$ spiral flow , $\mathrm{Re}_i = 70$; (c) $n = 1$ spiral flow, $\mathrm{Re}_i = 90$; (d) $n = 1$ spiral flow with defects, $\mathrm{Re}_i = 110$; (e) Taylor vortices, $\mathrm{Re}_i = 140$.

explained by the assumption made by these authors that neglects the correction of the velocity field at each timestep. This correction is necessary to ensure that the solution of the discretized problem has zero divergence in the interior of the domain. Based on previous studies of similar flows they considered this term to be negligible. Under this assumption they stated that the onset of spiral flow does not depend on thermal buoyancy and occurs at a fixed critical Reynolds Re_c, slightly lower than Re_c in the isothermal situation. As we adopt the same hypothesis in our simulations the same results as in Kuo & Ball (1997) are recovered and the primary transition is missed. The correction of the velocity field is therefore essential to properly predict the onset of instability in this problem. Nevertheless its relevance diminishes as increasing Re_i and the secondary transitions coincide with those in Kuo & Ball (1997).

The same sequence of flow states as in figure 5.3 has been obtained, differing only in the values at which the transitions take place. The basic flow loses stability to spiral flow with $n = 3$ for $\mathrm{Re}_i \approx 50$ (figure 5.5 (a)). Further increasing Re_i results in spiral flow patterns with decreasing n. The transitions to $n = 2$ (figure 5.5 (b)) and $n = 1$ (figure 5.5 (c)) occur for $\mathrm{Re}_i \approx 63$ and $\mathrm{Re}_i \approx 90$ respectively. The transition between spiral flow and Taylor vortices is also characterized by the presence of defects. Nevertheless, these are much more pronounced than in the infinite cylinders case, as can be seen in figure 5.5 (d). The onset of Taylor vortices, which are illustrated figure 5.5 (e), takes place for $\mathrm{Re}_i \approx 130$.

5.4.3 Convective heat transport rate

In this section we show the variation of the averaged Nusselt number (Nu) along the inner cylinder when the control parameters are varied for the two systems considered in this study. This dimensionless number measures the relationship between total and conductive heat transfer across a surface and is commonly used to characterize the intensity of convective heat transport in engineering applications. The Nusselt number along the inner cylinder can be mathematically expressed as

$$< Nu_i >_t = \frac{\int_0^{2\pi} \int_{-\Gamma/2}^{\Gamma/2} \partial_r T|_{r_i} \mathrm{d}z\mathrm{d}\theta}{q_{cond}} \tag{5.3}$$

where $< . >_t$ indicates time average and $q_{cond} = 2\pi\kappa\Delta T/ln(\eta)$ denotes the dimensionless conductive heat flux. To simplify the notation the subindex i is omitted henceforth. Note that the Nusselt number along the outer cylinder Nu_o can be easily obtained from a simple heat balance as $Nu_o = Nu_i\eta$.

In figure 5.6 (a) the evolution of Nu with Re_i in the finite and infinite cases is compared when $G = 2000$. It is observed that heat transfer is in both cases independent of rotation as long as the basic laminar flow is stable ($\mathrm{Re}_i \lesssim 50$). In the infinite case heat transfer is purely conductive ($Nu = 1$), whereas in the finite case, Nu is slightly higher ($Nu = 1.07$) due to the heat transfer through the Ekman boundary layers. The onset of instability enhances the convective heat transport so that Nu increases significantly as increasing Re_i. The scaling behavior is nearly identical in both cases. It can be described by a power law relationship of the type $Nu = A\mathrm{Re}_i^B$, in which the same coefficient $A = 0.15$ is obtained in both cases and the exponent only differs marginally, $B = 0.49$ and $B = 0.50$, in the finite and infinite cases respectively.

Most experiments intended for developing heat transfer correlations operate in forced convection regime, so that the effect of free convection in heat transfer has received little attention (Fenot *et al.*, 2011). In order to fill this gap, in figure 5.6 (b) we show the evolution of Nu with G in the finite and infinite cases for several values of Re_i near the onset of instability, where thermal buoyancy effects prevail over centrifugal forces. The different dynamical behaviors arising between finite and infinite systems as increasing G are clearly reflected in the convective heat transfer rate. Obviously, the largest differences occur for $\mathrm{Re}_i = 20$, which corresponds to the first region of figure 5.1 (a). In the infinite case (circles), $Nu = 1$ remains constant up to $G \approx 11000$, indicating that heat transport is exclusively conductive up to reach the onset of instability. In contrast, in

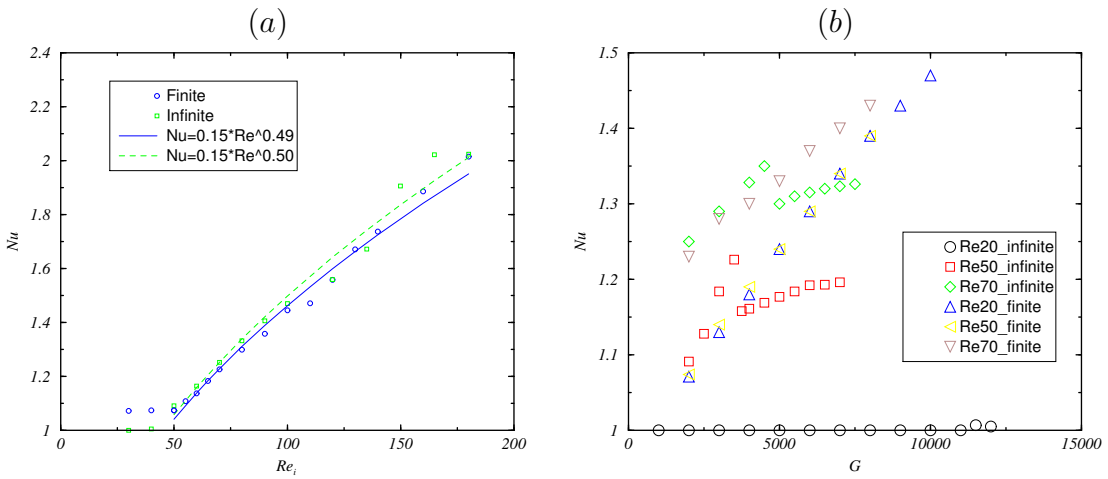

Figure 5.6: Variation of the averaged Nusselt number (Nu) along the inner cylinder in the case of finite and infinite cylinders plotted agains (a) Reynolds number Re_i, for $G = 2000$; (b) Grashof G, for several values of Re_i.

the finite case (up triangles), the secondary circulation provides an efficient mechanism to transfer heat, which results in an almost linear increase of Nu with G. Such linear growth remains in the region of spiral flow, $\mathrm{Re}_i = 50$ (left triangles) and $\mathrm{Re}_i = 70$ (down triangles), nevertheless the slope diminishes as Re_i is increased. As formerly mentioned Nu increases with Re_i after the basic flow becomes unstable. However, the values of Nu corresponding to different values of Re_i approach each other as G increases. When G exceeds the value corresponding to the upper part of the marginal curve in figure 5.1 (a) the flow becomes again axisymmetric and Nu solely depends on G. As a result, curves corresponding to different values of Re_i collapse, as can be seen for $\mathrm{Re}_i = 20$ and $\mathrm{Re}_i = 50$ when $G > 6000$. In the infinite case, the behavior of Nu within the region of spiral flow, $\mathrm{Re} = 50$ (squares) and $\mathrm{Re} = 70$ (diamonds), reflects the transitions described in 5.4.1. The spiral flow ($G < 3500 - 4000$) resulting from the primary transition is an excellent heat transfer mechanism, leading to a rapid and linear growth of Nu as G is increased. In this flow regime the values of Nu in the infinite case are slightly larger than those in the finite case. The transition towards wavy spiral flow results in a sudden decrease of the convective heat transport, consistently with the results of Kedia *et al.* (1998). After this initial drop, further increasing G towards fully developed turbulent flow is accompanied by a progressive growth in Nu, which is however significantly lower than the linear growth in the spiral flow regime. Once the instability of the basic flow has occurred Nu increases with Re independently of G.

5.4.4 Comparison of the dynamical behavior of the two systems

The presence of Ekman boundary layers delays the onset of instability with respect to that in the case of infinite long cylinders, with the exception of the transition to Taylor vortices, which happens for slightly larger values of Re_i in the infinite case. Hot rising and cold descending fluid are radially transported through the Ekman layers at the top and bottom lids respectively. This produces a stable axial temperature gradient, and consequently, a buoyancy force is generated that opposes the convective vertical motion. This stabilizing force becomes increasingly important as the thermal effects gain relevance and, for sufficiently large values of G, results in entirely horizontal motion, suppressing the baroclinic vorticity production. The Ekman layer also acts as a frictional layer, slowing down the internal flow and causing the marginal curve to shift towards larger values of Re_i than in the infinite case.

For low G, stratification and frictional effects are still weak so that both systems share the same fundamental dynamics. The marginal curves show a good qualitatively agreement and the same sequence of flow patterns is found in both cases when $G = 2000$ and Re_i is varied, differing only in the values at which the transitions occur. The stabilizing effect due to the aforementioned mechanisms causes the primary and first secondary transitions to occur for slightly larger values of Re_i in the finite case. Nevertheless, as the rotation is increased, the onset of the remaining secondary instabilities is favored by the presence of axial end walls, taking place at considerably lower values of Re_i in the finite case.

The discrepancies between the marginal curves in both systems grow very substantially as G is increased. In the finite case, the size of the fluid regions in which vertical motion is inhibited increases as the axial stratification becomes stronger, thereby reducing the region of the fluid domain where spiral flow occurs (see figures 5.4 (c) and (d)). The radial circulation, which is significantly intensified with the increase of G, extends over the former regions (see figure 5.7) and results in an increase of the friction with the internal flow, which leads to substantial differences with the onset of instability in the infinite case. When G is increased above the second turning point TP_2, the flow is strongly stabilized and the marginal curve bends towards larger Re_i. This means that, as increasing G from the spiral flow regime, there exist a threshold from which the baroclinic vorticity production cannot overcome the damping provided by stable density stratification and frictional effects. The formation of spiral flow is therefore inhibited and the flow returns to the axisymmetric state.

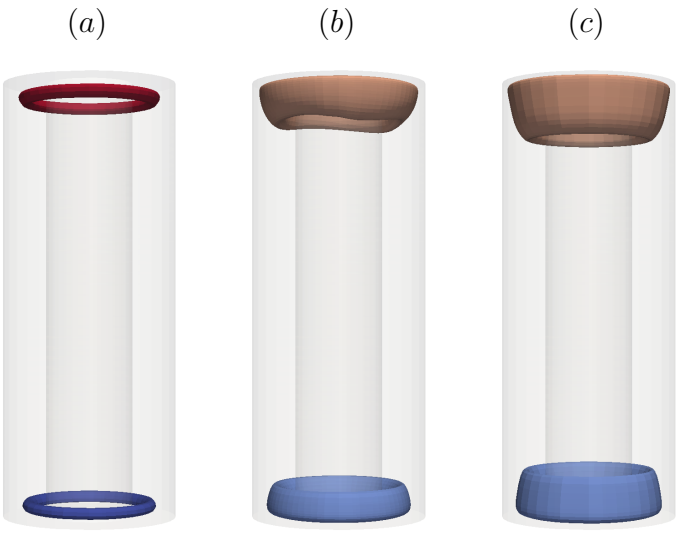

Figure 5.7: Isosurfaces of the radial velocity $u = -6$ (blue) and $u = 7$ (red) in the finite case. (a) $G = 2000$, (b) $G = 5000$ and (c) $G = 8000$

In the infinite cylinders case, the absence of meridional circulation results in an additional mechanism of instability which occurs for very weak rotation speeds and involves the onset of convective heat transport in the system. The onset of spiral flow is accompanied by an abrupt drop of the marginal curve. This is a robust feature in the case of axially periodic boundary conditions, which has been found either changing the boundary conditions (relative rotation between the cylinders or sense of the temperature gradient) or the parameters of the system (η and σ). Despite the difference in geometry it is reminiscent of the destabilization of the free convective flow by weak rotation observed in the Czochralski model (Gelfgat, 2011). When G is increased, the flow undergoes the classical Ruelle-Takens route to chaos, in which the spiral flow bifurcates first in wavy spiral flow and becomes subsequently irregular.

The σ effect described in 5.2.2 is negligible ($\sigma \approx 1$), so the differences between the finite and infinite cases can be exclusively ascribed to the role played by the Ekman layers.

5.5 Solid-body rotation with cooled inner cylinder

We consider now the stability of fluid heated at the outer cylinder and cooled at the inner cylinder. The entire system rotates uniformly at a constant angular speed Ω. This is the typical experimental setup to study baroclinic instability in an atmospheric

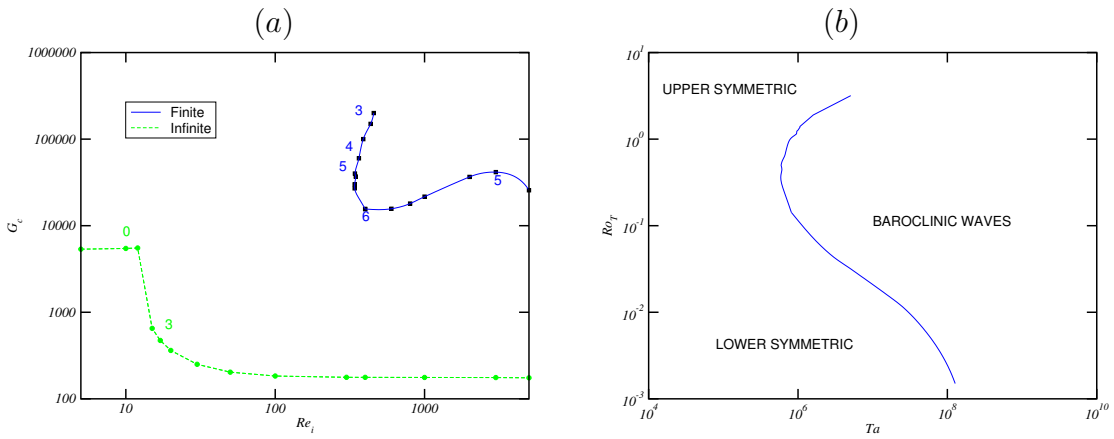

Figure 5.8: (a) Critical stability curve in the case of solid-body rotation with cooled inner cylinder. The numbers that appear on top of the critical curves are the azimuthal modes associated to the critical perturbations. (Blue) Solid line and squares are used for the finite cylinder case, whereas (green) dashed line and circles stand for the marginal stability in the infinite cylinders case. The working fluid is water($\sigma = 7.16$) and the geometric parameters are $\eta = 0.47$ and $\Gamma = 1.86$ (in the finite case). Note that the ordinate axis is logarithmic in this case. (b) Marginal curve for the case of finite cylinders plotted in a log-log Ta-Ro_T diagram, as it is typically found in the context of geophysical fluids.

context. Since the atmosphere's vertical extension is much smaller than the radial one, experiments are generally carried out in shallow annular containers ($\Gamma \sim O(1)$) which entails a significant influence of the axial end walls in the dynamics. For the study presented here, we have considered the experimental setup used by Koschmieder (1972), where the geometry is defined by $\eta = 0.47$ and $\Gamma = 1.86$, and the working fluid is water ($\sigma = 7.16$).

The figure 5.8 (a) shows the critical boundaries in the finite (solid line) and infinite (dashed line) cases. The short aspect ratio results in a basic state with a completely different axial velocity profile, which leads to extremely large differences (three orders of magnitude) between the marginal curves in both cases.

5.5.1 Rigid flat end walls

Basic flow

The axial velocity w_b is confined to the cylinders, forming the so-called Stewartson layers (see figure 5.9 (a)). They consist of two opposite vertical circulations near each cylinder

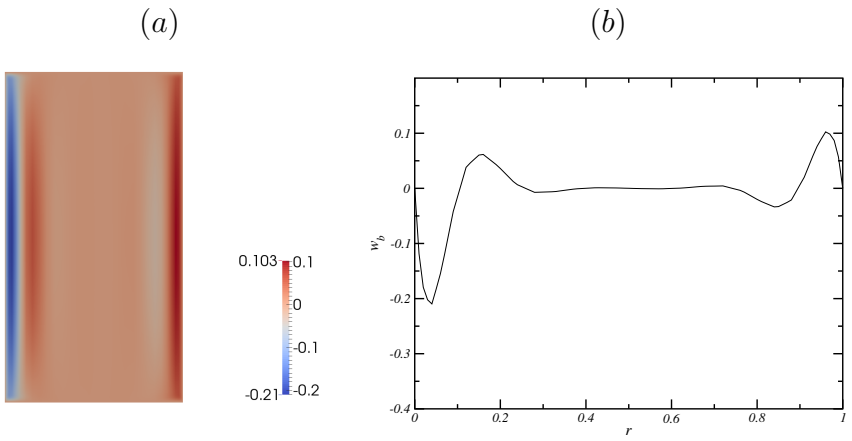

Figure 5.9: (a) Axial velocity of the basic state in the finite case plotted in a meridional plane for $\mathrm{Re}_i = 5000$, $G = 10000$, $\Gamma = 1.86$, $\eta = 0.47$ and $\sigma = 7.16$. The inner cylinder is on the left hand side. (b) Radial dependence of w_b at mid-height for the same parameters as in (a).

which perform different dynamical roles. The inner layer fits the azimuthal velocity to the sidewall velocity, whereas the outer layer adjusts the radial and axial velocities to satisfy the no-slip condition at the sidewall. Moreover, the outer layer is also responsible for the vertical flux between the Ekman layers, creating an overturning circulation which mimics the tropical atmospheric circulation, known as Hadley cell, and is thus essential to study baroclinic instability in this context. The dimensionless thickness of the inner and outer layers is usually expressed in terms of the Ekman number ($E = \frac{\nu}{\Omega r^2}$) , being the outer layer ($\delta \sim E^{1/3}$) narrower than the inner one ($\delta \sim E^{1/4}$). The Stewartson layers are thicker than the Ekman layers resulting at the horizontal end walls ($\delta \sim E^{1/2}$). The outer circulation is much more intense than the inner one, as is reflected in 5.9 (b), where the radial dependence of w_b at mid-height is shown for $\mathrm{Re}_i = 5000$ and $G = 10000$. We refer to Greenspan (1968) for an exhaustive treatment of the Stewartson layers. Due to the lateral confinement of w_b the basic flow splits into two parts, a roughly azimuthal inner flow and the meridional overturning circulation created by the radial and axial velocities near the boundaries.

Onset of instability and baroclinic waves

In an atmospheric context the stability boundaries are usually plotted in a logarithmic $Ta - Ro_T$ diagram, where $Ta = \frac{4\Omega^2 d^4}{\nu^2}$ and $Ro_T = \frac{4G\Gamma}{Ta}$ are the dimensionless Taylor and thermal Rossby numbers respectively. Note that Ro_T depends on Γ and thus is infinite in the axially periodic case, which is the reason for choosing G for the comparison between

the finite and infinite cases. In this parameter space, the onset of baroclinic waves (see figure 5.8 (b)) displays the typical anvil shape which has been extensively reported in the literature (see i.e. Hide (1958); Lewis & Nagata (2004)). It is characterized by the existence of an inflexion point that connects two instability branches, commonly known as upper and lower symmetric transitions. The latter indicates the onset of instability when the temperature profile of the basic state is essentially conductive (small ΔT) and progressively decreases towards smaller Ro_T as Ta is increased. As pointed out in Lewis & Nagata (2004) and Koschmieder (1972), for high rotational speeds, a significant destabilizing effect is induced by the centrifugal force, changing the concavity of the lower transition curve. The upper transition occurs for large ΔT, when the effects of the stable stratification become strong and higher rotational speeds are required for the onset of baroclinic waves. The critical azimuthal wavenumber n associated with the baroclinic waves is shown on top of the (blue) solid line in figure 5.8 (a). It is observed that n decreases along the upper and lower transitions, existing a local maximum $n = 6$ in the region near the inflexion point. This behavior is in full agreement with the results of the linear stability analysis reported in Lewis & Nagata (2004). Figure 5.10 illustrates in a horizontal section at mid-height the temperature profiles of two baroclinic waves obtained when $\mathrm{Re}_i = 1000$ is fixed and G is varied. As G is increased from the lower to the upper transition, the azimuthal wavenumber of the wavy patterns progressively decreases from $n = 6$ at the onset of instability up to $n = 2$ near the upper transition curve. Further increase in G leads to axisymmetric flow patterns with a stably stratified temperature profile, which are characteristic of the upper symmetric region. When ΔT is fixed and the rotation is increased, baroclinic waves often exhibit amplitude vacillations which usually occur before the transition towards a new state with lower n takes place. Nevertheless, in the parameter range studied here, the same azimuthal wavenumber remains when Re_i is increased, and therefore, only steady waves with a single frequency have been found.

5.5.2 Axially periodic boundary conditions

Basic flow

The basic flow under the assumption of axial periodicity was generally described in section 2.4.1. Here attention is paid to the axial velocity profile and the differences existing with the finite case. The axial velocity w_b consists of two fluid cells that fill the entire domain. The fluid rises (descends) within the outer (inner) cell reproducing an infinite

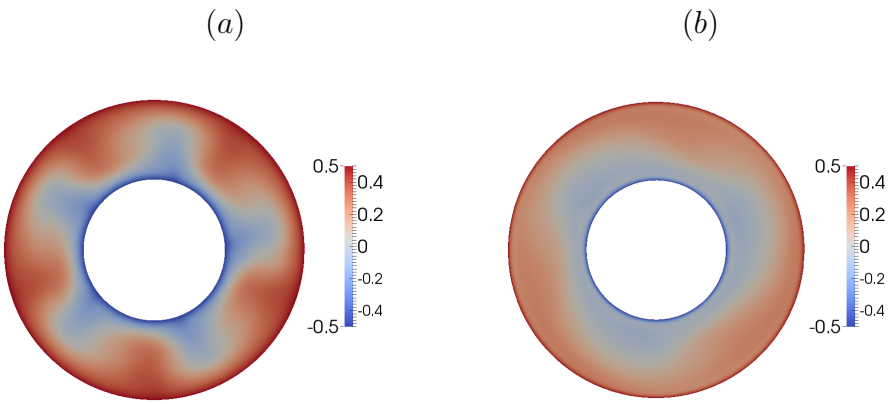

Figure 5.10: Baroclinic waves in the finite case. Color map of the temperature in a horizontal section at mid-height for $\mathrm{Re}_i = 1000$ and (a) $G = 8 \times 10^5$ and $n = 5$; (b) $G = 1.6 \times 10^6$ and $n = 3$.

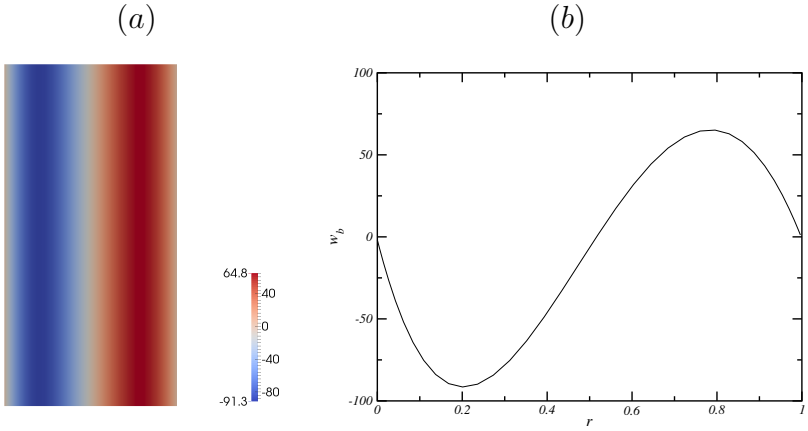

Figure 5.11: (a) Axial velocity w_b of the infinite case plotted in a meridional section for $\mathrm{Re}_i = 5000.0$, $G = 10000.0$, $\eta = 0.47$ and $\sigma = 7.16$. The inner cylinder is on the left hand side. (b) Radial dependence of w_b for the same parameters as in (a).

convective loop (see figure 5.11 (a)). The enormous qualitative and quantitative differences between w_b in the finite and infinite cases can be easily seen when comparing the radial dependence in each case (see figures 5.9 (b) and 5.11 (b) for the finite and infinite cases respectively). In the case infinite, w_b only has radial dependence and its highest absolute values are approximately in the middle of each cell, at a distance $r \approx \frac{r_o - r_i}{4}$ from the cylinders. In contrast, the largest values of w_b in the finite case are located near the cylinders and are two orders of magnitude lower than those in the infinite case.

Onset of instability and baroclinic waves

As long as rotation is weak, the marginal curve ((green) dashed line in figure 5.8 (a)) shows the same dynamical features as in section 5.4 ((green) dashed line in figure 5.1 (a)). The onset of convection through axisymmetric convection rolls occurs at a nearly constant value, $G_c \approx 5319$, and when $\mathrm{Re}_i = 13$ is reached, the marginal curve exhibits a steep decrease which means the transition to the baroclinic waves regime.

The onset of baroclinic waves slightly decreases with Re_i and, similarly to the finite case, is destabilized due to centrifugal buoyancy. However, for the values of Re_i shown in figure 5.8 (a), this destabilizing effect is still weak, and thus the change is not apparent. To illustrate the influence of centrifugal buoyancy in the case of infinite long cylinders, figure 5.12 shows the critical boundaries corresponding to three different situations for larger values of Re_i. The (blue) solid and (black) dashed-dotted lines are the marginal curves for systems with a positive temperature gradient (heated outer cylinder and cooled inner cylinder) with and without considering the centrifugal term respectively, whereas the (green) dashed line is the marginal curve for a system with a negative temperature gradient (cooled outer cylinder and heated inner cylinder). The centrifugal term plays a crucial dynamical role as Re_i is increased. If it is switched off, the onset of instability becomes independent of Ω. In contrast, when it is considered, the flow is destabilized (stabilized) by a positive (negative) temperature gradient. The critical azimuthal wavenumber also depends on the sense of the temperature gradient, increasing (decreasing) with Re_i in a system with a positive (negative) temperature gradient. These results qualitatively agree with the experiments conducted by Koschmieder (1972), using the same fluid and radius ratio. However, the values of Re_i for which the marginal curves corresponding to positive and negative temperature gradients depart from each other in Koschmieder (1972) are much lower than in the infinite case, which points to the large centrifugal effects due to the secondary radial circulation.

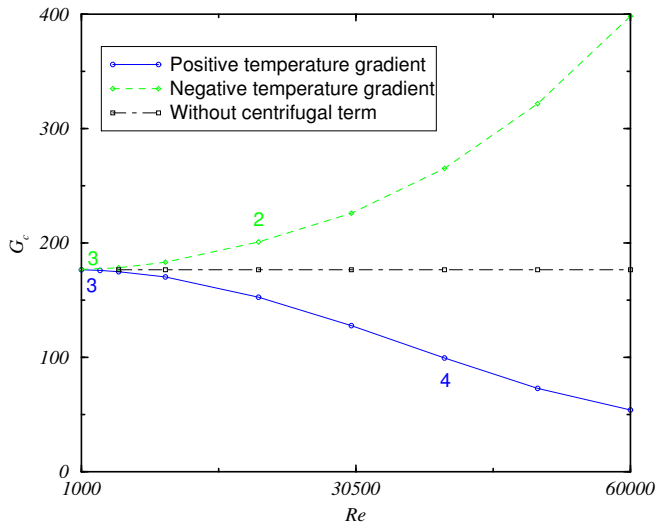

Figure 5.12: Influence of the centrifugal force in the infinite case. The (blue) solid line represents the critical boundary when the system is heated from the outer cylinder (positive temperature gradient), the (green) dashed line is the critical boundary when the system is heated from the inner cylinder(negative temperature gradient) and the (black) dashed-dotted line stands for the marginal curve in a system with positive temperature gradient when the centrifugal term is neglected.

The axial wavenumber k_c of the critical disturbances is approximately zero ($k_c \sim O(10^{-4})$). Consequently, the flow becomes quasi two dimensional, as expected from the Taylor-Proudman theorem. Figure 5.13 shows the temperature profiles corresponding to the sequence of states obtained for fixed $k_z = 4.5\times10^{-2}$ and $\mathrm{Re}_i = 1000$ when G is increased. The azimuthal wavenumber of the resulting flow patterns gradually decreases from $n = 3$ at the onset of instability ($G = 177$) up to $n = 1$ ($G \approx 4000$). Subsequently increasing G random fluctuations come to progressively dominate the flow, which becomes fully irregular for $G \approx 6000$.

5.5.3 Influence of the aspect ratio

To elucidate how the length of the apparatus affects the stability of the basic flow, we have computed the critical boundary (G_c) as the aspect ratio Γ is increased and $Re_i = 1000$ is fixed (see figure 5.14 (a)). As increasing Γ, the basic flow must approach that in the infinite case, so the instability should ultimately occur at the same values in both cases. This hypothesis is consistent with the exponential decay of G_c when Γ is increased from $\Gamma = 1.86$ up to $\Gamma \approx 12$ (see inset in figure 5.14 (a)). The gradual

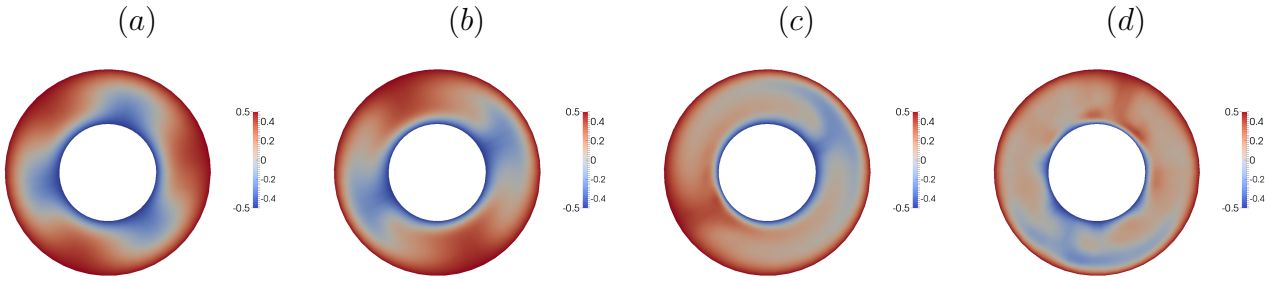

Figure 5.13: Sequence of states obtained in the infinite case for $\mathrm{Re}_i = 1000$ and $k_z = 4.5 \times 10^{-2}$ as G is increased. (a) Baroclinic wave with $n = 3$ for $G = 250$, (b) Baroclinic wave with $n = 2$ for $G = 600$, (c) Baroclinic wave with $n = 1$ for $G = 5550$ and (d) Irregular flow for $G = 7500$.

approximation between both basic flows is also reflected in figure 5.14 (b), where the radial dependence of w_b is plotted at mid-height for several values of Γ and $G = 10000$. It is observed that the maximum and minimum values of w_b grow almost linearly as Γ is increased and progressively approach w_b in the infinite case, which is depicted in figure 5.11 (b) for the same G. Nevertheless, for $\Gamma = 20$, w_b is still far from that in the infinite case. From linear extrapolation of the maximum absolute values, it is estimated that a very tall apparatus ($\Gamma = 204.934$) would be required to achieve the value of w_b corresponding to the infinite case. It should be underlined, though, that this is a rough estimate as w_b has axial dependence, and thus the maximum absolute value will change with z. The exponential decrease of G_c ceases for $\Gamma > 12$, resulting in a slight growth of the marginal curve with increasing Γ. This behavior remains until a turning point is reached at $(\Gamma, G) \approx (19.6, 10000)$, and the marginal curve changes direction towards larger values of G. The mechanism causing this reversal will be discussed in the following subsection. From $\Gamma > 19.6$ up to $\Gamma = 60$, which is the last value considered in this study, the axisymmetric flow remains stable. However, it is reasonable to expect that a new transition, leading to the instability taking place in the infinite case, will occur with further increase in Γ.

5.5.4 Comparison of the dynamical behavior of the two systems

The dynamics of the finite and infinite cases is profoundly modified by the different axial velocity profile w_b in each case. In the finite case, the strong viscous damping due to the boundary layers is reflected in a vast shift of the marginal curve towards larger values of

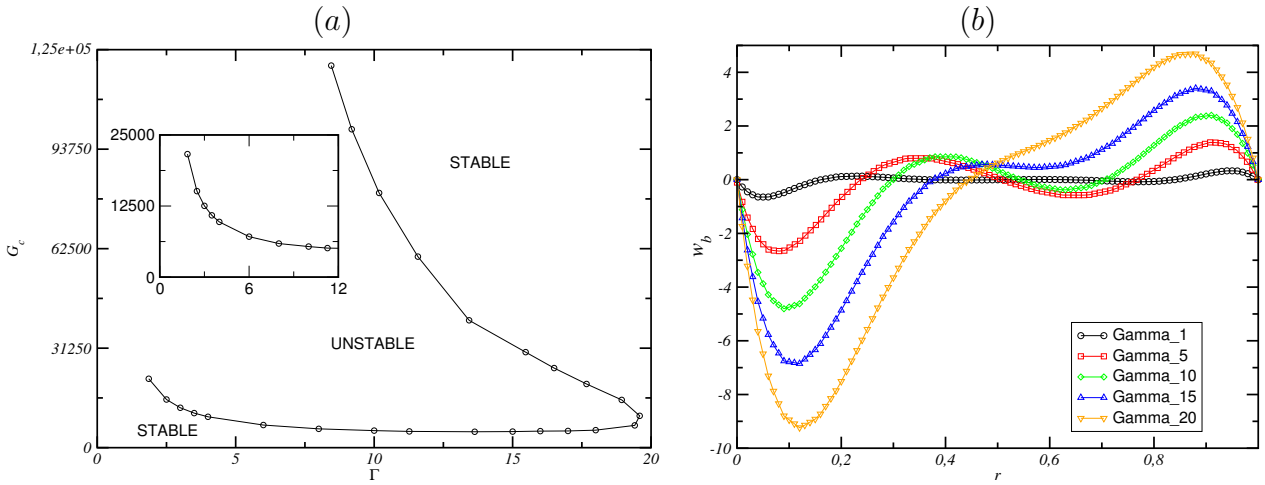

Figure 5.14: (a) Evolution of the critical Grashof number G_c as increasing the aspect ratio Γ. (b) Axial velocity w_b as a function of the radial coordinate r, at mid height $(z = 0)$, for $G = 10000$ and several values of Γ. In (a) and (b), $\mathrm{Re}_i = 1000$, $\eta = 0.47$ and $\sigma = 7.16$.

the control parameters (Re_i and G). The basic state loses stability to steady baroclinic waves, characterized by the presence of a unique phase velocity, which is commonly known as drift frequency. The azimuthal wavenumber is maximum near the turning point and decreases along the upper and lower transition curves. When Re_i is fixed and G is increased from the lower transition curve, the azimuthal wavenumber of the resulting baroclinic waves progressively decreases until the flow becomes axisymmetric above the upper transition curve. As in section 5.4, the temperature difference between the Ekman layers results in a stable vertical density gradient which plays an essential role in stabilizing the flow for large values of G. Above a certain threshold (upper transition branch), this stabilizing effect is strong enough to prevent the occurrence of baroclinic waves. Consequently, the flow returns to an axisymmetric state which is usually termed as convective basic flow. In the infinite case, despite the quantitative differences in w_b and the frictional effects, baroclinic waves of a similar nature as in the finite case are obtained. This is not surprising since, as pointed out by Williams & Robinson (1974), the Ekman layers friction and stable density stratification in a baroclinic annulus only introduce alterations in the form of the baroclinic waves, which are essentially Eady-like waves. For fixed rotation the azimuthal wavenumber decreases with the increase of G. Nevertheless, unlike the finite case, the flow becomes eventually irregular because of the lack of stabilizing mechanisms in this case. For weak rotation the same dynamical behavior as in section 5.4 is observed. The critical value G_c for the onset of convection in the non-rotating case remains nearly constant as Re_i is increased. Beyond a certain crit-

ical rotation Re_{i_c}, the marginal curve experiences a strong destabilization which involves the transition from the initial pure convective instability to the baroclinic instability. As was mentioned in 5.4, this behavior is inherent to radially heated systems under axially periodic boundary conditions.

As the aspect ratio Γ is increased, one expects the same instability to occur in the finite and infinite cases. Initially, there is an exponential decay of G_c, which progressively approaches the critical value in the infinite case. Nevertheless, as is illustrated in figure 5.14 (b), increasing Γ is accompanied by a substantial growth of the axial velocity w_b which intensifies the meridional overturning circulation. The resulting friction becomes increasingly important and results in stabilizing G_c, eventually causing the reversal of the critical boundary. When Γ is beyond the turning point, the rotational speed is insufficient to overcome the viscous damping due to the boundary layers, therefore baroclinic waves disappear and the axisymmetric flow reestablishes. Although the axisymmetric flow remains stable for the highest value of Γ simulated in this study, a transition to the instability taking place in the infinite case is likely to occur for larger values of Γ than those considered here. Lateral friction is systematically neglected in analytical and numerical models of the baroclinic annulus, which replace the no-slip boundary condition at the sidewall with a free-slip boundary condition. However, this assumption was refuted in Mundt *et al.* (1995), where the dynamical behavior was found to largely depend on the lateral boundary condition. More recently, Williams *et al.* (2010), based on torque-balance considerations, argued that the Stewartson layers drag is of the same order as the Ekman friction. They stated that although shear stresses due to Stewartson layers are lower than those for the Ekman layers, the area where the forces act is larger in the former, and therefore, similar torques result in both cases. In the case presented here, the torque in the cylinders gradually increases with Γ, which suggests that the Stewartson layers play a crucial role in damping the instability.

Finally, we also want to mention the influence of σ in the basic flow. As described in 5.2.2, the basic flow in the infinite case is independent of σ, what could eventually become a source of discrepancies between simulations in finite and infinite systems. In order to discern how σ affects the basic flow in the finite case, we have computed several basic flows for $G = 10000$, $\mathrm{Re}_i = 1000, 3000$ and 5000, and $\sigma = 0.71, 7.16$ and 24. We have observed that the basic flow is only slightly modified for $\mathrm{Re}_i = 1000$ and remains unchanged for $\mathrm{Re}_i = 3000$ and 5000. It is therefore concluded that the discrepancies between the finite and infinite cases are solely due to the boundary layer effect described along this section.

5.6 Conclusion

The influence of axial end walls in the stability of baroclinic flows has been investigated by comparing the linear stability of the flow in a laterally heated differentially rotating annulus when considering axial periodicity and rigid flat axial boundaries. The aim of this study is to discern the extent to which simulations in axially periodic systems (with lower computational cost) can be used to reproduce experimental results, and conversely, how far axial end walls can modify the dynamics of axially unbounded flows.

First, we have considered a system of moderate aspect ratio $\Gamma = 10$ (in the finite case) and wide gap $\eta = 0.5$, with a heated rotating inner cylinder, which is typically used to study baroclinic instabilities in industrial flows. Air ($\sigma = 0.71$) has been chosen as the working fluid. The onset of spiral flow is stabilized in presence of axial end walls. When the temperature difference between the cylinders is small, finite and infinite systems display similar dynamics, differing only in the values at which the transitions take place. With the increase of heat input, the Ekman layers friction increases and slows down the inner flow, leading to the progressive stabilization of the marginal curve. For sufficiently large G, spiral flow is suppressed as a result of strong vertical stratification, resulting in axisymmetric flow patterns. In the infinite case, owing to the lack of stabilizing mechanisms, the flow undergoes a sequence of bifurcations as G is increased, which results eventually in turbulent flow.

The rate of heat convective transport is closely related to the dynamical regimes that arise in each system. In the finite case, the Ekman layers provide an effective mechanism of convective heat transfer which operate even for laminar flow. These are enhanced as G increases, which results in a nearly linear growth of Nu. The onset of instability does not modify the linear scaling of Nu with G, but the slope decreases as rotation is increased. In the infinite case, the heat transfer rate due to spiral flow is much higher than that for the convection rolls arising for weak rotation and large G. As G is increased from the spiral flow regime, the transition between pure and wavy spiral flow patterns leads to a significant reduction of Nu, which subsequently increases with G as the flow becomes irregular. When the effect of thermal buoyancy is weak and both systems display the same dynamics, Nu varies with Re_i as a power law which is nearly the same in both cases ($Nu = 0.15\mathrm{Re}_i^{0.5}$). A great number of Nusselt correlations based on a non-dimensional power law have been suggested in the literature (Fenot *et al.*, 2011; Ball *et al.*, 1989). Nevertheless, there exist important discrepancies between some of them and further comparison with numerical results can assist in detecting the sources of these differences. The exponent of the correlation obtained in this study ($B \approx 0.5$) is the same

as in the analytical correlation provided by Dorfman (1963) for laminar flow. A similar exponent ($B = 0.47$) has also been found by Viazzo & Poncet (2014) who numerically explored a similar region of parameter space to that considered in figure 5.6 (a), using an apparatus with a different geometry ($\eta = 0.8$ and $\Gamma = 80$). The experimental correlation of Bjorklund & Kays (1959), which can be written as $Nu = 0.10\mathrm{Re}_i^{0.5}$ when their data are averaged, is also in very good agreement with our results. These authors did not observed any change in the heat transfer rate when the radius ratio was varied between $0.8026 \leq \eta \leq 0.9488$. Taken together, these results suggest that, as long as ΔT is small and the rotation speed is not enough to trigger turbulence, convective heat transfer does not depend on the geometry of the apparatus. Moreover, since the specific features of the flow patterns vary significantly from wide to narrow gap apparatuses, it is tempting to state that secondary instabilities resulting in pre-turbulent flow patterns do not alter the mechanisms of heat transfer. Nevertheless, such conclusions are in disagreement with the experiments of Ball *et al.* (1989), who found that the exponent of the power law relationship increases as the gap size is reduced. In addition, for the three values of the radius ratio considered by these authors ($\eta = 0437, 0.565$ and 0.656), the exponent is well below 0.5 ($B = 0.17, 0.30$ and 0.36). The exponent of the correlation experimentally determined by Gazley (1958) ($B = 0.8$), using an apparatus with a very narrow gap ($\eta = 0.99$), is also consistent with the trend observed in Ball *et al.* (1989). Since all aforementioned studies were performed for the same range of parameters, it is difficult to suggest a reason for such discrepancies. A numerical study that considers the influence of the radius ratio in the convective heat transport would therefore be necessary to clarify this issue.

Second, we have considered the flow in an atmospheric context where the container is rotating as a solid-body and heated from the outer cylinder. In this case the system has a short aspect ratio ($\Gamma = 1.86$, in the finite case) and wide gap ($\eta = 0.47$), and the working fluid is water ($\sigma = 7.16$). The presence of axial end walls substantially modifies the basic flow, so the onset of instability is entirely different in both cases. In the finite case, the axial velocity is confined to the sidewall, creating a meridional overturning circulation along the lateral and vertical boundaries. Similarly to the previous setup, friction between boundary layers and internal flow results in strong flow stabilization. As the meridional circulation is enhanced, either increasing G or Γ, there exist a threshold above which baroclinic vorticity production is not enough to overwhelm the damping effects and the flow becomes again axisymmetric. In the infinite case, the baroclinic waves ensuing from the primary transition are quasi-two dimensional. When G is increased the flow exhibits a sequence of transitions towards baroclinic waves with

decreasing azimuthal wavenumber n and becomes finally irregular.

Note that the basic flow in the infinite case can be modified to better approach that in the finite case, for example, by adding an additional term to include the stable vertical temperature gradient resulting from the meridional circulation(see i.e. Ali & McFadden (2005)). Nevertheless, the objective of this work is to identify those features which rely on the existence of axial end walls, and thus a conductive basic flow is considered.

These results provide us with relevant information to undertake a future study of baroclinic instabilities in an astrophysical context. The existence of axial end walls is a major problem when approximating the Keplerian velocity profile of accretion disks in laboratory experiments (Avila, 2012). The problem seems to have been solved with the experimental setup employed in Princeton (Ji *et al.*, 2006), consisting in a short aspect ratio facility where the end walls are split into two independently rotating rings. The end walls effect is mitigated by properly adjusting the angular velocity of each ring, and a close approximation to the quasi-keplerian azimuthal flow is obtained. In the absence of external heating the flow has been found to remain laminar at Reynolds of order 10^6, thus instabilities of pure hydrodynamics nature have been discarded as the possible mechanism underlying turbulence in these astrophysical structures. Recent simulations using more realistic models of accretion disks suggest the existence of subcritical baroclinic instabilities in presence of a radial temperature gradient (Klahr & Bodenheimer, 2003; Petersen *et al.*, 2007; Lesur & Papaloizou, 2010). In order to account for this possibility, experiments using a similar setup with lateral heating seem to be the next logical step in the investigation. However, the stable vertical stratification resulting from the meridional circulation poses a significant problem. Although real accretion disks are axially stratified, experiments and simulations focus on the the physics of the disk's mid-plane and thus neglect axial stratification. These conditions might be reproduced in the laboratory if the temperature difference between the axial end walls is minimized, for example, by heating the lower boundary, similarly to the experiments carried out by Stone *et al.* (1969) to study symmetric baroclinic instabilities. Nevertheless, experiments should only be undertaken very carefully, since the temperature profile near the bottom is modified and might result in unwanted dynamical behaviors. Since very large rotational speeds are involved in these experiments, frictional effects are expected to be negligible. However, testing this assumption is of particular importance in this context, because small discrepancies due to friction may entirely contaminate the extrapolation of the results to real accretion disks, where the expected Reynolds numbers are of order 10^{12}. Comparison with simulations in axially periodic systems will be therefore essential in order to determine the suitability of laboratory experiments to approximate

quasi-keplerian flows with a radial temperature gradient.

CHAPTER 6

ON THE DYNAMICS OF AXIALLY LOCALIZED STATES IN TAYLOR COUETTE FLOWS.

6.1 Introduction

The formation of spatially localized patterns within a homogeneous background state is a regular feature in a wide variety of pattern forming systems (see Dawes, 2010, and references therein). In fluid dynamics localized states are particularly relevant in linearly stable flows, in which the transition to turbulence occurs subcritically, when the amplitude of the perturbation exceeds a certain threshold which depends on the control parameter of the system. Flow patterns in which turbulent patches coexist with laminar flow emerge near the onset of transition and are believed to play a crucial role in organizing the complex dynamics of such transition. Examples of these localized states are found in canonical wall-bounded shear flows such as pipe flow (Mellibovsky *et al.*, 2009; Willis & Kerswell, 2009; Avila *et al.*, 2011; Eckhardt *et al.*, 2007) or plane Couette flow (Schneider *et al.*, 2010*a*; Duguet *et al.*, 2009; Barkley & Tuckerman, 2005; Schneider *et al.*, 2010*b*).

Spatially localized structures have also been observed in Taylor–Couette flow either when the transition scenario is subcritical or supercritical. Nevertheless, in contrast to the above-mentioned canonical flows, localization does not necessarily involve coexistence of laminar and turbulent flow, but sometimes manifests in the appearance of spatially confined regions in which some feature of the global background state is locally modified. An example of this phenomenon was reported in Heise *et al.* (2008), who using a combined experimental and numerical approach found the existence of spiral vortices with strongly localized amplitude near the end plates in the case of centrifugally stable counter-rotating cylinders. Also in the same regime of Taylor–Couette flow, Abshagen *et al.* (2010) showed the emergence of steady and axisymmetric vortices localized near the inner cylinder. These vortices appear smoothly in the basic state, resulting in a multiplicity of localized states which differ among themselves in the total number of vortices. The presence of a large scale circulation due to the presence of end walls seems to play a key role in the formation of these vortices. They could be related to a homoclinic snaking branch. More recently, axially localized states have been experimentally reported in the centrifugally unstable regime, in the case of rotating inner cylinder and stationary outer cylinder (Abshagen *et al.*, 2012). These pre-turbulent states occur for

sufficiently large values of the inner cylinder Reynolds number (Re_i), in systems in which the ratio between the length-to-gap aspect ratio (Γ) and the number of vortices (N) is restricted to the range $0.85 \simeq \frac{\Gamma}{N} \simeq 0.95$. They are characterized by the existence of large amplitude oscillations localized in some pairs of vortices. In all of these studies, despite the differences between the resulting states or the regime of Taylor–Couette flow considered, the phenomenon of localization results from the finite nature of experimental facilities, because of the interaction between the bulk flow and the Ekman vortices generated at the end plates. The competition between states with a different number of vortices (Eckhaus instability), modulated by the presence of end walls, also plays a role in the localization. Thus, simulations in axially periodic systems cannot capture this dynamics. In Abshagen *et al.* (2010) the background state over which localization takes place is a boundary-driven-large-scale circulation, which is a major difference with the laminar states in other linearly stable flows, whereas in Heise *et al.* (2008) and Abshagen *et al.* (2012), localization occurs over a global state, in which the oscillation amplitude of some vortices differ from that in the background state. In the former, this global background state consists of spirals propagating from mid-height towards the ends and viceversa, and in the latter, it is the bifurcated state (wavy vortex flow) resulting after Taylor-vortex flow (*TVF*) becomes unstable, which is usually known as Small Jet state (*SJ*) (Jones, 1985; Gerdts *et al.*, 1994).

The bifurcation scenario exhibited by the fluid in the experimental setup utilized in Abshagen *et al.* (2012) (wide gap $\eta = 0.5$ and moderate-large Γ) shows some very interesting dynamical features. A variety of states and transitions between them have been experimentally reported in Gerdts *et al.* (1994); von Stamm *et al.* (1996); Abshagen *et al.* (2012). There exist additional transitions to the classical Ruelle-Takens scenario described in section 1.3. Furthermore, these occurs for all *TVF* states, as long as the number of vortices is $N > 8$, in a wide range of Re_i. When Re_i is increased above a certain Re_{VLF} from the *SJ* state, the flow becomes quasi periodic due to the emergence of a very low frequency mode. However, in contrast to other modulated wavy flows (*MWVF*) (Coughlin & Marcus, 1992; Gorman & Swinney, 1982), this mode is axisymmetric ($n = 0$). The very low frequency mode (*VLF*), as was termed in Gerdts *et al.* (1994), plays an essential role in the dynamics of the flow, leading to the occurrence of chaos through a period-doubling route on T^2 tori (von Stamm *et al.*, 1996). This chaotic regime vanishes with further increase in Re_i and gives rise to the flow regime characterized by the existence of global states with axially localized large amplitude oscillations (Abshagen *et al.*, 2012). In this regime, localization may result in an extremely

large multiplicity of states which coexist in a wide range of the parameter space $\mathrm{Re}_i - \Gamma$.

The aim of this chapter is to extend the available information on the axially localized states regime (*ALS*) by means of a detailed numerical study of the parameter space in which these states occur. Due to the multiplicity of states, the dynamics is very complex and numerous sequences of previously unreported transitions have been found when the control parameters Re_i and Γ are varied. The *VLF* occurs in wide range of the parameter space and its interaction with the *ALS* appears to be crucial in most transitions, either between different *ALS* or to the chaotic regime. The rest of this chapter is structured as follows. The governing equations and the numerical method used to solve them are discussed in section 6.2. In section 6.3 we briefly describe the sequence of states preceding the *ALS* regime, paying especial attention to the *VLF* and the transition to *ALS*. The family of *ALS* found in this particular case is shown in 6.4.1. Its main features are enumerated and compared with the experimental results. In 6.4.2, the sequence of states exhibited by the fluid in the transition to chaos when Re_i and Γ are varied are illustrated. Finally, the main remarks are collected in section 6.5.

6.2 Governing equations and numerical method

6.2.1 Description of the system

We consider an incompressible fluid of kinematic viscosity ν confined between two concentric cylinders of length h and inner and outer radii r_i and r_o. The inner cylinder rotates at constant angular speed Ω, whereas the top and bottom end walls and outer cylinder remain at rest. The system is non-dimensionalized using the gap width, $d = r_o - r_i$, as the length scale and the viscous time d^2/ν as the time scale. The radius ratio is $\eta = 0.5$. The inner cylinder Reynolds number Re_i and the aspect ratio Γ are the control parameters of the system. The flow is governed by the incompressible Navier–Stokes equations

$$\partial_t \mathbf{v} + (\mathbf{v} \cdot \nabla)\mathbf{v} = -\nabla p + \Delta \mathbf{v}, \quad \nabla \cdot \mathbf{v} = 0 \,, \tag{6.1}$$

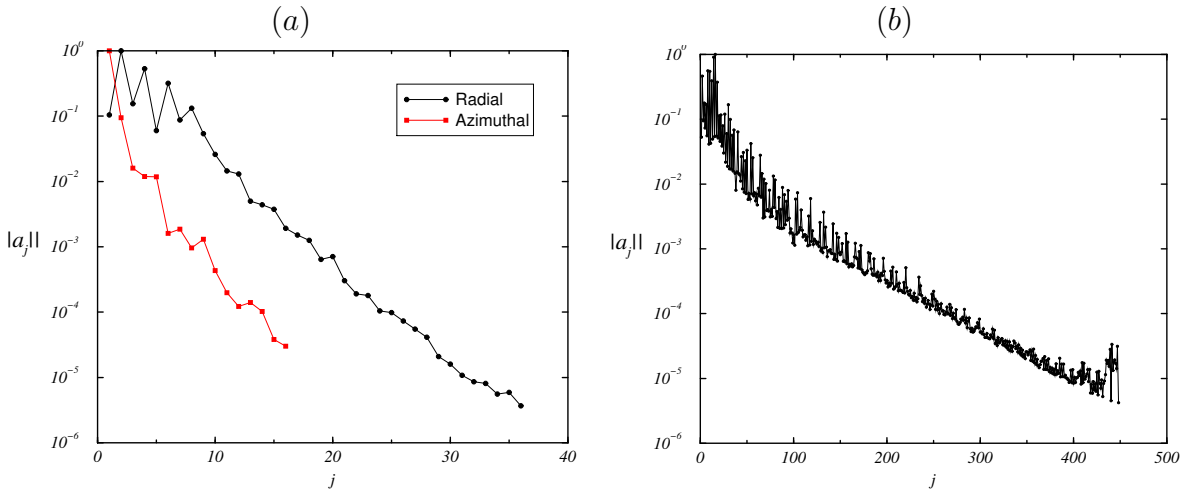

Figure 6.1: Convergence of the spectral coefficients of the axial velocity using the infinity norm. The flow corresponds to a weakly chaotic state found at $Re = 1300$ and $\Gamma = 9$, computed with $L = 36$ Chebyshev radial points, $M = 16$ Fourier modes and $N = 448$ Chebyshev axial points. (a) shows convergence in r and θ and (b) in z.

where $\mathbf{v} = (u, v, w)$ denotes the non-dimensional velocity field in cylindrical coordinates (r, θ, z). The no-slip boundary conditions are

$$\begin{aligned} \mathbf{v}(r_i, \theta, z, t) &= (0, Re_i, 0), \\ \mathbf{v}(r_o, \theta, z, t) &= (0, 0, 0), \\ \mathbf{v}(r, \theta, \pm\Gamma/2, t) &= (0, 0, 0). \end{aligned} \tag{6.2}$$

The governing equations and boundary conditions are invariant under arbitrary rotations R_ϕ about the axis, and the reflection K_z about the equatorial plane $z = 0$. The actions of these symmetries on the velocity field are:

$$R_\phi \mathbf{v}(r, \theta, z, t) = \mathbf{v}(r, \theta + \phi, z, t), \tag{6.3}$$

$$K_z \mathbf{v}(r, \theta, z, t) = (u, v, -w)(r, \theta, -z, t). \tag{6.4}$$

Together, they generate the symmetry group $\mathcal{G} = SO(2) \times Z_2$ of the system.

6.2.2 Numerical formulation and methodology

The governing equations (6.1) have been solved using the spectral solver described in 2.2.

We have checked the spectral convergence of the code using the infinity norm of the spectral coefficients $(a_{l,m,n})$ of the computed solutions, defined as $||a_l||_\infty = \max_{n,m} |a_{l,n,m}|$ for

the radial direction, and analogously for the axial and azimuthal directions. Figure 6.1 shows $||a_j||_\infty$, with $j = l, n, m$, of the axial velocity w for a weakly chaotic state taking place at $Re = 1300$ and $\Gamma = 9$. This solution has been computed with $L = 36$ and $N = 448$ Chebyshev points in r and z, and $M = 16$ Fourier modes in θ, ensuring that the trailing coefficients of the spectral expansion are at least four orders of magnitude smaller than the leading coefficients. Time steps as small as $\delta t = 5 \times 10^{-6}$ have been required for numerical stability and accuracy of the second-order temporal scheme.

Time series of the axial velocity at three different points, $w_1(r = 1.2, \theta = 0, z = \Gamma/4)$, $w_2(r = 1.2, \theta = 0, z = -\Gamma/4)$ and $w_3(r = 1.2, \theta = 0, z = 0)$, are simultaneously recorded. A subsequent spectral analysis of these data via fast Fourier transform, together with phase portraits and Poincare sections are used as tools to identify the different transitions that take place as the control parameters are varied (see Moon, 2008, for a simple description of these methods).

6.3 Flow patterns and transitions towards the ALS regime

6.3.1 Taylor Vortex Flow

There exist a variety of steady TVF , differing in the number of vortices N present in the fluid domain, which coexist for the same values of Re_i and Γ (Benjamin & Mullin, 1982). They are very sensitive to the initial conditions of the system and thus depend on the path followed by the fluid in the parameter space. The choice of a certain TVF as initial state determines in many cases the sequence of transitions exhibited by the fluid as Re_i is increased. However, the complete bifurcation scenario described along this paper is very robust, taking place in the same region of a normalized parameter space $\mathrm{Re}_i - \frac{\Gamma}{N}$, provided that $N \geq 8$ (see figure 2 in von Stamm *et al.* (1996) and figures 5 and 7 in Abshagen *et al.* (2012)). Here, we focus on a TVF with $N = 10$ vortices, which allows us to find a significant number of axially localized states in moderate aspect ratio systems ($8.6 < \Gamma < 9.5$) at an affordable computational cost. In addition, this complements the experimental work of Abshagen *et al.* (2012), in which axially localized states were reported for the cases of $N = 8$ and $N = 12$ vortices. Figure 6.2 illustrates the streamlines (a) and angular momentum (b) of this state. Five outgoing jets emerge from the inner cylinder due to the centrifugal instability. The two cells at the cylinders ends are larger than the rest of cells due to the Ekman layers resulting from the interaction between fluid and end walls. The kinetic energy of the fluid is

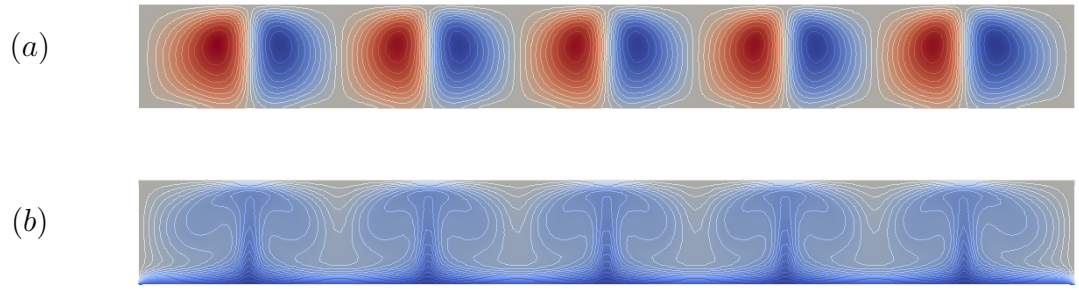

Figure 6.2: Axisymmetric 5-jet (10 vortices) TVF state at $\mathrm{Re}_i = 400$ and $\Gamma = 9$ on a meridional plane $(r, z) \in [1, 2] \times [-\Gamma/2, \Gamma/2]$ at $\theta = \pi$. (a) Streamlines. There are 10 positive and negative contours in $[-28.45, 28.45]$. (b) Angular momentum. There are 20 contours in $[-400, 0]$.

concentrated in the boundary layer at the inner cylinder and in the outgoing jets, which are thinner and more intense than the return ingoing jets.

6.3.2 Small and Large Jet States

The axisymmetric 5-jets *TVF* state loses stability at $\mathrm{Re}_i \approx 425$ via a Hopf bifurcation to a rotating wave with azimuthal wave number $n = 1$. Figures 6.3 (a) and (b) show respectively contours of angular momentum of the resulting state at $\mathrm{Re}_i = 700$ and $\Gamma = 9$ on cylindrical (θ, z) and meridional (r, z) sections of the apparatus. It is observed that the oscillations mainly occur at the outgoing jets, while the ingoing jets remain in the same axial place for all angle values θ. The exception are the two outgoing jets near the end walls which also remain stationary. A phase difference of 180 degrees between oscillations in contiguous outgoing jets can be seen in figure 6.3 (a). These features are in full agreement with experimental observations (Gerdts *et al.*, 1994) as well as with the numerical work by Jones (1985) in infinite long cylinders. Figure 6.3 (c) shows the evolution of the axial velocity w over the line $r = 1.8$, $\theta = \pi$, $z \in [-\Gamma/2, \Gamma/2]$, recorded at 20 different time steps and overlapped on the same plot. The oscillations of the outgoing jets are reflected in the thicker lines located in the bulk vortices. As a result of the oscillations the axial velocity in these vortices is larger than that in the Ekman vortices. Since the outgoing jets are thinner than the ingoing ones, the terminology small-jet state *SJ* and small jet instability has been typically used in the literature to refer to this state. Both the $SO(2)$ rotational symmetry and the K_z reflection symmetry $(z \to -z)$ of the *TVF* are broken in the Hopf bifurcation to the *SJ*, but this state still

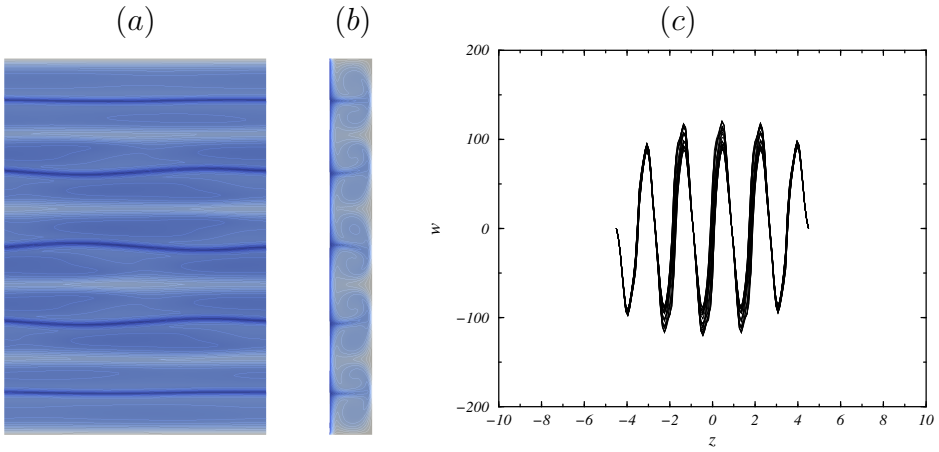

Figure 6.3: Small jet mode at $\mathrm{Re}_i = 700$ and $\Gamma = 9$. Contours of angular momentum rv, (a) on a cylindrical surface $(\theta, z) \in [0, 2\pi] \times [-\Gamma/2, \Gamma/2]$ at $r = 1.5$ and (b) on a meridional plane $(r, z) \in [1, 2] \times [-\Gamma/2, \Gamma/2]$ at $\theta = \pi$. (c) Overlapped axial velocity profiles w over the line $r = 1.8, \theta = \pi, z \in [-\Gamma/2, \Gamma/2]$, corresponding to 20 different time steps.

retains a discrete spatial Z_2 symmetry, the composition of a half-turn (a rotation of π around the cylinder axis) and the K_z reflection. This symmetry, which can be observed in figure 6.3 (a), is the central reflection (also called the inversion $\mathcal{I}$) respect to the center of the cylindrical domain ($r = 0$ and $z = 0$). The spatial $SO(2)$ rotational symmetry of the TVF becomes a spatio-temporal symmetry of the rotating wave: a rotation of angle α is equivalent to a time evolution of $t = \alpha / f_p$, where f_p is the precession frequency of the SJ. The value of f_p varies between 44-48% of the rotation frequency of the inner cylinder as Re_i is increased.

There exist another global wavy vortex flow which coexists with the SJ in a wide region of the parameter space (for $\mathrm{Re}_i > 700$), and is characterized by the large amplitude of its oscillations. For this reason it is often referred to as Large Jet (LJ) state. In order to compare the SJ and LJ states, figure 6.4 illustrates the LJ state at $\mathrm{Re}_i = 720$ and $\Gamma = 9.25$ similarly to figure 6.3. The main oscillations happen again in the outgoing jets, showing a substantial increase in the amplitude of the oscillations with respect to that in the SJ state. Nevertheless, in contrast to SJ, the outgoing jets oscillate in phase. Oscillations of the ingoing jets can be discerned in this flow pattern. The amplitude of these oscillations is much lower than that in the outgoing jets and they occur in antiphase with the oscillations of the outgoing jets. The precession frequency of the LJ remains around 56% of the rotation frequency of the inner cylinder. All these observations coincide with previously reported descriptions of this flow pattern (Gerdts

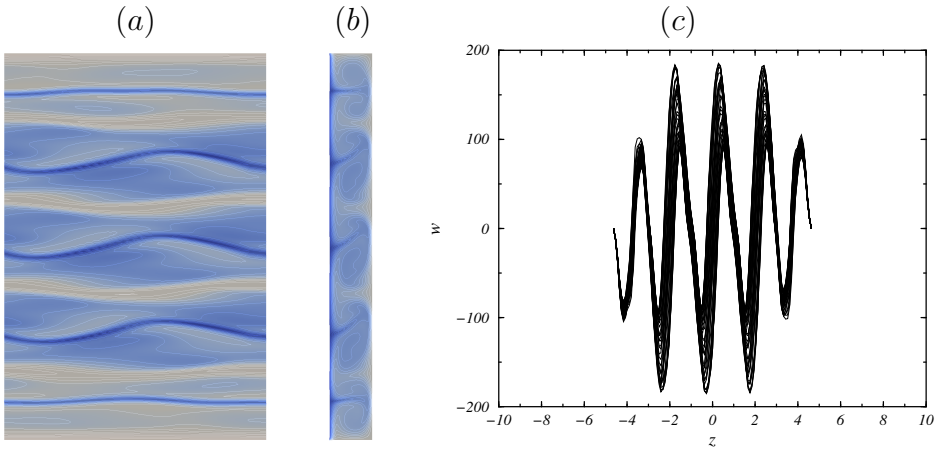

Figure 6.4: Large jet mode at $\mathrm{Re}_i = 720$ and $\Gamma = 9.25$. Contours of angular momentum rv, (a) on a cylindrical surface $(\theta, z) \in [0, 2\pi] \times [-\Gamma/2, \Gamma/2]$ at $r = 1.5$ and (b) on a meridional plane $(r, z) \in [1, 2] \times [-\Gamma/2, \Gamma/2]$ at $\theta = \pi$. (c) Axial velocity profiles w over the line $r = 1.8, \theta = \pi, z \in [-\Gamma/2, \Gamma/2]$, recorded for 40 different time steps and overlapped on the same plot.

et al., 1994). The *LJ* preserves the same discrete symmetry group Z_2 as the *SJ*.

6.3.3 Very Low Frequency mode

With the increase of Re_i there is a small phase shift in the oscillations of contiguous vortices. This phase difference results in small wavelength-disturbances which slowly propagate in axial direction, giving rise to the appearance of an axisymmetric mode $n = 0$, known as very low frequency mode (*VLF*). The resulting quasi-periodic state was first reported in Gerdts *et al.* (1994), and characterized in detail by von Stamm *et al.* (1996) in a subsequent experimental study.

The discrete central reflection retained by the *SJ* and *LJ* is broken due to the occurrence of *VLF*. This is illustrated in figure 6.5 at $\mathrm{Re}_i = 780$ and $\Gamma = 9$. It shows contours of angular momentum on two opposite (differing by an angle of π) meridional planes, being the second plane (b) vertically reflected $(z \to -z)$. If the central inversion symmetry were preserved, both figures should be identical, however there are small differences, mainly around the second and fourth outgoing jets.

The dynamical behavior of the *VLF* is very sensitive to changes in N and Γ. Abshagen & Pfister (2000) experimentally found a transition between two types of *VLF* with different features at $\frac{\Gamma}{N} = 0.907$. Below this value, the onset of the *VLF* occurs via a homoclinic

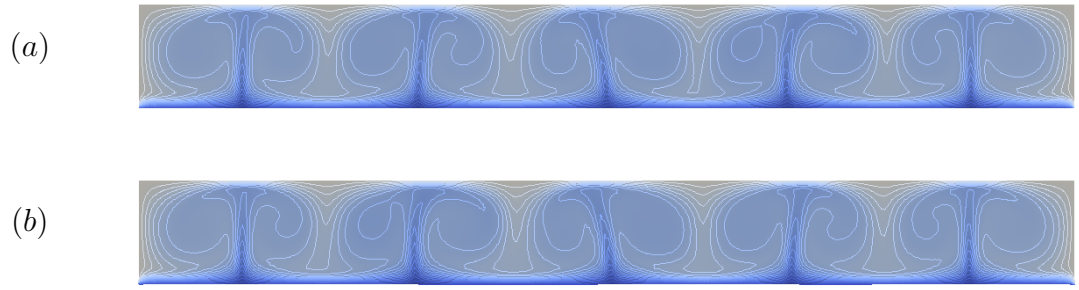

Figure 6.5: VLF state at $\mathrm{Re}_i = 780$ and $\Gamma = 9$. (a) Contours of angular momentum on a meridional plane $(r, z) \in [1, 2] \times [-\Gamma/2, \Gamma/2]$ and $\theta = \pi$. (b) The inverse-symmetric of (a) ($\theta \to \theta + \pi$ and $z \to -z$). There are 20 contours in $[-780, 0]$

bifurcation, whereas for $\frac{\Gamma}{N} > 0.907$ it takes place for larger values of Re_i through a Hopf bifurcation, resulting in an oscillation frequency one order of magnitude larger than that in the homoclinic case. The scenarios of transition to chaos also vary among the different experimental studies. For example, in von Stamm *et al.* (1996), the flow undergoes a period doubling route to chaos, whereas in Abshagen & Pfister (2000), a transition to chaos via spatio-temporal intermittency was found.

In the study here undertaken, the *VLF* emerges from a Hopf bifurcation and the flow approaches chaos via the period-doubling bifurcation cascade which is sketched in figure 6.6. The sequence of states that occur throughout the period-doubling route to chaos cannot be identified by visual inspection of the flow patterns, but requires the analysis of time series recorded over a long simulation time. The different states of this sequence are shown in figure 6.7. Figure 6.7 (a) illustrates the *VLF* state near the bifurcation ($\mathrm{Re}_i = 770$). The frequency spectrum (first column) shows the large difference between the frequencies of the underlying rotating wave, in this case the *SJ*, and the frequency of *VLF*, f_p and f_{VLF} respectively. An increase in the power spectral density (PSD) of the harmonics of f_{VLF} near f_p is another distinctive mark of these solutions. The phase portrait of the trajectories defined by the axial velocities w_1 and w_2 in the phase plane is displayed in the second column. It reflects the toroidal structure of the *VLF* state due to the actions of f_p and f_{VLF}. To facilitate the visual interpretation of the phase portraits, we have also computed the intersections of these trajectories with a carefully chosen plane, the so-called Poincare section, in which the action of f_p is removed. This is depicted in the third column, showing a single closed orbit corresponding to the low frequency motion. The *VLF* doubles its period (P to $P2$) for the first time at $\mathrm{Re}_i \approx 782$. The frequency spectrum in figure 6.7 (b) illustrates the emergence of the new frequency

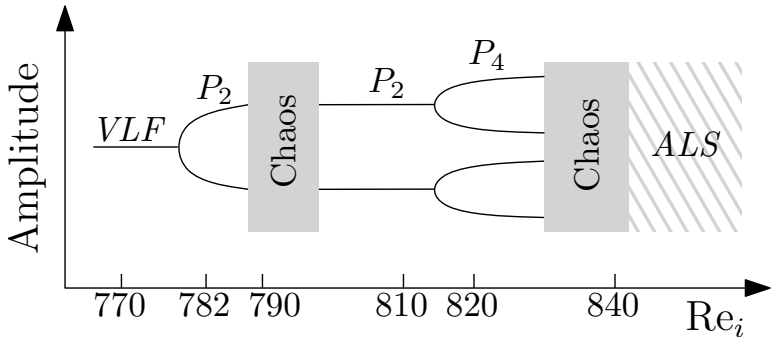

Figure 6.6: Schematic of the period doubling route to chaos exhibited by the *VLF* as Re_i is increased, for $\Gamma = 9$. The solutions at the Re_i indicated are described in figure 6.7.

$f_{VLF_2} = \frac{f_{VLF}}{2}$. Since the dynamics is entirely dominated by the very low frequency mode, only the low frequency spectrum is shown in this and the subsequent states of the sequence. The period doubling bifurcation can also be easily observed in the Poincare section, where a new periodic orbit emerges, with twice the period of the original orbit. Further increasing Re_i, the flow becomes weakly chaotic at $\mathrm{Re}_i \approx 788$, which is illustrated in figure 6.7 (*c*), and remains disordered up to $\mathrm{Re}_i \approx 810$. Here, the flow recovers the period $P2$ (see figure 6.7 (*d*)), however, a comparison between the phase portraits in figures 6.7 (*b*) and (*d*) reveals that the structure of the new state differs from that before the chaotic regime. A subsequent increase in Re_i leads to a new period doubling ($P4$), $f_{VLF_4} = \frac{f_{VLF_2}}{2}$, which is illustrated in figure 6.7 (*e*) at $\mathrm{Re}_i = 820$. The phase portrait resembles that in 6.7 (*d*), nevertheless, the enlargement of the phase trajectories is reflected in the fact that, for the same simulation time in both cases, the torus surface in 6.7 (*e*) has not been filled yet. The flow becomes chaotic again with further increase in Re_i. This flow regime is shown at $\mathrm{Re}_i = 840$ in figure 6.7 (*f*). Finally, the chaotic behavior disappears at $\mathrm{Re}_i \approx 855$ and gives rise to the regime of axially localized states which is discussed in the next section.

6.4 Axially Localized States

6.4.1 Description

A new pre-turbulent flow regime arises for $\mathrm{Re}_i \geq 855$ and $8.6 < \Gamma < 9.5$. The resulting flow patterns are characterized by the existence of large amplitude oscillations localized on some of the outgoing jets of the bulk vortices. Due to this particularity we refer to

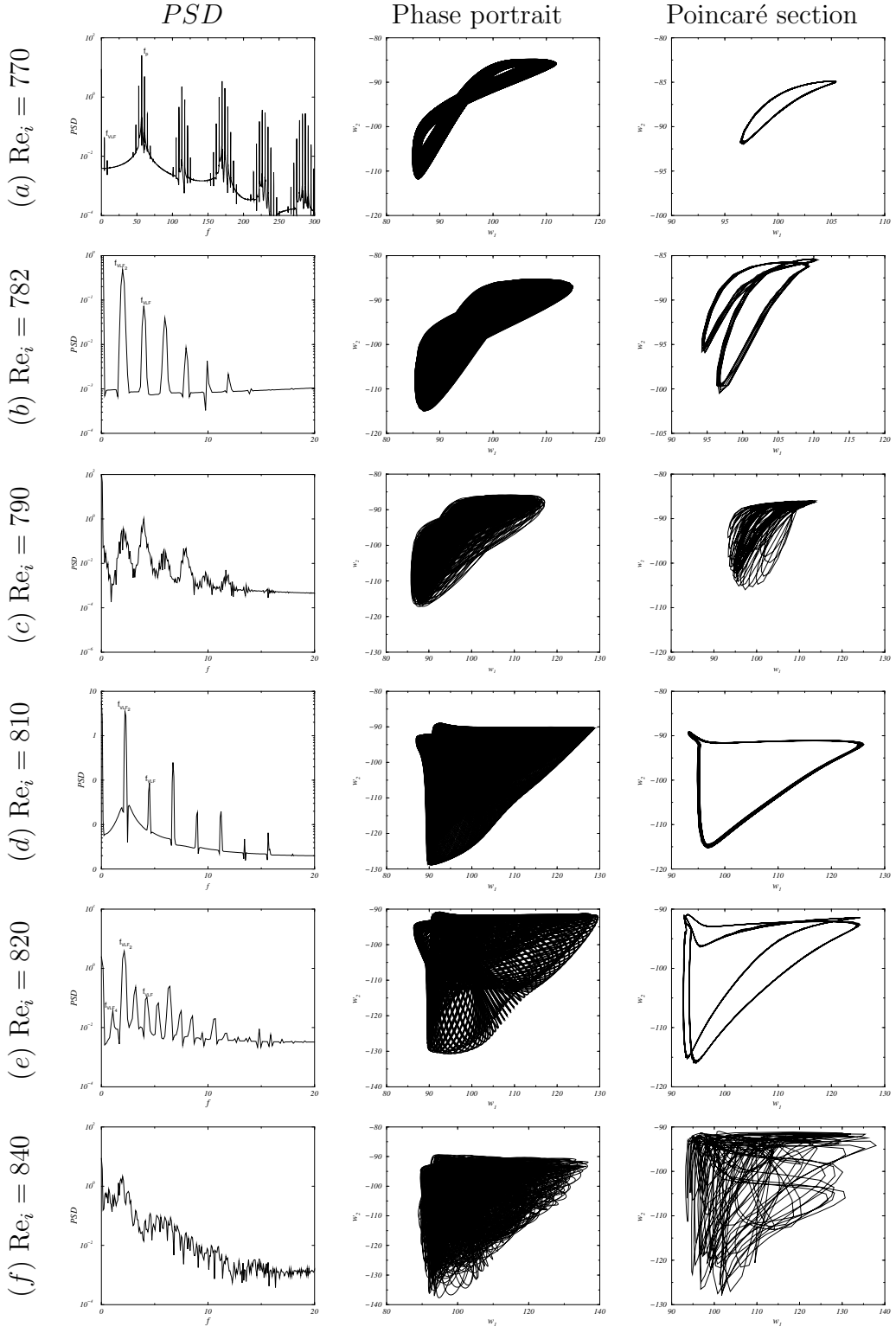

Figure 6.7: Power spectral density PSD, phase portrait and Poincare section illustrating the sequence of period-doubling bifurcations sketched in figure 6.6 at $\Gamma = 9$. (a) VLF at $\mathrm{Re}_i = 770$, near the bifurcation; (b) first period doubling $P2$ of VLF at $\mathrm{Re}_i = 782$; (c) first chaotic solution at $\mathrm{Re}_i = 790$; (d) state with period $P2$ but different structure at $\mathrm{Re}_i = 810$; (e) second period doubling $P4$ of VLF at $\mathrm{Re}_i = 820$; (f) chaotic flow at $\mathrm{Re}_i = 840$.

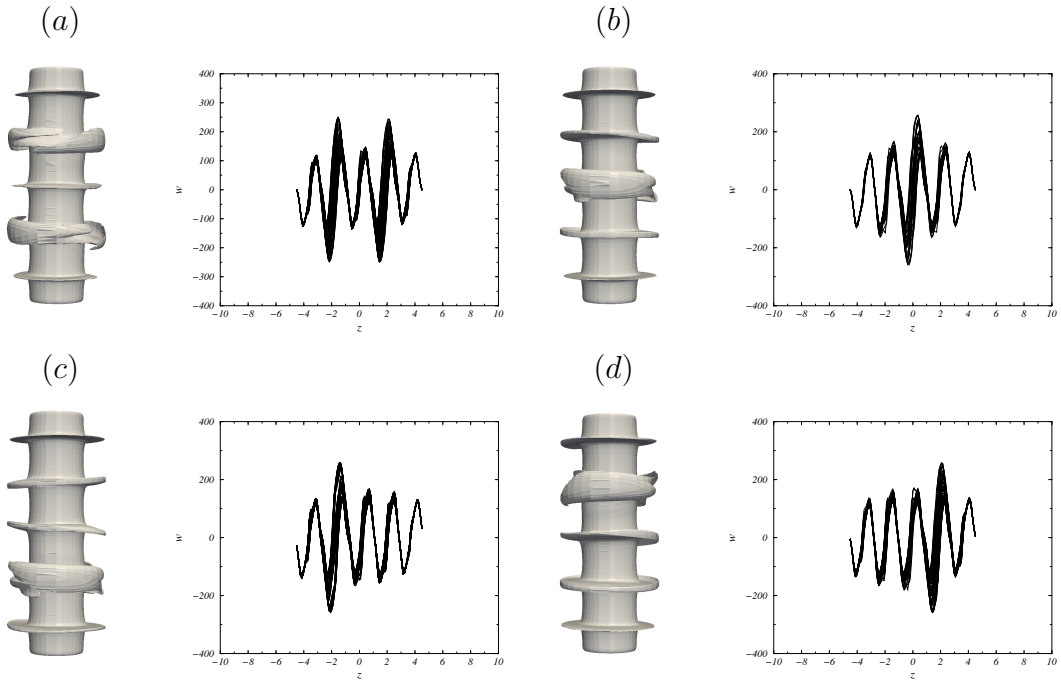

Figure 6.8: Three-dimensional contour of the angular momentum ($rv = -450$) and axial velocity profiles w recorded at $r = 1.8, \theta = \pi$ and $z \in [-\Gamma/2, \Gamma/2]$ for 40 different time steps and overlapped on the same plot. (a) ALS_{10} at $\mathrm{Re}_i = 920$ and $\Gamma = 9$, (b) ALS_4 at $\mathrm{Re}_i = 960$ and $\Gamma = 9$, (c) ALS_8 at $\mathrm{Re}_i = 960$ and $\Gamma = 9.1$, and (d) ALS_2 at $\mathrm{Re}_i = 960$ and $\Gamma = 9.3$. The nomenclature ALS_{number} is carefully explained in the text.

these flow structures as axially localized states (*ALS*). The main consequence of this localization is the appearance of multiple steady states, differing in the axial position of the outgoing jet (or jets) showing the large amplitude oscillations. Thus, a remarkably high number of *ALS* can be observed when the aspect ratio Γ and the number of vortices N in the flow are changed. The *ALS* were found experimentally by Abshagen *et al.* (2012), who reported the existence of a wide spectrum of *ALS* for several N-vortex flows, many of which coexist in the parameter space, giving rise to a very complex and intriguing dynamics. They also explored the variation in the wavelength λ of the different pairs of vortices when Re_i changes, concluding that λ increases with Re_i in the pairs of vortices where localization occurs, and decreases with Re_i in the Ekman vortices. In this section, apart from confirming numerically these experimental results, we focus on the transitions taking place within this region of the parameter space, which eventually lead to chaotic behavior.

The family of *ALS* numerically obtained for the $N = 10$ vortex flow is illustrated in figure 6.8 through a three-dimensional contour of angular momentum $rv = -450$, which

reflects the axial localization of the large jet oscillations, and a plot such as that in figures 6.3 (c) and 6.4 (c), which gives a clear idea of the difference in amplitude between the localized large jet oscillations and the oscillations in the rest of vortices. As occurred in Abshagen *et al.* (2012), not all possible ALS (6 in the case of a 10-vortex flow) have been found. This could mean that the remaining ALS are unstable, or simply that very specific sequences of states, which have not been detected in this study, are required to reach these states. To denote the different ALS, we have adopted the nomenclature used in Abshagen *et al.* (2012). Each ALS can be expressed with a binary number where, the pairs of vortices with large amplitude oscillations are indicated with ones, and the rest of vortices are denoted by zeros. This binary number is converted into decimal base, starting from the Ekman vortex at the top, and placed as subscript of ALS. For example, the binary number corresponding to the state in figure 6.8 (c) is 01000 because the only pair of vortices oscillating with large amplitude is the second one starting from the bottom. It is subsequently converted to decimal base (8) and the state is referred to as ALS_8. Depending on the location of the large jet oscillations, the ALS may or not preserve the axial reflection symmetry. The symmetric states in figures 6.8 (a) and (b), denoted by ALS_{10} and ALS_4 respectively, can be obtained as a direct transition from any of the states described in section 6.3. In contrast, the asymmetric states ALS_8 and ALS_2, shown in figures 6.8 (c) and (d), are only found when starting the simulation from other ALS.

Figure 6.9 shows the states achieved in the simulations performed for $\mathrm{Re}_i > 850$, overlapped in the parameter space with the experimentally measured critical boundaries (Abshagen *et al.*, 2012). There are two different boundaries corresponding to flows with a distinct number of vortices, $N = 8$ and $N = 12$, which are represented as solid and dashed lines respectively. The region of the parameter space where the ALS occur is delimited by the lines ALS_l and ALS_h, being the zone H_{ALS} comprised between ALS_r (transition curve from chaotic VLF to ALS when increasing Re_i) and ALS_h a hysteretic region. The onset of the LJ state is indicated by the line LJ_l, whereas similarly to the ALS, there is also a hysteretic region for the LJ, which is contained inside the curve LJ_h. It can be seen that all numerical results lie in parameter space consistently with experiments. The four ALS found coexist for the same values of Re_i and Γ, so that obtaining each of them critically depends on the path followed in the parameter space. The ALS_{10}, indicated with diamonds in figure 6.9, is the only one of the computed ALS where two outgoing jets oscillate with large amplitude. It is the most stable ALS for the lowest values of Re_i ($855 \leq \mathrm{Re}_i \leq 1050$) in which the regime of ALS takes place. This is in agreement with Abshagen *et al.* (2012), where the states with the highest number of

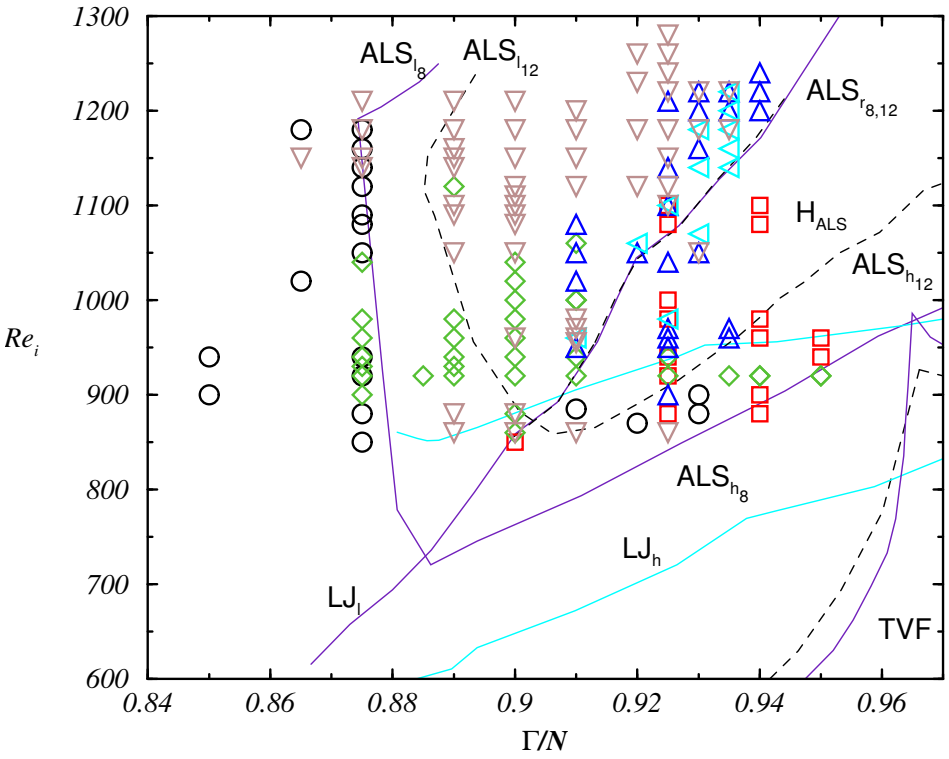

Figure 6.9: Distribution in the parameter space of the flow patterns obtained when $\mathrm{Re}_i > 850$. The solid lines represent the experimental stability boundaries for the case of $N = 8$ (solid line) and $N = 12$ (dashed line) given in (Abshagen *et al.*, 2012). Circles (black) and squares (red) stand for the LJ and SJ states respectively, whereas the axially localized states are denoted as diamonds (green) for the ALS_{10}, down triangles (brown) for the ALS_4, up triangles (dark blue) for the ALS_8 and left triangles (soft blue) for the ALS_2.

axially localized large jet oscillations were also found at the lowest values of Re_i. Also in accordance with these experimental results is the fact that all ALS with large jet oscillations localized on a single outgoing jet have been found. The symmetric ALS_4, marked with down triangles in figure 6.9, is very stable in the range $1050 \leq \mathrm{Re}_i \leq 1280$, whereas the states ALS_8 and ALS_2, indicated with left and up triangles respectively, are found when considering longer systems ($9.1 \leq \Gamma \leq 9.4$). All ALS can be found hysteretically, coexisting with the SJ in ALS_h, and with the LJ in the region of the parameter space resulting from the intersection of ALS_h and LJ_h.

The formation of a certain ALS obeys to a specific stable arrangement of the wavelengths of the vortex pairs within a system of finite length. However, the phases of oscillation of the different ALS exhibit the same coherence as for the LJ state. This can be seen from figures 6.10 (a) and (b), which show the contours of angular momentum on a cylindrical

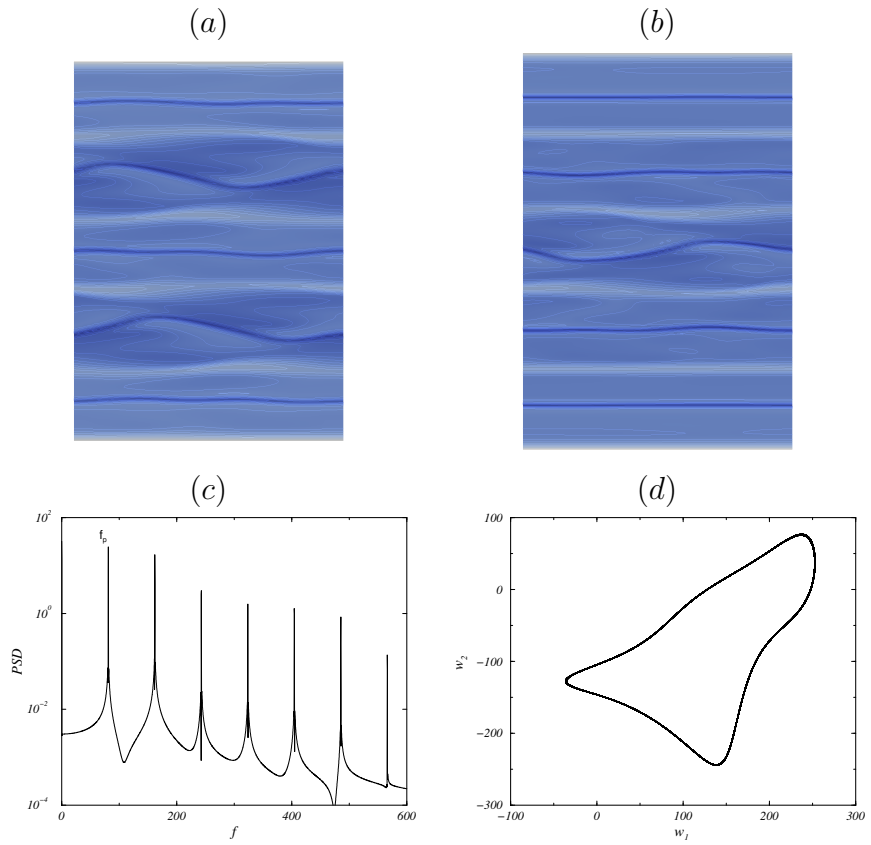

Figure 6.10: Contours of angular momentum rv on a cylindrical surface $(\theta, z) \in [0, 2\pi] \times [-\Gamma/2, \Gamma/2]$ at $r = 1.5$ for (a) ALS_{10} at $\mathrm{Re}_i = 920$ and $\Gamma = 9.25$; and (b) ALS_4 at $\mathrm{Re}_i = 1260$ and $\Gamma = 9.25$; (c) and (d) are respectively the power spectral density (PSD) and phase portrait for ALS_{10} at $\mathrm{Re}_i = 920$ and $\Gamma = 9.25$.

surface for the ALS_{10} and ALS_4. In both figures the outgoing jets oscillate in phase (although it is quite difficult to visually distinguish this feature between contiguous jets with large and small amplitude oscillation) and weak oscillating ingoing jets are in antiphase with the oscillations of the outgoing jets. While the ALS preserve this phase coherence they are found as rotating waves in the parameter space, precessing with the same oscillation frequency, $f_p \approx 55\%$ of the rotation frequency of the inner cylinder, as the LJ state. Figures 6.10 (c) and (d) show the frequency spectrum and phase portrait of the ALS_{10} at $\mathrm{Re}_i = 920$ and $\Gamma = 8.85$, clearly illustrating its behavior as rotating wave. As in 6.3.3, the breaking of the phase coherence of the different vortex-pairs leads to the emergence of the VLF, which coexists with the ALS in a wide range of control parameters, and plays a crucial role in the transitions to chaos described below.

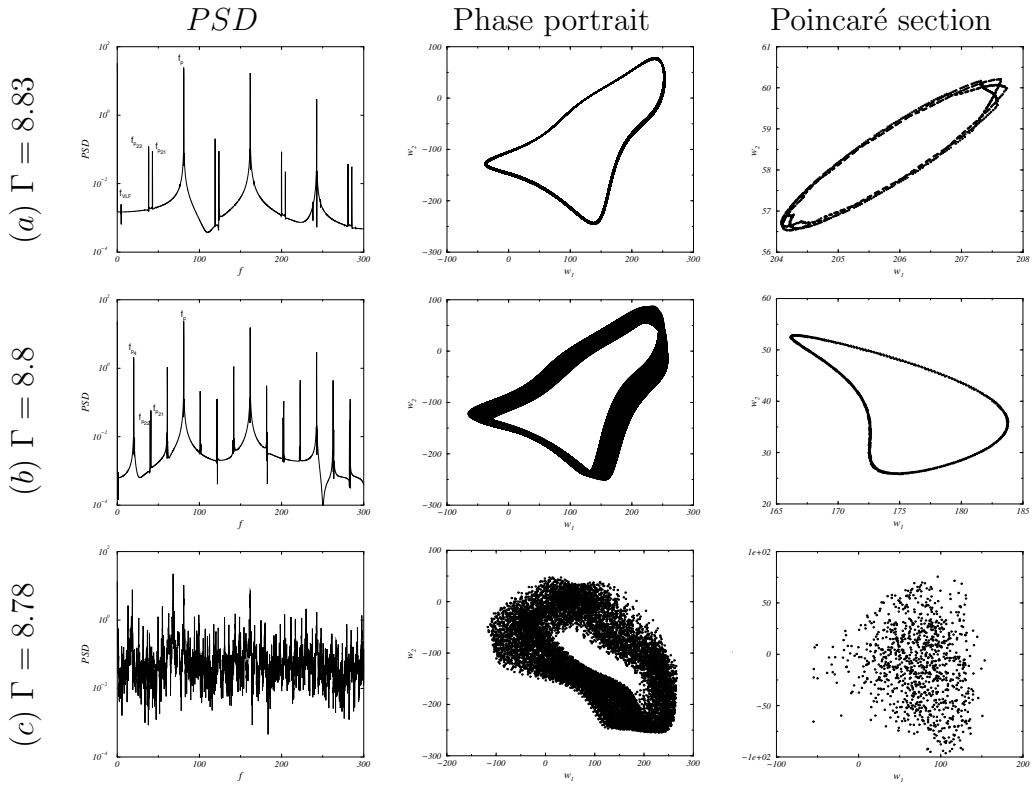

Figure 6.11: Power spectral density, phase portrait and Poincaré section illustrating the sequence of states in the route to chaos when $\mathrm{Re}_i = 920$ and Γ is decreased. The initial state is the ALS_{10} at $\mathrm{Re}_i = 920$. (a) State resulting from the first transition at $\Gamma = 8.83$; (b) State resulting from the second transition at $\Gamma = 8.80$; (c) Chaotic flow at $\Gamma = 8.78$.

6.4.2 Transition to chaos

As a consequence of the diversity of states coexisting in the parameter space there exist multiple routes to chaos. Each one is determined by the initial state and the path followed in the parameter space, differing from the others in the number of transitions and types of ALS arising. Nevertheless, despite the complexity introduced by the coexistence of states, the dynamical behavior associated with the transitions is similar in all cases and depends essentially on the control parameter that is varied.

Figure 6.11 shows an example of the bifurcation scenario occurring when Γ is reduced. In this case, $\mathrm{Re}_i = 920$ is fixed and the initial state of the sequence is the ALS_{10} at $\Gamma = 9.25$ (rotating wave with precession frequency f_p shown in figures 6.10 (c) and (d)). This state is stable up to $\Gamma = 8.84$, where the transition illustrated in figure 6.11 (a) takes place. The frequency spectrum (PSD) suggests that the coupling between the oscillations of the different vortex pairs is broken simultaneously with the period

doubling of the main frequency f_p, resulting in the appearance of two frequencies $f_{p_{21}}$ and $f_{p_{22}}$, with similar amplitudes and equidistant from the value $f_{p_2} = f_p/2$, corresponding to the frequency of the period doubling. The small difference between $f_{p_{21}}$ and $f_{p_{22}}$ results in a very low frequency f_{VLF} which involves, similarly to the *VLF* described in section 6.3, the axial propagation of the wavelength-disturbances of the different vortex pairs. Hence, $f_{p_{21}}$ and $f_{p_{22}}$ can be expressed in terms of f_{VLF} and f_p, as $f_{p_{22}} = \frac{f_p - f_{VLF}}{2}$ and $f_{p_{21}} = \frac{f_p + f_{VLF}}{2}$. It should be noted that f_{VLF} is in this case nearly twice f_{VLF} in the *VLF* state. The fact that there are two frequencies of similar amplitude arising at the same time is probably related to the existence of two vortex pairs with large jet oscillations in the ALS_{10}. The new state is therefore a two dimensional torus in the phase space. Nevertheless, the amplitude of the main frequency is much higher than that for the additional frequency, so that the phase portrait resembles a limit cycle. The intersection of the invariant torus with a Poincare section shows a closed orbit which, similarly to a period-doubling bifurcation, follows two different loops. This reflects the coupling between the mechanism responsible for the period-doubling of the main frequency and the oscillation due to the very low frequency mode. Due to the small region of the phase plane in which the orbit is located, it is quite difficult to distinguish the full trajectory of the orbit in 6.11 (a). As far as we know this transition has not been previously reported, however, there exist a few works in the realm of the dynamical system theory that analyze a problem resembling the transition above described. They discuss the influence of a periodic perturbation in a non-linear system which is close to a period-doubling bifurcation (Horner, 1983; Bryant & Wiesenfeld, 1986; Svensmark & Samuelsen, 1990). In all of these studies, the dynamics is entirely dominated by the periodic perturbation, which suppresses the period doubling bifurcation. This behaviour is somewhat similar to that of the aforementioned bifurcation, with f_{VLF} playing the dynamical role of the periodic perturbation.

When Γ is reduced from 8.84 to approximately 8.81, the amplitudes of $f_{p_{21}}$, $f_{p_{22}}$ and f_{VLF} gradually increase. For Γ values below 8.81, f_p undergoes a second period doubling bifurcation, which is clearly illustrated in figure 6.11 (b). In this case, unlike the first period doubling, there is a single frequency arising at $f_{p_4} = f_p/4$, whose amplitude is substantially larger than that for $f_{p_{21}}$ and $f_{p_{22}}$. This transition seems to help restore the phase coherence of the initial state. This is reflected in the fact that $f_{p_{21}}$ and $f_{p_{22}}$ closely approach f_{p_2}, so f_{VLF} becomes approximately zero. Nevertheless, the flow is still quasi-periodic, as indicates the limit cycle displayed in the Poincare section. The phase portrait reveals the same initial spatial structure, which becomes increasingly thicker as the flow approaches chaos. When we further reduce Γ, the flow becomes suddenly

chaotic at $\Gamma = 8.78$. This behavior is easy to identify in figure 6.11 (c). For example, the Poincare section clearly shows the loss of periodicity of the previous states, giving rise to a cloud of points in the phase space. The flow remains chaotic up to $\Gamma \approx 8.5$, where it bifurcates to a more stable state with $N = 8$ vortices. It is noticeable that all transitions happen in a very short range $8.78 \leq \Gamma \leq 8.84$. This sequence of transitions to chaos as Γ is decreased has only been found for $\mathrm{Re}_i \leq 950$, when using ALS_{10} as initial state. For higher Re_i or a different initial state, the flow approaches chaos similarly when reducing Gamma or increasing Re_i, as is described below.

Figure 6.12 shows the sequence of bifurcations to chaos that occurs when Re_i is increased and $\Gamma = 9.25$. The initial state is the same as in the transition described above, the ALS_{10} at $\mathrm{Re}_i = 920$. This state loses stability at $\mathrm{Re}_i = 948$, resulting in a similar state to that obtained after the first transition when decreasing Γ. The frequency spectrum in figure 6.12 (a) (corresponding to $\mathrm{Re}_i = 952$), displays the same behavior as in figure 6.11 (a). Again, it is observed that two additional frequencies, $f_{p_{21}}$ and $f_{p_{22}}$, arise in the vicinity of the frequency $f_{p_2} = f_p/2$, corresponding to the period doubling of the main frequency f_p. These frequencies cause the appearance of a very low frequency, $f_{VLF} = f_{p_{21}} - f_{p_{22}}$, which is about twice f_{VLF} of the VLF state found in section 6.3. The phase portrait and Poincaré section in figure 6.12 (a) are also qualitatively similar to those in figures 6.11 (b) and (c). A close-up has been included in the Poincaé section in order to discern the complex path followed by the periodic orbit. The amplitude of f_{VLF} grows progressively with the increase of Re_i. This fact, which is reflected in figure 6.12 (b) at $\mathrm{Re}_i = 980$, might be ascribed to the increasing phase difference between the oscillations of contiguous vortices with respect to the initial state, which result in larger wavelength-disturbances. Further increasing Re_i the ALS_{10} becomes weakly chaotic, and subsequently bifurcates into another axially localized state which is more stable at higher values of Re_i, the ALS_4. This transition, which takes place at $\mathrm{Re}_i = 1030$, is illustrated in figure 6.12 (b). The existence of a new state can be seen from the phase portrait, which reveals an entirely different structure with respect to that in figures 6.12 (a) and (b). There also exist a low frequency f_{LF} coexisting with the precession frequency of the rotating wave, which is one order of magnitude higher than f_{VLF} in the previous state. The dynamics is still on a 2d torus surface, as is reflected by the single closed orbit shown in the Poincaré section. The amplitude of f_{LF} decreases with the increase of Re_i, so the ALS_4 progressively turns into a rotating wave. This happens at $\mathrm{Re}_i \approx 1130$, where f_{LF} completely disappears and the ensuing flow pattern is a pure rotating wave with precession frequency f_p. This behavior, which is illustrated in figure 6.12 (d) at $\mathrm{Re}_i = 1260$, persists up to $\mathrm{Re}_i \approx 1275$. Note that the Poincaré

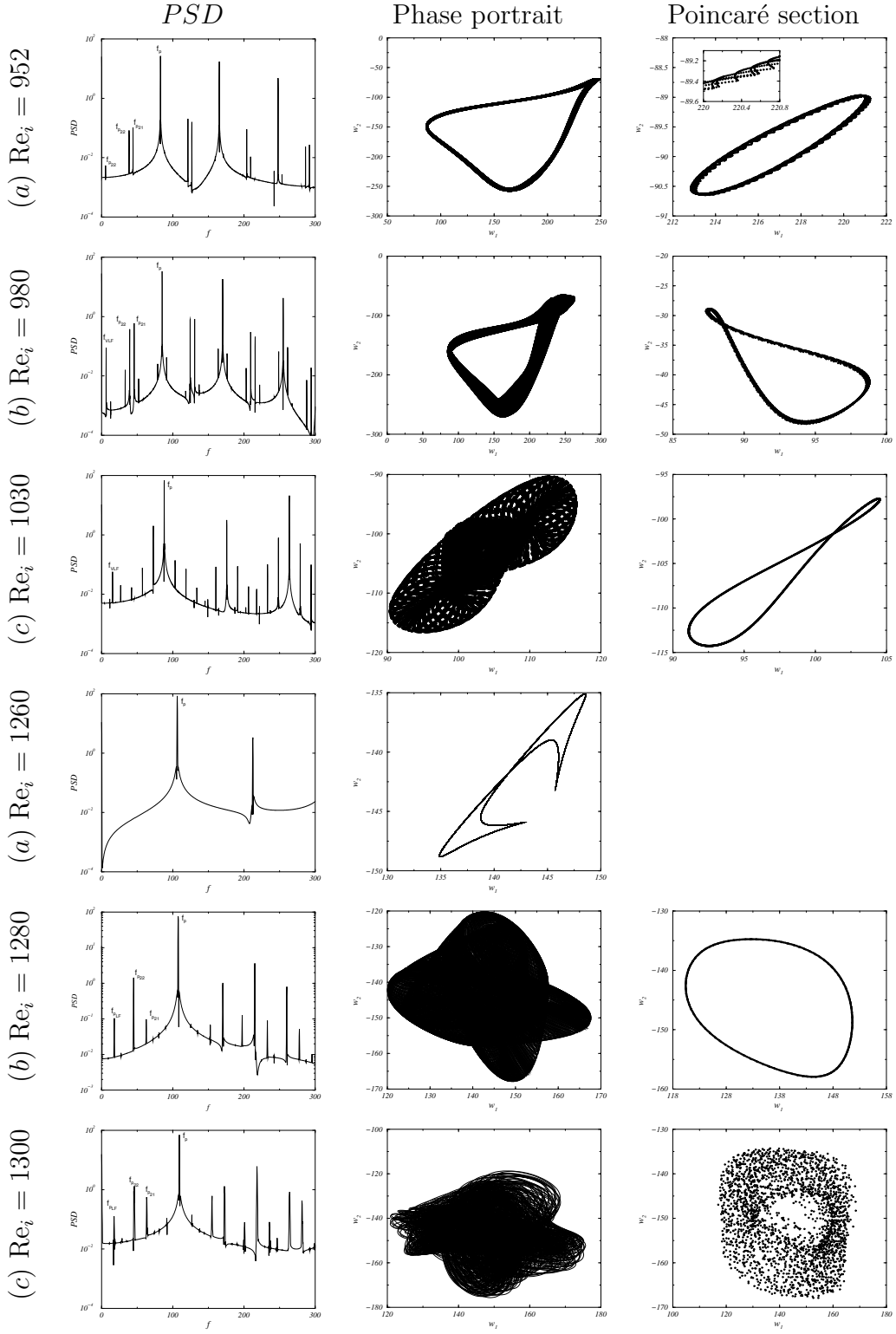

Figure 6.12: Power spectral density, phase portrait and Poincaré section illustrating the route the chaos when Re_i is increased and $\Gamma = 9.25$ is fixed. The initial state is the ALS_{10} at $\mathrm{Re}_i = 920$. (a) State resulting from the first transition at $\mathrm{Re}_i = 952$; (b) Intermediate state before the transition to the ALS_4 at $\mathrm{Re}_i = 980$; (c) ALS_4 with a low frequency mode at $\mathrm{Re}_i = 1030$; (d) ALS_4 as rotating wave at $\mathrm{Re}_i = 1260$. (e) Emergence of the low frequency mode at $\mathrm{Re}_i = 1280$. (f) Chaotic flow at $\mathrm{Re}_i = 1300$.

section gives in this case a single point in phase space, and thus it has not been plotted. When $\mathrm{Re}_i > 1275$ the coupling between neighboring vortices is again broken, resulting in a similar mechanism to that described for the first transition. Figure 6.12 (e) illustrates this state at $\mathrm{Re}_i = 1280$. It is observed that, alike the first transition, there arise two peaks at $f_{p_{21}}$ and $f_{p_{22}}$, which are equidistant to $f_p/2$, and their difference leads to the appearance of a low frequency f_{LF}. Since the difference between $f_{p_{21}}$ and $f_{p_{22}}$ is significantly larger than in the first transition, f_{LF} is approximately one order of magnitude higher than f_{VLF}. Moreover, the amplitude of $f_{p_{22}}$ near the bifurcation is much larger than that of $f_{p_{21}}$, in contrast to the first transition, where both frequencies emerged approximately with the same amplitude. This could be related to the existence of a single outgoing jet oscillating with large amplitude in the ALS_4. Note that, unlike figures 6.11 (a) and 6.12 (a), the Poincaré section does not reflect a doubled loop, which is probably due to dominance of $f_{p_{22}}$ over $f_{p_{21}}$. Subsequently increasing Re_i, f_{LF} and $f_{p_{21}}$ increase progressively their amplitude and additional frequencies come into play, causing eventually the appearance of chaos. The flow becomes first chaotic at $\mathrm{Re}_i = 1300$, which is shown in figure 6.12 (f).

6.5 Conclusion

The bifurcation scenario in a wide gap ($\eta = 0.5$) Taylor-Couette apparatus, where only the inner cylinder is rotating and the length-to-gap aspect ratio is restricted to the range $8.85 < \Gamma < 9.95$ has been numerically investigated. We focus on the dynamics of recently reported experimental flow patterns (Abshagen *et al.*, 2012) which exhibit large amplitude oscillations localized in some of the outgoing jets of the bulk vortices. We refer to these states as axially localized states ALS.

We find that, for the particular case of a 10-vortex flow, four different ALS coexist in the parameter space, differing in the axial position where the large amplitude oscillations take place. We have not found all possible ALS for this flow (6), but consistently with the experiments, all ALS having a single outgoing jet oscillating with large amplitude occur. There is only one ALS with large amplitude oscillations in two outgoing jets, which is the most stable ALS at the lowest values of Re_i in the region of the parameter space where the ALS are located. The states that retains the axial reflexion symmetry are more stable than the asymmetric states, and thus they are found in larger areas of the parameter space. These results are also in full agreement with experimental observations (Abshagen *et al.*, 2012).

Each *ALS* is related to a specific stable coupling of the vortex pairs in a finite-length system. Varying the control parameters (Γ and Re_i) modifies the wavelengths of the different vortex pairs, generally increasing (decreasing) in those vortex pairs where the large amplitude oscillations manifest, and in return, decreasing (increasing) in the Ekman vortices. While the coupling between the vortices remains, the *ALS* are rotating waves with a single precession frequency that coincide with that for the so-called large jet state *LJ* (Gerdts *et al.*, 1994), in which all outgoing jets in the bulk flow oscillate with large amplitude. Nevertheless, when the coupling is broken there arise disturbances in the wavelength of the different vortex pairs that slowly spread in axial direction, similarly to the situation described in Gerdts *et al.* (1994), who termed the resulting axisymmetric motion as very low frequency mode *VLF*. The growth of these disturbances determines the flow transitions occurring as the control parameters are varied, leading to either a different *ALS* or the appearance of chaos.

We observed that, in all cases, the *VLF* seems to emerge almost simultaneously with the period doubling of the orbit associated with the precession frequency of the *ALS* f_p, resulting in two frequencies, f_{p21} and f_{p22}, in the vicinity of $f_p/2$, and separated $\pm$ $f_{VLF}/2$ from it. Nevertheless, the frequency spectrum and Poincaré section reveal some interesting differences between *ALS* having one or two outgoing jets oscillating with large amplitude. In the latter case f_{p21} and f_{p22} arise with nearly the same amplitude, and the periodic orbit obtained in a Poincaré section reflects a trajectory that follows a double loop in a small region of phase space. In contrast, in the former case, f_{p22} is higher than f_{p21}, and a single loop trajectory is obtained in a Poincaré section. After this transition, the behavior has been found to depend on the control parameter that is changed. Decreasing Γ (when $\mathrm{Re}_i < 950$) results in restoring the phase coherence between vortex pairs, so f_{VLF} approaches zero and the system undergoes a second period doubling bifurcation, which precedes the final transition to chaos. In contrast, when Re_i is increased, the value of f_{VLF} as well as its amplitude gradually increase, leading to a distinct *ALS* or, at a sufficiently high Re_i, to the occurrence of chaos. This behavior is also observed when decreasing Γ for $\mathrm{Re}_i > 950$.

The behavior of the *VLF* mode is very sensitive to changes in the control parameters. It has been found to occur through distinct types of bifurcations and its magnitude f_{VLF} substantially increases with Re_i (Abshagen & Pfister, 2000; von Stamm *et al.*, 1996). There also exist experimental evidences suggesting different dynamical behaviors of the *VLF* when the number of vortices in the flow is greater than 20 (von Stamm *et al.*, 1996). Consequently, it is likely that different transitions to those described in this chapter will arise in systems with higher Γ. Nevertheless, the computational cost of properly solving

extended geometries at high values of Re_i with our methods is extremely large, if not impossible in many cases. The implementation of multi-domain methods, such as that in Viazzo & Poncet (2014), could help cope with this problem, an therefore it will be considered in the future in order to keep studying the rich and complex dynamics existing in these systems.

CHAPTER 7
OVERVIEW

Understanding the dynamics of rotating fluids, and in particular the mechanisms involved in the onset of turbulence, is one the most important challenges facing the Fluid Dynamics community. Resolving this long-running problem would have a tremendous impact on a wide variety of industrial, geophysical and astrophysical processes (see section 1.1 for an overview), which in most cases are of vital importance to society, the economy and the environment. Due to the intrinsic complexity of the problem, it is approached using models based on simple geometries such as cylinders or annuli, which allow for straightforward laboratory and numerical experiments. The advancement of scientific understanding in this area will be to a large extent determined by the interaction between these two research tools. This thesis is intended to assist in comparing and interpreting the results provided by experiments and numerical simulations, in some cases identifying weaknesses of the latter when reproducing experimental results, and in others, highlighting the advantages that they provide over laboratory experiments.

The numerical approach adopted to deal with the Navier-stokes equations governing these flows embraces several tools such as direct numerical simulations, linear stability analysis, Newton and continuation methods or time series analysis. In all cases, simulations have been performed using spectral codes which have for the most part been developed during the thesis. They have been discussed in detail in chapter 2. Special attention has been paid to the solver described in 2.2, which has been entirely designed and implemented for the completion of this doctoral thesis. Task distribution based on *MPI* has been been accomplished, allowing for fast and efficient computations. As a result, regions of parameter space that were computationally intractable with the previously existing codes, i.e. the large aspect-ratio facilities of chapter 6, have been addressed in this thesis. This code is currently being used to successfully simulate experimental quasi-keplerian flows at large rotation speeds (Edlund & Ji, 2014) and it will certainly serve as an important tool for the scientific production of the group in the near future. The performance and scalability of the code can be significantly improved through a hybrid *OpenMP–MPI* approach, which will be accomplished over the next few months. It is also worth briefly mentioning that the spectral-finite-differences solver for laterally heated axially periodic Taylor–Couette flows delineated in 2.3, which is an extension of Shi *et al.* (2015), was granted to participate in the *LRZ-Extreme Scaling* workshop in Garching (Germany), showing acceptable weak scalability up to 8 islands in the *SuperMuc* computer ($8 \times \times 512 \times 16 = 65536$ cores).

Chapter 3 focuses on the dynamical changes resulting from symmetry-breaking due to experimental imperfections. In particular, it considers the pinning phenomenon that occurs when a rotating wave with precession frequency near zero is stopped by the imperfections and becomes a steady solution. This happens in a finite region of the parameter space which is referred to as pinning region. The chapter can be divided into two parts. In the first one the normal form of a Hopf bifurcation with zero frequency in which the $SO(2)$ symmetry is broken by adding a ϵ term has been analyzed. As a result of this symmetry-breaking, the curve of solutions with zero frequency splits into two curves, located to the left and right of the former, which delimit the pinning region. It was found that these curves are infinite period bifurcations ($SNIC$). As they approach the Hopf bifurcation curve the dynamics becomes very complex, with several codimension-two and global bifurcations in a small region of parameter space. In the second part of the chapter, the theoretical predictions have been tested in the case of rotating Rayleigh-Bénard convection. In this problem a bifurcation scenario that fulfills the requirements for the occurrence of a pinning region (existence of rotating waves and precession frequency changing sign when the control parameters are varied) was identified. After checking that simulations in idealized systems do not allow for capturing pinned rotating waves, the $SO(2)$ symmetry was broken by imposing a linear temperature profile at the top lid. In doing so a pinning region bounded by infinite period bifurcation curves was found. It was observed that pinned solutions correspond to the attachment of the rotating wave to the sidewall. It must be emphasized that, unlike other pinning phenomena reported in fluid dynamics, this pinning occurs in a region of parameter space where the Hopf bifurcation is subcritical. Pinned rotating waves are likely to occur in experimental facilities for the study of rotating flows, which are typically $SO(2)$ equivariant, resulting in inconsistencies with the results of numerical simulations. It is thus important to have in mind the results provided in this chapter for the correct interpretation of these discrepancies.

Chapter 4 discusses how to incorporate a new term into the Navier-Stokes equations in order to consider centrifugal effects in certain situations in which they have been traditionally neglected. This new term is obtained from similar considerations to those in the classical Boussinesq approximation, which is used to take into account the gravitational buoyancy effects in incompressible flows. In addition to the traditional radial contribution of the centrifugal buoyancy, the new approach allows for considering secondary centrifugal effects stemming from differential rotation or strong internal vorticity. The significance of these effects has been elucidated by comparing, for several axially periodic configurations of laterally heated Taylor-Couette flows, the marginal curves ob-

tained with and without including the new term in the governing equations. In some cases, this plays a very relevant dynamical role, particularly at high rotation speeds, causing significant changes in the onset of instability and eigenfunctions with respect to the traditional approach. It is important to highlight that only the linear stability analysis of these flows has been considered. Even though, very substantial differences between the two approaches arise. A similar study to the one carried out here, but considering fully nonlinear computations, i.e. comparing the onset of secondary instability, would be an interesting future work to quantify the influence of the non-linear interactions in the centrifugal buoyancy. Alternatively, the study might be performed in finite geometries which can be easily tested experimentally. The radial velocities induced by the end walls result in significant centrifugal effects, so it is possible speculate that important discrepancies between the traditional and new approaches will be found for lower values of the rotation speed than in the axially periodic situation. The chapter has also provided a discussion on the suitability of using the new numerical approach for the study of quasi-keplerian shear flows (accretion disks), where the rotation speeds are extremely high. Although in this case, shear has been found to prevail over centrifugal buoyancy, and thus the marginal curves are almost identical in both approaches, the new term could be of great importance when the non-linear terms are considered. Since little effort both in preparation and execution is required to include the new term in existing numerical codes, we recommended to use the new approach in all situations, regardless of whether the centrifugal buoyancy is the dominant force or not.

The influence of finite-length effects in the dynamics of radially heated Taylor–Couette flows has been investigated in chapter 5. The onset of the primary and secondary instabilities, when rigid flat end walls (experimental boundary conditions) and axially periodic boundary conditions (infinite long cylinders; no boundary layers) are used, have been compared. Two experimental facilities, differing in the sense of the radial temperature gradient and relative rotation of the cylinders have been analyzed. When the inner cylinder rotates and the outer cylinder is held at rest (common setup to study industrial flows), the discrepancies between the finite and infinite cases mainly occur at high temperatures, because of the stable density gradient induced by the temperature difference between the Ekman layers, which strongly stabilizes the flow. Furthermore, the frictional effects due to the Ekman layers shift the marginal curve in the finite case towards larger values of the rotation speed. Nevertheless, when the temperature difference between the cylinders is small, the discrepancies due to friction only slightly affect the critical values for the onset of the transitions, and the dynamics is in both cases similar. When the system rotates as a solid-body (baroclinic annulus utilized to

model atmospheric instabilities), the axial velocity in the finite case is confined to the sidewall, which entirely modifies the base flow of the infinite case, resulting in completely different dynamics in both cases. The analysis carried out in this chapter is of interest in order to design future laboratory experiments to reproduce quasi-keplerian flows in the presence of radial temperature gradients. In numerical models of realistic accretion disks (Klahr & Bodenheimer, 2003; Petersen *et al.*, 2007; Lesur & Papaloizou, 2010), which neglect axial stratification, subcritical global and local instabilities have been found, which trigger turbulence that transport angular momentum outward at the rates estimated for real accretion disks (Richard & Zahn, 1999). In order to approximate such models in the laboratory, the axial temperature gradient due to the Ekman layers must be minimized. To this avail, one approach would be to heat the bottom lid, producing a vertical temperature gradient that opposes the former (see Stone *et al.*, 1969, in which the same strategy is applied for the case of solid-body rotation). The strong stabilizing effect due to axial stratification nearly disappears and the differences between finite and infinite systems would be solely due to Ekman friction. Since very small frictional effects are expected at large rotation speeds, it can be speculated that the dynamics will be similar in both cases. The results of axially periodic simulations could be used as a guideline to assure the validity of the experimental work.

Finally, in chapter 6 we report a numerical study of the bifurcation scenario experimentally found by Abshagen *et al.* (2012), in which global states with large amplitude oscillations localized in some of vortex-pairs arise in a certain region of parameter space. In contrast to the preceding chapters, where radial or axial temperature gradients are present, the experimental setup is an isothermal Taylor–Couette facility with moderate–large aspect ratio. The objective was to explore in detail the dynamics of these axially localized states and, in particular the transition to chaos, by making use of the advantages offered by numerical simulations for simultaneously extracting time series in several points of the fluid domain. Frequency analysis of these time series have been used to identify the bifurcations taking place. All results obtained are in full agreement with experimental observations. Four axially localized states over the six possible combinations existing for a 10-vortex flow have been found. These states, which appear for the same values of the control parameters (Reynolds number and aspect ratio normalized with the number of vortices) as in experiments, can be either rotating waves with a single precession frequency or quasi-periodic. The latter happens when they coexist with a very low frequency mode, which arise as a result of the breaking of the phase coherence between the oscillations of adjacent vortex pairs (Gerdts *et al.*, 1994; von Stamm *et al.*, 1996). The emergence of the very low frequency mode plays a key

role in the transition to chaos when the control parameters are changed. It seems to originate at the same time as the period-doubling of the frequency of the rotating wave, and grow in amplitude with the increase of the Reynolds number, leading eventually to chaotic flow. When the aspect ratio is reduced a second route to chaos has been found, in which the very low frequency becomes nearly zero and the main frequency undergoes a second period doubling before the flow becomes completely chaotic. The dynamics is in general very complex due to the high multiplicity of states, hence the sequence of transitions that is captured is entirely dependent on the initial state and the variations of the control parameters carried out.

BIBLIOGRAPHY

Abshagen, J., Heise, M., Hoffmann, C. & Pfister, G. 2008 Direction reversal of a rotating wave in Taylor-Couette flow. *J. Fluid Mech.* **607**, 199–208.

Abshagen, J., Heise, M., Pfister, G. & Mullin, T. 2010 Multiple localized states in centrifugally stable rotating flow. *PoF* **22**, 021702.

Abshagen, J. & Pfister, G. 2000 Low-dimensional dynamics of axisymmetric modes in wavy taylor vortex flow. In *Physics of Rotating Fluids* (ed. C. Egbers & G. Pfister), *Lecture Notes in Physics*, vol. 549, pp. 84–101. Springer.

Abshagen, J., von Stamm, J., Heise, M., Will, C. & Pfister, G. 2012 Localized modulation of rotating waves in taylor-couette flow. *PRE* **85** (5), 056307.

Ackerman, S. A. & Knox, J. 2003 *Meteorology: Understanding the atmosphere*. Pacific Grove, CA:Thomson Learning.

Ahlers, G., Grossmann, S. & Lohse, D. 2009 Heat transfer and large scale dynamics in turbulent Rayleigh-Bénard convection. *Rev. Mod. Phys.* **81** (2), 503–537.

Ali, M. E. & McFadden, G. B. 2005 Linear stability of cylindrical Couette flow in the convection regime. *Phys. Fluids* **17**.

Ali, M. E. & Weidman, P. D. 1990 On the stability of circular Couette-flow with radial heating. *J. Fluid Mech.* **220**, 53–84.

Andereck, C., S.S., L. & Swinney, H. 1986 Flow regimes in a circular Couette system with independently rotating cylinders. *J. Fluid Mech.* **164**, 155– 183.

Arfken, G. B. & Weber, H. J. 2005 *Mathematical Methods for Physicists*, 6th edn. Academic Press.

Avila, K. & Hof, B. 2013 High-precision Taylor-Couette experiment to study subcritical transitions and the role of boundary conditions and size effects. *Review of Scientific Instruments* **84**, 065106.

Avila, K., Moxey, D., de Lozar, A., Avila, M., Barkley, D. & Hof, B. 2011 The onset of turbulence in pipe flow. *Science* **333** (6039), 192–196.

Avila, M. 2012 Stability and angular-momentum transport of fluid flows between corotating cylinders. *Phys. Rev. Lett.* **108**, 124501.

Avila, M., Grimes, M., Lopez, J. M. & Marques, F. 2008 Global endwall effects on centrifugally stable flows. *Phys. Fluids* **20**, 104104.

Balbus, S. A. 2003 Enhanced angular momentum transport in accretion disks. *Annual Review of Astronomy and Astrophysics* **41** (1), 555–597.

Balbus, S. A. 2011 Fluid dynamics: A turbulent matter. *Nature* **470** (7335), 475–476.

Ball, K., Farouk, B. & Dixit, V. 1989 An experimental study of heat transfer in a vertical annulus with a rotating inner cylinder. *International Journal of Heat and Mass Transfer* **32** (8), 1517 – 1527.

Ball, K. S. & Farouk, B. 1987 On the development of taylor vortices in a vertical annulus with a heated rotating inner cylinder. *Int. J. Numer. Meth. Fluids* **7**, 857–867.

Ball, K. S. & Farouk, B. 1988 Bifurcation phenomena in taylor–couette flow with buoyancy effects. *J. Fluid Mech.* **197**, 479–501.

Ball, K. S. & Farouk, B. 1989 A flow visualization study of the effects of buoyancy on taylor vortices. *Phys. Fluids A* **1**, 1502–1507.

Bannon, P. 1996 On the anelastic approximation for a compressible atmosphere. *J. Aero. Sci.* **53** (23), 3618–3628.

Barcilon, V. 1964 Role of the ekman layers in the stability of the symmetric regime obtained in a rotating annulus. *Journal of the Atmospheric Sciences* **21** (3), 291–299.

Barcilon, V. & Pedlosky, J. 1967 On the steady motions produced by a stable stratification in a rapidly rotating fluid. *J. Fluid Mech.* **29**, 673–690.

Barkley, D. & Tuckerman, L. S. 2005 Computational study of turbulent laminar patterns in couette flow. *Physical review letters* **94** (1), 014502.

Batchelor, G. K. 1967 *An introduction to Fluid Mechanics*. Cambridge University Press.

Benjamin, T. B. 1978 Bifurcation Phenomena in Steady Flows of a Viscous Fluid. I. Theory. *Proc. Roy. Soc. Lond. A* **359** (1696).

Benjamin, T. B. & Mullin, T. 1982 Notes on the multiplicity of flows in the Taylor experiment. *J. Fluid Mech.* **121**, 219–230.

Bjorklund, I. & Kays, W. 1959 The heat transfer between concentric rotating cylinders. *Journal of Heat Transfer* **81**, 175–186.

Boning, C. W., Dispert, A., Visbeck, M., Rintoul, S. R. & Schwarzkopf, F. U. 2008 The response of the antarctic circumpolar current to recent climate change. *Nature Geosci* **1**, 864–869.

Boussinesq, J. 1903 *Théorie Analytique de la Chaleur*, , vol. II. Gauthier-Villars, Paris.

Brandstater, A. & Swinney, H. L. 1987 Strange attractors in weakly turbulent couette-taylor flow. *Physical Review A* **35** (5), 2207.

Broer, H., van Dijk, R. & Vitolo, R. 2008 Survey of strong normal-internal k:l resonances in quasi-periodically driven oscillators for l = 1, 2, 3. In *SPT 2007: Symmetry and Perturbation Theory, Otranto 2007* (ed. G. Gaeta, R. Vitolo & S. Walcher), pp. 45–55. World Scientific.

Brummell, N., Hart, J. E. & Lopez, J. M. 2000 On the flow induced by centrifugal buoyancy in a differentially-heated rotating cylinder. *Theoret. Comput. Fluid Dynamics* **14**, 39–54.

Bryant, P. & Wiesenfeld, K. 1986 Suppression of period-doubling and nonlinear parametric effects in periodically perturbed systems. *Physical Review A* **33** (4), 2525.

Campbell, S. A. & Holmes, P. 1992 Heteroclinic cycles and modulated travelling waves in a system with D_4 symmetry. *Physica D* **59**, 52–79.

Canuto, C., Quarteroni, A., Hussaini, M. Y. & Zang, T. A. 2007 *Spectral Methods. Evolution to Complex Geometries and Applications to Fluid Dynamics*. Springer-Verlag.

Chandrasekhar, S. 1961 *Hydrodynamic and Hydromagnetic Stability*. Oxford University Press.

Childs, P. 2011 *Rotating flow*. Elsevier.

Choi, I. & Korpela, S. 1980 Stability of the conduction regime of natural convection in a tall vertical annulus. *J. Fluid Mech.* **99**, 725–738.

Chossat, P. & Iooss, G. 1994 *The Couette–Taylor Problem*. Springer.

Chossat, P. & Lauterbach, R. 2000 *Methods in Equivariant Bifurcations and Dynamical Systems*. World Scientific.

Chow, S. N., Li, C. & Wang, D. 1994 *Normal Forms and Bifurcations of Planar Vector Fields*. Cambridge: Cambridge University Press.

Coles, D. 1965 Transition in Circular Coeutte Flow. *J. Fluid Mech.* **21**, 385–425.

Collins, A. 2004 *Ocean circulation*. The open university. Butterworth-Heinemann.

Couette, M. 1888 On a new apparatus for the study of friction of fluids. *Compt. Rend.* **107**, 388–390.

Coughlin, K. T. & Marcus, P. S. 1992 Modulated waves in Taylor-Couette flow Part 2. Numerical simulation. *J. Fluid Mech.* **234**, 19–46.

Crawford, J. D. & Knobloch, E. 1991 Symmetry and symmetry-breaking bifurcations in fluid dynamics. *Annu. Rev. Fluid Mech.* **23**, 341–387.

Dangelmayr, G., Hettel, J. & Knobloch, E. 1997 Parity-breaking bifurcation in inhomogeneous systems. *Nonlinearity* **10**, 1093–1114.

Dawes, J. 2010 The emergence of a coherent structure for coherent structures: localized states in nonlinear systems. *Philosophical Transactions of the Royal Society A: Mathematical, Physical and Engineering Sciences* **368** (1924), 3519–3534.

DiPrima, R. C., Eagles, P. M. & Ng, B. S. 1984 The effect of radius ratio on the stability of couette flow and taylor vortex flow. *Physics of Fluids* **27** (10), 2403–2411.

Dorfman, L. 1963 *Hydrodynamic Resistance and the Heat Loss of Rotating Solids*. Oliver & Boyd.

Drake, R. P. 2009 Plasma astrophysics: How to see a black hole. *Nat Phys* **5**.

Drazin, P. R. & Reid, W. H. 2004 *Hydrodynamic Stability*, 2nd edn. Cambridge University Press.

Duguet, Y., Schlatter, P. & Henningson, D. S. 2009 Localized edge states in plane couette flow. *Physics of Fluids (1994-present)* **21** (11), 111701.

Dumortier, F., Roussarie, R. & Sotomayor, J. 1997 Bifurcations of cuspidal loops. *Nonlinearity* **10**, 1369–1408.

Dutcher, C. S. & Muller, S. J. 2009 Spatio-temporal mode dynamics and higher order transitions in high aspect ratio newtonian taylor–couette flows. *Journal of Fluid Mechanics* **641**, 85–113.

Eckhardt, B., Schneider, T. M., Hof, B. & Westerweel, J. 2007 Turbulence transition in pipe flow. *Annu. Rev. Fluid Mech.* **39**, 447–468.

Edlund, E. M. & Ji, H. 2014 Nonlinear stability of laboratory quasi-keplerian flows. *Physical Review E* **89** (2), 021004.

Elperin, T., Kleeorin, N. & Rogachevskii, I. 1998 Dynamics of particles advected by fast rotating turbulent fluid flow: Fluctuations and large-scale structures. *Phys. Rev. Lett.* **81**, 2898–2901.

Esser, A. & Grossmann, S. 1996 Analytic expression for TaylorCouette stability boundary. *Physics of Fluids* **8** (7), 1814–1819.

Farneti, R., Delworth, T. L., Rosati, A. J., Griffies, S. M. & Zeng, F. 2010 The role of mesoscale eddies in the rectification of the southern ocean response to climate change. *Journal of Physical Oceanography* **40**.

Fein, J. 1973 An experimental study of the effects of the upper boundary condition on the thermal convection in a rotating cylindrical annulus of water. *Geophys. Astrophys. Fluid Dynam.* **5**.

Fein, J. & Pfeffer, R. 1976 An experimental study of the effects of prandtl number on thermal convection in a rotating, differentially heated cylindrical annulus of fluid. *J. Fluid Mech.* **75**, 81–112.

Fenot, M., Bertin, Y., Dorignac, E. & Lalizel, G. 2011 A review of heat transfer between concentric rotating cylinders with or without axial flow. *International journal of thermal sciences* **50** (7), 1138–1155.

Gambaudo, J. M. 1985 Perturbation of a Hopf bifurcation by an external time-periodic forcing. *J. Diff. Eqns.* **57**, 172–199.

Gazley, U. 1958 Heat transfer characteristics of the rotational and anal flow between concentric cylinders. *Journal of Heat Transfer* **80**, 79–90.

Gelfgat, A. 2011 Destabilization of free convection by weak rotation. *J. Fluid Mech.* **685**, 377–412.

Gerdts, U., von Stamm, J., Buzug, T. & Pfister, G. 1994 Axisymmetric time-dependent flow in the Taylor-Couette system. *Phys. Rev. E* **49** (5), 4019–4026.

Golubitsky, M. & Schaeffer, D. G. 1985 *Singularities and Groups in Bifurcation Theory, vol. I*. Springer.

Golubitsky, M. & Stewart, I. 1986 Symmetry and Stabiliy in Taylor-Couette flow. *" SIAM J. Math. Anal."* **17(2)**, 249– 288.

Golubitsky, M. & Stewart, I. 2002 *The Symmetry Perspective: From Equilbrium to Chaos in Phase Space and Physical Space*. Birkhäuser.

Golubitsky, M., Stewart, I. & Schaeffer, D. G. 1988 *Singularities and Groups in Bifurcation Theory*, *Appl. Math. Sci.*, vol. II. Springer.

Gorman, M. & Swinney, H. L. 1982 Spatial and temporal characteristics of modulated waves in the circular Couette system . *J. Fluid Mech.* **117**, 123–142.

Greenspan, H. P. 1968 *The Theory of Rotating Fluids*, 2nd edn. Cambridge University Press.

Haragus, M. & Iooss, G. 2011 *Local Bifurcations, Center Manifolds, and Normal Forms in Infinite-Dimensional Dynamical Systems*. Springer.

Hart, J. E. 2000 On the influence of centrifugal buoyancy on rotating convection. *Journal of Fluid Mechanics* **403**, 133–151.

Heise, M., Abshagen, J., Küter, D., Hochstrate, K., Pfister, G. & Hoffmann, C. 2008 Localized spirals in taylor-couette flow. *Phys. Rev. E* **77**, 026202.

Hide, R. 1958 An experimental study of thermal convection in a rotating liquid. *Phil. Trans. Roy. Soc. Lond. A* **250**, 441–478.

Hide, R. & Fowlis, W. 1965 Thermal convection in a rotating annulus of liquid: Effect of viscosity on the transition between axisymmetric and non-axisymmetric flow regimes. *Journal of Atmospheric Sciences* **22**, 541–558.

Hide, R. & Mason, P. J. 1975 Sloping convection in a rotating fluid. *Advances in Physics* **24**, 47–100.

Hirschberg, P. & Knobloch, E. 1996 Complex dynamics in the Hopf bifurcation with broken translation symmetry. *Physica D* **90**, 56–78.

Holton, J. R. 1965 The influence of viscous boundary layers on transient motions in a stratified rotating fluid. part i. *Journal of the Atmospheric Sciences* **22** (4), 402–411.

Homsy, G. M. & Hudson, J. L. 1969 Centrifugally driven thermal convection in a rotating cylinder. *Journal of Fluid Mechanics* **null**, 33–52.

Homsy, G. M. & Hudson, J. L. 1971 Centrifugal convection and its effect on the asymptotic stability of a bounded rotating fluid heated from below. *Journal of Fluid Mechanics* **48**, 605–624.

Horner, H. 1983 Periodic perturbation on a period-doubling system. *Phys. Rev. A* **27**, 1270–1271.

Hughes, S. & Randriamampianina, A. 1998 An improved projection scheme applied to pseudospectral methods for the incompressible navier stokes equations. *Intnl J. Num. Meth. Fluids* **28**, 501–521.

Ji, H., Burin, M., Schartman, E. & Goodman, J. 2006 Hydrodynamic turbulence cannot transport angular momentum effectively in astrophysical disks. *Nature* **444**, 343–346.

Jones, C. 1985 The transition to wavy Taylor Vortices . *J. Fluid Mech.* **157**, 135– 162.

Kedia, R., Hunt, M. L. & Colonius, T. 1998 Numerical simulations of heat transfer in taylor-couette flow. *J. Heat Transfer* **120**, 65–71.

Keener, J. P. 1987 Propagation and its failure in coupled systems of discrete excitable cells. *SIAM J. Appl. Math.* **47**, 556–572.

King, G. P. & Swinney, H. L. 1983 Limits of stability and irregular flow patterns in wavy vortex flow. *Phys. Rev. A* **27**, 1240–1243.

Klahr, H. & Bodenheimer, P. 2003 Turbulence in accretion disks: Vorticity generation and angular momentum transport via the global baroclinic instability. *The Astrophysical Journal* **582** (2), 869.

Klahr, H., Henning, T. & Kley, W. 1999 On the azimuthal structure of thermal convection in circumstellar disks. *The Astrophysical Journal* **514** (1), 325.

Knobloch, E., Hettel, J. & Dangelmayr, G. 1995 Parity breaking bifurcation in inhomogeneous systems. *Phys. Rev. Lett.* **74**, 4839–4842.

Koschmieder, E. L. 1972 Convection in a rotating laterally heated annulus. *J. Fluid Mech.* **51**, 637–656.

Kreith, F. 1968 Convection heat transfer in rotating systems. *Advances in heat transfer* **5**, 129–251.

Kuo, D.-C. & Ball, K. S. 1997 Taylor-Couette flow with buoyancy: Onset of spiral flow. *Phys. Fluids* **9**, 2872–2884.

Kuznetsov, Y. A. 1998 *Elements of Applied Bifurcation Theory, Second Edition*. Springer–Verlag.

Kuznetsov, Y. A. 2004 *Elements of Applied Bifurcation Theory*, 3rd edn. Springer.

Lamb, J. S. W. & Wulff, C. 2000 Pinning and locking of discrete waves. *Physics Letters A* **267**, 167–173.

Lappa, M. 2012 *Rotating Thermal Flows in Natural and Industrial Processes*. John Wiley and Sons.

Larcher, T., Fournier, A. & Hollerbach, R. 2013 The influence of a sloping bottom endwall on the linear stability in the thermally driven baroclinic annulus with a free surface. *Theoret. Comput. Fluid Dynamics* **27** (3-4), 433–451.

Launder, B., Poncet, S. & Serre, E. 2010 Laminar, transitional, and turbulent flows in rotor-stator cavities. *Annual Review of Fluid Mechanics* **42** (1), 229–248.

Lee, Y., Korpela, S. A. & Horn, R. N. 1982 Structure of multicellular natural convection in a tall vertical annulus. In *Proc. 7th Zntl Heat Transfer Conf. Munich*, , vol. 2, pp. 221–226.

Lepiller, V., Goharzadeh, A., Prigent, A. & Mutabazi, I. 2008 Weak temperature gradient effect on the stability of the circular couette flow. *The European Physical Journal B* **61**, 445–455.

Lesur, G. & Papaloizou, J. C. B. 2010 The subcritical baroclinic instability in local accretion disc models. *AA* **513**, A60.

Lewis, G. & Nagata, W. 2004 Linear stability analysis for the differentially heated rotating annulus. *Geophys. Astrophys. Fluid Dynam.* **98**, 129–152.

Lopez, J. M. & Marques, F. 2009 Centrifugal effects in rotating convection: nonlinear dynamics. *J. Fluid Mech.* **628**, 269–297.

Lopez, J. M., Rubio, A. & Marques, F. 2006 Travelling circular waves in axisymmetric rotating convection. *Journal of Fluid Mechanics* **569**, 331–348.

Lopez, J. M. & Shen, J. 1998 An efficient spectral-projection method for the Navier-Stokes equations in cylindrical geometries I. Axisymmetric cases. *J. Comput. Phys.* **139**, 308–326.

Mamun, C. K. & Tuckerman, L. S. 1995 Asymmetry and hopf bifurcation in spherical couette flow. *Phys. Fluids* **7**, 80–91.

Marcus, P. S. 1984 Simulation of Taylor-Couette flow. Part 2. Numerical results for wavy-vortex flow with one travelling wave. *J. Fluid Mech.* **146**, 65–113.

Maretzke, S., Hof, B. & Avila, M. 2014 Transient growth in linearly stable taylor–couette flows. *Journal of Fluid Mechanics* **742**, 254–290.

Marques, F. & Lopez, J. 2006 Onset of three-dimensional unsteady states in small-aspect-ratio taylor–couette flow. *Journal of Fluid Mechanics* **561**, 255–277.

Marques, F., Mercader, I., Batiste, O. & Lopez, J. M. 2007 Centrifugal effects in rotating convection: Axisymmetric states and three-dimensional instabilities. *J. Fluid Mech.* **580**, 303–318.

Marques, F., Meseguer, A., Lopez, J. M., Pacheco, J. R. & Lopez, J. M. 2012 Hopf bifurcation with zero frequency and imperfect $SO(2)$ symmetry. *arXiv* **math.DS** (1206.1643).

Marques, F., Meseguer, A., Lopez, J. M., Pacheco, J. R. & Lopez, J. M. 2013 Bifurcations with imperfect so(2) symmetry and pinning of rotating waves. *Proc. Roy. Soc. Lond. A* **469** (2152).

McFadden, G. B., Coriell, S. R., Boisvert, R. F. & Glicksman, M. E. 1984 Asymmetric instabilities in buoyancy-driven flow in a tall vertical annulus. *Phys. Fluids* **27**, 1359–1361.

Mellibovsky, F., Meseguer, A., Schneider, T. M. & Eckhardt, B. 2009 Transition in localized pipe flow turbulence. *Phys. Rev. Lett.* **103**, 054502.

Mercader, I., Batiste, O. & Alonso, A. 2006 Continuation of travelling-wave solutions of the Navier-Stokes equations. *Intnl J. Num. Meth. Fluids* **52**, 707–721.

Mercader, I., Batiste, O. & Alonso, A. 2010 An efficient spectral code for incompressible flows in cylindrical geometries. *Computers and Fluids* **39**, 215–224.

Meseguer, A., Avila, M., Mellibovsky, F. & Marques, F. 2007 Solenoidal spectral formulations for the computation of secondary flows in cylindrical and annular geometries. *European Physics Journal Special Topics* **146**, 249–259.

Meseguer, A. & Marques, F. 2000 On the competition between centrifugal and shear instability in spiral Couette flow. *J. Fluid Mech.* **402**, 33–56.

Moon, F. C. 2008 *Chaotic and Fractal Dynamics: Introduction for Applied Scientists and Engineers*. John Wiley & Sons.

Mullin, T. 1985 Onset of time dependence in taylor-couette flow. *Phys. Rev. A* **31**, 1216–1218.

Mundt, M., Hart, J. & Ohlsen, D. 1995 Symmetry, sidewalls, and the transition to chaos in baroclinic systems. *J. Fluid Mech.* **300**, 311–338.

Ning, L. & Ecke, R. E. 1993 Rotating rayleigh-bénard convection: Aspect-ratio dependence of the initial bifurcations. *Phys. Rev. E* **47**, 3326–3333.

Nishioka, M. & Asai, M. 1985 Some observations of the subcritical transition in plane poiseuille flow. *Journal of Fluid Mechanics* **150**, 441–450.

Orszag, S. A. & Patera, A. T. 1983 Secondary instability of wall-bounded shear flows. *J. Fluid Mech.* **128**, 347–385.

Pacheco, J. R., Lopez, J. M. & Marques, F. 2011 Pinning of rotating waves to defects in finite Taylor-Couette flow. *J. Fluid Mech.* **666**, 254–272.

Paoletti, M. S. & Lathrop, D. P. 2011 Measurement of angular momentum transport in turbulent flow between independently rotating cylinders. *Phys. Rev. Lett.* **106**, 024501.

Pedlosky, J. 1982 Geophysical fluid dynamics. *New York and Berlin, Springer-Verlag, 1982. 636 p.* **1**.

Petersen, M., Julien, K. & Stewart, G. 2007 Baroclinic vorticity production in protoplanetary disks. *The Astrophysical Journal* **658**, 1236–1251.

Pierrehumbert, R. & Swanson, K. 1995 Baroclinic instability. *Annu. Rev. Fluid. Mech.* **27**, 419–467.

Randriamampianina, A., Früh, W.-G., Read, P. L. & Maubert, P. 2006 Direct numerical simulations of bifurcations in an air-filled rotating baroclinic annulus. *J. Fluid Mech.* **561**, 359–389.

Regev, O. & Umurhan, O. M. 2008 On the viability of the shearing box approximation for numerical studies of mhd turbulence in accretion disks. *Astron. Astroph.* **481** (1), 21–32.

Reynolds, O. 1883 An experimental investigation of the circumstances which determine whether the motion of water shall be direct or sinuous, and of the law of resistance in parallel channels. *Proceedings of the royal society of London* **35** (224-226), 84–99.

Rhodes, M. 1998 *Introduction to particle technology*. John Wiley and Sons.

Richard, D. & Zahn, J.-P. 1999 Turbulence in differentially rotating flows what can be learned from the couette-taylor experiment. *Astron.Astrophys.* **347**, 734.

Romanov, V. 1973 Stability of plane-parallel couette flow. *Functional analysis and its applications* **7** (2), 137–146.

Alziary de Roquefort, T. & Grillaud, G. 1978 Computation of taylor vortex flow by a transient implicit method . *Computers and Fluids* **6** (4), 259 – 269.

Rossby, H. T. 1969 A study of benard convection with and without rotation. *Journal of Fluid Mechanics* **36**, 309–335.

Rubio, A., Lopez, J. M. & Marques, F. 2009 Onset of Küppers-Lortz-like dynamics in finite rotating thermal convection. *J. Fluid Mech.* .

Saleh, K. & Wagener, F. O. O. 2010 Semi-global analysis of periodic and quasi-periodic normal-internal $k:1$ and $k:2$ resonances. *Nonlinearity* **23**, 2219–2252.

Sanchez-Lavega, A. 2011 *An Introduction to Planetary Atmospheres*. Taylor & Francis.

Schneider, T. M., Gibson, J. F. & Burke, J. 2010*a* Snakes and ladders: localized solutions of plane couette flow. *Physical review letters* **104** (10), 104501.

Schneider, T. M., Marinc, D. & Eckhardt, B. 2010*b* Localized edge states nucleate turbulence in extended plane couette cells. *Journal of Fluid Mechanics* **646**, 441–451.

Shepherd, D. G. 1956 *Principles of turbomachinery*. Macmillan.

Shi, L., Rampp, M., Hof, B. & Avila, M. 2015 A hybrid mpi-openmp parallel implementation for pseudospectral simulations with application to taylor-couette flow. *Computers and Fluids* **106**, 1–11.

Siedler, G., Griffies, S., Gould, J., Gould, W. & Church, J. 2013 *Ocean Circulation and Climate: A 21st Century Perspective*, *Academic Press*, vol. 103. Elsevier Science and Technology Books.

Singer, P. 1984 Techniques of low pressure chemical vapor deposition. *Semiconductor, Int.* pp. 72–77.

Snyder, H. A. & Karlsson, S. K. F. 1964 Experiments on the stability of couette motion with a radial thermal gradient. *Phys. Fluids* **7**, 1696.

Sorour, M. M. & Coney, J. E. R. 1979 The effect of temperature gradient on the stability of flow between vertical concentric rotating cylinders. *J. Mech. Engng. Sci.* **21**, 403–409.

von Stamm, J., Gerdts, U., Buzug, T. & Pfister, G. 1996 Symmetry breaking and period doubling on a torus in the VLF regime in Taylor-Couette flow. *Phys. Rev. E* **54** (5), 4938–4957.

Stone, P., Hess, S., Hadlock, R. & Ray, P. 1969 Preliminary results of experiments with symmetric baroclinic instabilities. *Journal of the Atmospheric Sciences* **26** (5), 991–996.

Sugata, S. & Yoden, S. 1990 The effects of centrifugal buoyancy force on the stability of axisymmetric viscous flow in a rotating annulus. *J. Fluid Mech.* **229**, 471–482.

Svensmark, H. & Samuelsen, M. R. 1990 Perturbed period-doubling bifurcation. i. theory. *Physical Review B* **41** (7), 4181.

Tassoul, J. L. 2000 *Stellar Rotation*. Cambridge Univ. Press.

Taylor, G. I. 1923 Stability of a Viscous Liquid Contained between Two Rotating Cylinders. *Phil. Trans. Roy. Soc. Lond. A* **223** (605-615), 289–343.

Thiele, U. & Knobloch, E. 2006*a* Driven drops on heterogeneous substrates: onset of sliding motion. *Phys. Rev. Lett.* **97**, 204501.

Thiele, U. & Knobloch, E. 2006*b* On the depinning of a driven drop on a heterogeneous substrate. *New Journal of Physics* **8**, 313.

de Vahl Davis, G. & Thomas, R. W. 1969 Natural convection between concentric vertical cylinders. *Phys. Fluids Suppl. II* pp. 198–207.

Vallis, G. K. 2006 *Atmospheric and oceanic fluid dynamics: fundamentals and large-scale circulation*. Cambridge University Press.

Veronis, G. 1959 Cellular convection with finite amplitude in a rotating fluid. *Journal of Fluid Mechanics* **5** (03), 401–435.

Viazzo, S. & Poncet, S. 2014 Numerical simulation of the flow stability in a high aspect ratio taylor-couette system submitted to a radial temperature gradient. *Computers & Fluids* .

Vivès, C. 1988 Effects of a forced couette flow during the controlled solidification of a pure metal. *International journal of heat and mass transfer* **31** (10), 2047–2062.

Wagener, F. 2001 Semi-local analysis of the k : 1 and k : 2 resonances in quasi-periodically forced systems. In *Global Analysis of Dynamical Systems* (ed. W. Broer, B. Krauskopf & G. Vegter), pp. 113–129. IOP Publishing Ltd.

Westerburg, M. & Busse, F. H. 2003 Centrifugally driven convection in the rotating cylindrical annulus with modulated boundaries. *Nonlin. Proc. Geophys.* **10**, 275–280.

Williams, G. & Robinson, J. 1974 Generalized eady waves with ekman pumping. *Journal of the atmospheric sciencies* **31** (7), 1768–1776.

Williams, P., Read, P. & Haine, T. 2010 Testing the limits of quasi-geostrophic theory: application to observed laboratory flows outside the quasi-geostrophic regime. *J. Fluid Mech.* **649**, 187–203.

Willis, A. P. & Kerswell, R. R. 2009 Turbulent dynamics of pipe flow captured in a reduced model: puff relaminarization and localized edgestates. *Journal of Fluid Mechanics* **619**, 213–233.

Yoshikawa, H. N., Nagata, M. & Mutabazi, I. 2013 Instability of the vertical annular flow with a radial heating and rotating inner cylinder. *Phys. Fluids* **25**, 114104.

Zhao, S. & Yedlin, M. J. 1994 A new iterative chebyshev spectral method for solving the elliptic equation. *Journal of Computational Physics* **113** (2), 215 – 223.

Zhong, F., Ecke, R. & Steinberg, V. 1991 Asymmetric modes and the transition to vortex structures in rotating rayleigh-bénard convection. *Phys. Rev. Lett.* **67**, 2473–2476.

Zhong, F., Ecke, R. E. & Steinberg, V. 1993 Rotating rayleigh-benard convection: asymmetric modes and vortex states. *Journal of Fluid Mechanics* **249**, 135–159.